Received: 18 February 2022 | Revised: 13 April 2022 | Accepted: 4 May 2022

DOI: 10.1002/cne.25349

RESEARCH ARTICLE

JCN RESEARCH IN SYSTEMS NEUROSCIENCE THE JOURNAL OF COMPARATIVE NEUROLOGY WILEY

The brain of the tree pangolin (*Manis tricuspis*). IX. The pallial telencephalon

Aminu Imam[1,2] | **Adhil Bhagwandin**[1] | **Moyosore S. Ajao**[2] | **Paul R. Manger**[1]

[1]School of Anatomical Sciences, Faculty of Health Sciences, University of the Witwatersrand, Johannesburg, Republic of South Africa

[2]Department of Anatomy, Faculty of Basic Medical Sciences, College of Health Sciences, University of Ilorin, Ilorin, Nigeria

Correspondence
Paul Manger, School of Anatomical Sciences, University of the Witwatersrand, 7 York Road, Parktown, 2193, Johannesburg, South Africa.
Email: Paul.Manger@wits.ac.za

Funding information
Third World Academy of Sciences; the National Research Foundation-Third World Academy of Science African Renaissance Doctoral Fellowship (AI); the South African National Research Foundation (PRM)

Abstract

A cyto-, myelo-, and chemoarchitectonic analysis of the pallial telencephalon of the tree pangolin is provided. As certain portions of the pallial telencephalon have been described previously (olfactory pallium, hippocampal formation, and amygdaloid complex), we focus on the claustrum and endopiriform nuclear complex, the white matter and white matter interstitial cells, and the areal organization of the cerebral cortex. Our analysis indicates that the organization of the pallial telencephalon of the tree pangolin is similar to that observed in many other mammals, and specifically quite similar to the closely related carnivores. The claustrum of the tree pangolin exhibits a combination of insular and laminar architecture, while the endopiriform nuclear complex contains three nuclei, both reminiscent of observations made in other mammals. The population of white matter interstitial cells resembles that observed in other mammals, while a distinct laminated organization of the intracortical white matter was revealed with parvalbumin immunostaining. The cerebral cortex of the tree pangolin presented with indistinct laminar boundaries as well as pyramidalization of the neurons in both layers 2 and 4. All cortical regions typically found in mammals were present, with the cortical areas within these regions often corresponding to what has been reported in carnivores. Given the similarity of the organization of the pallial telencephalon of the tree pangolin to that observed in other mammals, especially carnivores, it would be reasonable to assume that the neural processing afforded the tree pangolin by these structures does not differ dramatically to that of other mammals.

KEYWORDS
Carnivora, cerebral cortex, claustrum, endopiriform nucleus

1 | INTRODUCTION

During development of the vertebrate brain, the embryonic telencephalic pallium forms medial, dorsal, lateral and ventral pallial regions. In mammals, the medial pallium forms the hippocampal region of the adult brain, the dorsal pallium forms the neocortical region, the lateral pallium forms the claustrum/dorsal and intermediate endopiriform nuclei, and insular cortex; and the ventral pallium forms the olfactory bulb, all olfactory cortical areas and related adjacent nuclei including the ventral endopiriform nucleus and much of the pallial amygdala (Watson & Puelles, 2017; Watson et al., 2017); however, certain aspects of amygdala development and relationships to specific pallial

regions, or whether the amygdala forms its own distinct pallial region, is still not fully resolved (Puelles, 2017). The adult neural structures that develop from these pallial telencephalic regions are involved in a broad spectrum of functions related to sensory, motor, and associative processes of various modalities of neural information that are used to create appropriate motor actions or inhibit inappropriate motor actions.

The brain of the tree pangolin has been observed to contain all the structures typically forming the mammalian pallial telencephalon (Imam et al., 2017). In addition, detailed descriptions of the olfactory portions of the pallial telencephalon (Imamet al., 2018a), the hippocampal formation (Imam et al., 2019a), and amygdaloid body (Imam et al., 2022a; Imam et al., 2022b) have been provided previously. Here we continue our detailed anatomical description of the structure of the brain of the tree pangolin (Imam et al., 2017; Imam et al., 2018a; Imam et al., 2018b; Imam et al., 2019a; Imam et al., 2019b; Imam et al., 2019c; Imam et al., 2022a, b) by providing a comprehensive architectonic account of the as yet undescribed structures of the pallial telencephalon. The structures include the claustrum and endopiriform nuclear complex (e.g., Real et al., 2003; Smith et al., 2018; Watson & Puelles, 2017), the white matter and white matter interstitial cells (WMICs, e.g., Bhagwandin et al., 2020; Swiegers et al., 2018), and the cerebral cortex (e.g., Homman-Ludiye et al., 2010; van Essen & Dierker, 2007; van der Gucht et al., 2007).

The tree pangolin is a solitary, nocturnal, myrmecophagic mammal belonging to the order Philodota, which is the recognized sister group of the Carnivora (e.g., Arnason et al., 2008; Foley et al., 2016). The tree pangolin does not appear to have unique sensory specializations, although both the olfactory and auditory systems do appear more complicated that the generalized mammal (Imam et al., 2018a, 2019b, c). While having an extensive tongue used in foraging (Doran & Allbrook, 1973), the tree pangolin shows a range of bipedal and quadrupedal locomotor styles allowing it to take advantage of both arboreal and terrestrial niches (Kingdon, 1971). It is in this context of tree pangolin behavior and phylogenetic relationships that the current findings are placed.

2 | MATERIALS AND METHODS

2.1 | Specimens

Adult tree pangolins (*Manis tricuspis*), caught from wild populations in Esejire, Osun State, Nigeria, were used in the current study (see Imam et al., 2017, for full details of animals, permits, and collection and treatment of tissue). All animals were treated and used according to the guidelines of the University of the Witwatersrand Animal Ethics Committee (AESC No. 2012/53/01), which parallel those of the NIH for the care and use of animals in scientific experimentation. In the current study, the brains of three of these tree pangolins, MT1 (male, body mass 2.44 kg, brain mass 10.69 g), MT3 (male, body mass 1.80 kg, brain mass 9.70 g), and MT5 (female, body mass 1.60 kg, brain mass 9.35 g), see Imam et al. (2017), were sectioned, stained, and analyzed.

2.2 | Sectioning and immunohistochemical staining

Prior to sectioning, each brain was allowed to equilibrate in 30% sucrose in 0.1 M PB at 4°C. The brains were then frozen in crushed dry ice and sectioned into 50-μm-thick sections on a freezing microtome. The whole brain of MT1 was sectioned in the coronal plane and a 1 in 10 series of sections taken and stained for Nissl, myelin, tyrosine hydroxylase (TH), orexin-A (OxA), serotonin (5HT), parvalbumin (PV), calbindin (CB), calretinin (CR), neurofilament H (NFH), and vesicular glutamate transporter 2 (vGlut2). The whole brain of MT3 was sectioned in the coronal plane and a 1 in 5 series of sections taken and stained for neuronal nuclear (NeuN) marker, choline acetyltransferase (ChAT), PV, CB, and CR. The right half of the brain of MT5 was sectioned in the sagittal plane and a 1 in 10 series of sections taken and stained for Nissl, myelin, TH, 5HT, PV, CB, CR, NFH, vGlut2, and doublecortin (DCX). All specimens were examined for the analysis presented herein, with the sagittally sectioned MT5 brain providing a useful comparison in terms of defining extents of cortical areas delineated in the coronal plane. The range of immunostains employed herein were selected to allow us to provide an accurate and well-supported architectonic analysis of the telencephalic pallium as well as the remainder of the brain not described in this article, but in associated papers. Some of the antibodies reported for use here, such as TH and 5HT, were very useful in other regions of the brain, but did not provide information of relevance to the current study, and thus were not reported on. Complete details of staining for Nissl and myelin staining, antibody characterization, specificity, and the protocol followed for all immunostains listed above have been provided previously (Imam et al., 2018a).

2.3 | Analysis and iconography

A low-power stereomicroscope was used to examine the sections and camera lucida drawings of the sections, outlining architectural borders were made. Architectonic borders were first defined using the standard Nissl and myelin stains. The parcellation of the cortical regions was then confirmed and refined using the immunohistochemical stains. The drawings were then scanned and redrawn using the Canvas Draw 6 program (Canvas GFX, Inc., FL, USA). The nomenclature used in the current study was based primarily on that used by Paxinos et al. (2009) for the rat, and Radtke-Schuller (2018) for the domestic ferret. While terminology is clearly variable across studies and species, where the terminology used in these atlases was not appropriate to the current observations, we used and cited the most appropriate terminology available. Digital photomicrographs were captured using an Axiocam 208 color camera mounted to a Zeiss Axioskop microscope. No pixilation adjustments, or manipulation of the captured images were undertaken, except for the adjustment of contrast, brightness, and levels using Adobe Photoshop.

TABLE 1 Stereological parameters used for estimating neuronal numbers in the white matter of the tree pangolin analyzed. **CR**, calretinin-immunopositive neurons; **NeuN**, neuronal nuclear marker-immunopositive neurons

Stain	Sectioning Plane	Counting frame size (μm)	Sampling grid size (μm)	Disector height (μm)	Section cut thickness (μm)	Measured mounted thickness (μm)	Upper and lower guard zones (μm)	Section interval	Number of sections	Number of sampling sites	Number of objects counted
NeuN	Coronal	150 × 150	600 × 600	20	50	26.4	2	80	11	486	957
CR	Coronal	150 × 150	600 × 600	18	50	23.2	2	40	11	383	247

2.4 | Stereological analysis

For the quantification of WMICs as revealed by NeuN and CR immunohistochemistry in MT3, we employed an unbiased design-based systematic random sampling stereological protocol. The stereological analysis was only undertaken in MT3, as this was the only brain in which we stained for NeuN, allowing determination of WMICs with certainty as compared to Nissl-stained material, and makes the counting procedure used herein comparable to that previously employed (e.g., Bhagwandin et al., 2020; Swiegers et al., 2018). We used an MBF Bioscience (Colchester, Vermont, USA) system with three plane motorized stage, Zeiss.Z2 vario axioimager and StereoInvestigator software (MBF, version 2018.1.1; 64-bit). Pilot studies for the NeuN and CR immunohistochemical stains were conducted to optimize sampling parameters, such as the counting frame and sampling grid size, and to achieve a coefficient of error (CE) below 0.1 (Dell et al., 2016; Gundersen, 1988; West et al., 1991). In addition, we measured the tissue section thickness at every sampling site, and the vertical guard zones were determined according to tissue thickness to avoid errors/biases due to sectioning artifacts (Dell et al., 2016; West et. al., 1991), all undertaken using a 40× objective. Table 1 provides a detailed summary of the parameters used in the current study. One specific concern with counting the WMICs is the determination of the border between the white matter and the deep border of layer 6, or other structures such as the putamen or claustrum. These borders were determined using the rapid decrease in neuronal density, the change in neuronal soma morphologies (as outlined in Mortazavi et al., 2016, Swiegers et al., 2019) and dendritic orientations, the dissolution of the microcolumnar organization of cortical neurons, and the significant decrease of any neuropil or background staining. The inner cortical borders were drawn using a 5× objective.

To estimate the total number of WMIC NeuN- or CR-immunoreactive neurons, we used the optical fractionator probe and the following equation (Dell et al., 2016; West et al., 1991):

$$N = Q/(SSF \times ASF \times TSF),$$

where N was the total estimated neuronal number, Q was the number of neurons counted, SSF was the fraction of the sections sampled, ASF was the area subfraction (which is calculated by the ratio of the size of the counting frame to the size of the sampling grid), and TSF was the thickness subfraction (which is calculated by the ratio of the disector height relative to the section thickness measured on the slide).

To determine NeuN- or CR-immunoreactive WMIC volumes, we used the nucleator probe, with a 40× objective. For all tissue sampled this probe was used concurrently with the optical fractionator while maintaining strict criteria, for example, only neurons with complete cell bodies were counted, and obeying all common stereological rules. As the samples violated the assumption of normality and homogeneity of variance, we report the median for neuronal volumes of WMICs as revealed by NeuN and CR immunostaining.

2.5 | Abbreviation list of anatomical structures

III – oculomotor nucleus
IV – trochlear nucleus
3a – rostral somatosensory area
3b – primary somatosensory area
3V – third ventricle
17 – primary visual area
18 – second visual area
19 – third visual area
20 – temporal visual cortex
21 – fourth visual area
ac – anterior commissure
AAF – anterior auditory field
Acb – nucleus accumbens
AHC – anterior hippocampal continuation
AI – primary auditory cortex
ALd – lateral auditory cortex, dorsal area
ALi – lateral auditory cortex, intermediate area
ALv – lateral auditory cortex, ventral area
Amyg – amygdaloid body
AOB – accessory olfactory bulb
AON – anterior olfactory nucleus
BNST – bed nuclei of the stria terminalis
ca – cerebral aqueduct
Cb – cerebellum
cc – corpus callosum
cic – commissure of the inferior colliculus
Cl – claustrum
Cli – claustrum, inner division
Clo – claustrum, outer division

D – dorsal nucleus (Clarke)
DB – diagonal band of Broca
DC – cingulate cortex, dorsal area
DEn – dorsal endopiriform nucleus
df – dorsal fornix
DT – dorsal thalamus
ec – external capsule
Ect – ectorhinal cortex
EGP – external globus pallidus
En – endopiriform nucleus
ER – entorhinal cortex
f – fornix
fi – fimbria of the hippocampus
fr – fasciculus retroflexus
GC – central gray matter
Hb – habenular nuclear complex
Hbc – habenular commissure
hc – hippocampal commissure
Hip – hippocampus (cornu ammonis, dentate gyrus, subiculum)
Hyp – hypothalamus
i – inner layer of subcortical white matter
IC – inferior colliculus
ic – internal capsule
ICjM – islands of Calleja, major island
IEn – intermediate endopiriform nucleus
IG – induseum griseum
IGP – internal globus pallidus
Ins – insular cortical area
IP – interpeduncular nucleus
LEC – lateral entorhinal cortex
lfp – lateral fasciculus of the pons
LGd – lateral geniculate nucleus, dorsal part
lot – lateral olfactory tract
LPO – lateral preoptic area
LSS – lateral suprasylvian cortex
lss – lateral stripe of the striatum
LV – lateral ventricle
m – middle layer of subcortical white matter
M1 – primary motor cortex
mcp – middle cerebellar peduncle
MEC – medial entorhinal cortex
MnPO – median preoptic nucleus
MOB – main olfactory bulb
MSS – medial suprasylvian cortex
NLOT – nucleus of the lateral olfactory tract
Nv – navicular nucleus of the basal forebrain
o – outer layer of subcortical white matter
OC – optic chiasm
OL – lateral orbital cortex
OM – medial orbital cortex
OT – optic tract
OV – ventral orbital cortex
ov – olfactory ventricle
P – putamen nucleus
PC – cerebral peduncle
pc – posterior commissure
PFCd – prefrontal cortex, dorsal area
PIRa – anterior piriform cortical region
PIRp – posterior piriform cortical region
POR – postrhinal cortical area
PP – posterior parietal cortex
Pre-M – premotor cortical area
PRhd – perirhinal cortex, dorsal area
PRhv – perirhinal cortex, ventral area
PSd – postsplenial cortex, dorsal area
PSi – postsplenial cortex, intermediate area
PSv – postsplenial cortex, ventral area
PVS – parietoventral somatosensory area
R – reticular thalamic nucleus
Rmc – red nucleus, magnocellular part
RSp – retrosplenial cortical area
S – septal nuclear complex
SII – second somatosensory area
SIII – third somatosensory area
SC – superior colliculus
SFO – subfornical organ
SMA – supplementary motor area
smt – stria medullaris of the thalamus
SO – superior olivary nuclear complex
SON – supraoptic nucleus
st – stria terminalis
STN – subthalamic nucleus
Str – striatum (caudate, putamen and accumbens nuclei)
SVA – splenial visual area
TTd – taenia tecta, dorsal part
TTv – taenia tecta, ventral part
Tu – olfactory tubercle
VC – cingulate cortex, ventral area
VEn – ventral endopiriform nucleus
VP – ventral pallidum
VPO – ventral pontine nucleus
VSS – ventral suprasylvian cortex
xscp – decussation of the superior cerebellar peduncle
zi – zona incerta

3 | RESULTS

Here, we provide a detailed cyto-, myelo-, and chemoarchitectonic description of the adult derivatives of the portions of the tree pangolin pallial telencephalon that have not been described previously (e.g., Imam et al., 2017; 2018a; 2019a; 2022a, b). These structures include the claustrum and endopiriform nuclei, the white matter and WMICs, as well as the various areas of the cerebral cortex. While the tree pangolin pallial telencephalon presents with an organization that resembles that previously reported in a range

of mammalian species, the organization of this region of the brain appears to be most similar to that observed in previously studied carnivores.

3.1 | Claustrum and endopiriform nuclear complex

The claustrum and endopiriform nuclear complex were located in the lateral and ventral aspects of the rostral half of the cerebral hemisphere, in a relative location typical of that observed across mammals (Figure 1; Smith et al., 2018). In the tree pangolin, this nuclear region was separated from the putamen nucleus by the white matter external capsule, but no extreme capsule separating these nuclei from the overlying cortex was present, although a thin neuropil band of low neuronal density was found between these nuclei and the overlying cortex (Figures 2 and 3).

Variances in the patterns of staining allowed parcellation of the claustrum into inner (Cli) and outer (Clo) divisions (Figures 1–4). Rostrally, the Clo was observed as patches within a broader Cli (Figure 1f, g), but caudally, the Cli and Clo formed two distinct parallel bands (Figure 1h–o). The density and NeuN marker immunostaining intensity of the neurons within the Cli was lower than that observed in the Clo, with the neurons oriented parallel to the outer border of the external capsule in the Cli, while those in the Clo showed a varied orientation (Figures 2a, 3a, and 4a, b). The density of myelinated fibers in the Cli was slightly higher than that of the Clo (Figure 4f, g). Parvalbumin immunostaining revealed a low density of neurons and a low to moderate density terminal network in the Cli, whereas in the Clo, the density of both parvalbumin-immunopositive neurons and terminal networks was higher (Figures 2c, 3b, and 4k, l). Calbindin immunostaining revealed the opposite pattern, with a higher number of calbindin-immunopositive neurons and a denser terminal network in the Cli compared the Clo (Figures 2d, 3c, and 4p, q). The Cli evinced a significantly higher density of calretinin-immunopositive neurons than the Clo (Figures 2e, 3d, and 4u, v), although the density of calretinin-immunopositive terminals was higher in the Clo (Figure 4u, v). Neurofilament H-immunopositive soma and dendrites were observed in the Cli, whereas in the Clo, only a low density of immunopositive dendrites was observed (Figures 2f and 4z, a'). These variances allowed the delineation and definition of these two claustral divisions in the tree pangolin.

Within the endopiriform nuclear complex, which was found deep to the lateral aspect of the cerebral cortex, three specific nuclei could be identified, the dorsal (DEn), ventral (VEn), and intermediate (IEn) nuclei (Figure 1). The DEn was the largest of these three nuclei and was observed throughout the dorsal rostro-caudal extent of the nuclear complex, while the smaller IEn was found ventrorostrally (Figure 1d–h) and the VEn ventrocaudally (Figure 1h–m). No distinct myelinated fiber tract separated the endopiriform nuclear complex from the overlying piriform cortex, although the thin cell-sparse neuropil band that separates the claustrum from the overlying lateral neocortex, continues ventrally to allow the distinction of the endopiriform nuclear complex from the piriform cortex (Figure 2a, b).

The density of neurons and the range of neuronal types in the DEn and VEn were quite similar, but both the VEn and IEn exhibited a lower neuronal density than the DEn (Figures 2a and 4c,d,e). A moderate density of myelinated fibers were observed in the DEn and VEn, with a substantially higher myelin density noted in the IEn (Figures 2b and 4h,i,j). In all three nuclei, parvalbumin-immunopositive neurons were observed, but these neurons in the IEn were visibly larger than those in the DEn and VEn (Figures 2c and 4m,n,o). In addition, the density of the parvalbumin-immunopositive terminal networks were greater in the DEn than both the VEn and IEn (Figures 2c and 4m,n,o). A low to moderate density of calbindin-immunopositive neurons were noted in all three nuclei, and while the size and types of these neurons appeared similar in the DEn and VEn, those in the IEn were composed of both smaller neurons (similar to those in the DEn and VEn) and larger neurons (Figures 2d and 4r,s,t). A moderate density of calretinin-immunopositive neurons was present in the DEn and VEn, while a lower density of smaller calretinin-immunopositive neurons was found in the IEn (Figures 2e and 4w,x,y). Neurofilament H-immunopositive soma and dendrites were observed in all three nuclei, all at a moderate density. These combinations of features allowed the division and delineation of the endopiriform nuclear complex into the three nuclei described herein.

3.2 | Cerebral white matter

3.2.1 | Deep cerebral white matter tracts

A significant proportion of the telencephalon is occupied by white matter pathways in the tree pangolin brain. In the tree pangolin, we could readily observe commissural, association, and projection pathways. The major commissural pathways readily identified include the corpus callosum, anterior commissure, and hippocampal commissure, while the most readily identified projection pathway was the internal capsule. Specific intratelencephalic association pathways could not be identified with certainty; however, the association pathways did evince a very distinct anatomical organization. We identified that the association white matter in the brain of the tree pangolin appears to be formed of three layers, outer, middle, and inner (Figures 5 and 6). The layering of the white matter in the tree pangolin is evident with Nissl, myelin, and parvalbumin immunostaining. The outer layer, lying directly deep to the inner border of cortical layer VI, was composed of intensely silver-stained myelin fascicles, that in coronal sections appeared to be oriented mostly rostrocaudally (Figure 5c,d). In addition, this outer layer evinced a high density of parvalbumin-immunopositive axons (Figure 5e,f). The staining intensity and orientation of the myelinated fascicles forming the middle layer was slightly different to that of the outer layer, showing a less intense silver-staining (Figure 5c,d) and a lower density of parvalbumin-immunopositive axons (Figure 5e,f). Interestingly, this middle layer appears to have a higher density of glial cells, as revealed with Nissl staining, that either the outer or inner layers (Figure 5a,b). The inner layer shows a Nissl and myelin staining similar to that of the outer layer (Figure 5a–d), but the

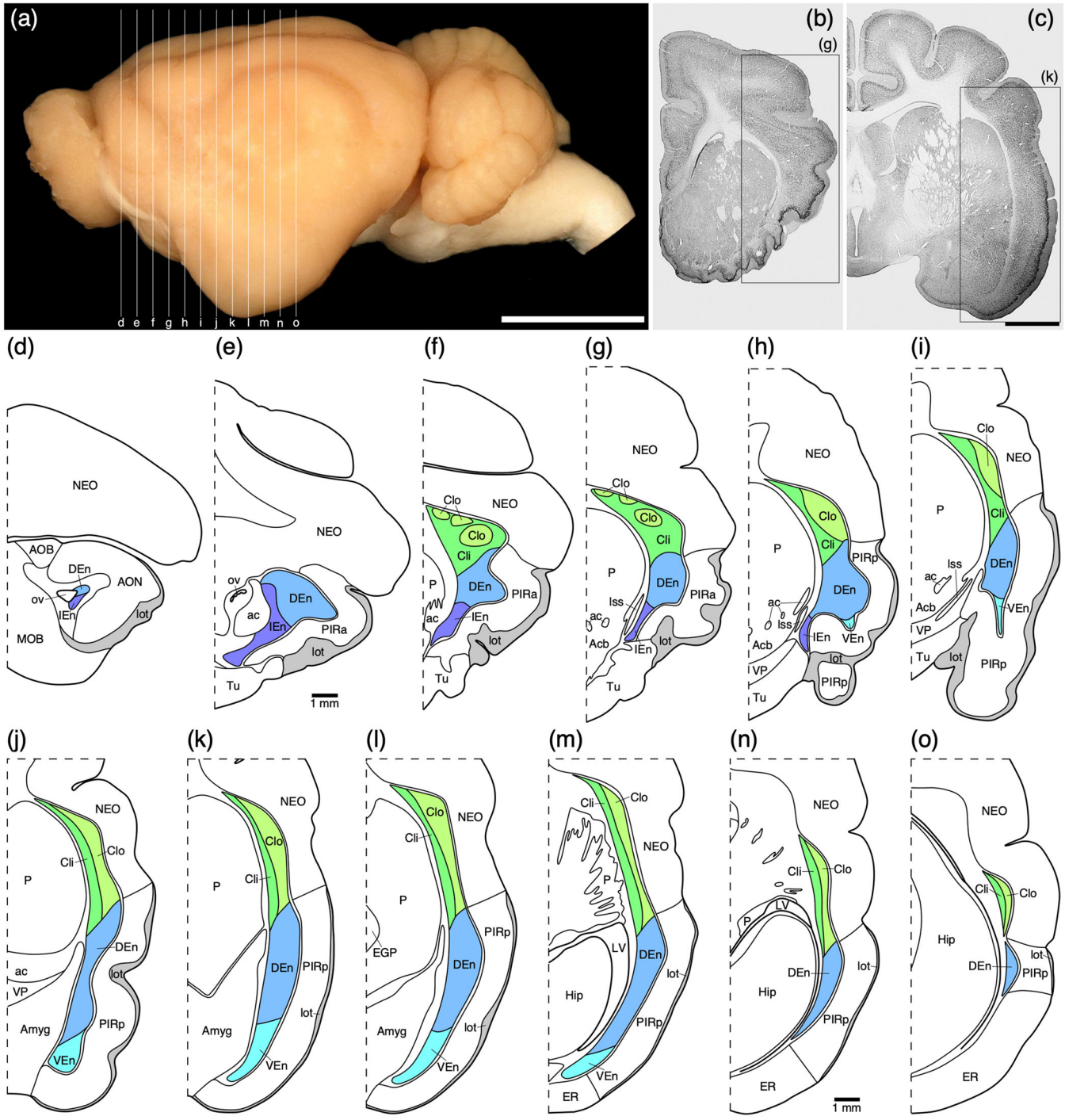

FIGURE 1 (**a**) Photograph of the lateral surface of the brain of the tree pangolin showing the levels at which the coronal sections imaged (b, c) and reconstructed (**d**–**o**) were taken. Scale bar in (**a**) = 1 cm and applies to (**a**) only. (**b**, **c**) Photomicrographs of coronal sections through the tree pangolin telencephalon, taken at the levels corresponding to (**g**) and (**k**) in (**a**), showing examples of the regions that were magnified and reconstructed (boxed regions), in these two cases diagrams (**g**) and (**k**) specifically. Scale bar in (**c**) = 3 mm and applies to (**b**) and (**c**). (**d**–**o**) Diagrammatic reconstructions delineating the claustrum and endopiriform nuclear complex of the tree pangolin. In all diagrams, dorsal is to the top and medial to the left. Diagram (**d**) represents the most rostral section drawn, while diagram **o** represents the most caudal section. Each diagram is approximately 1000 μm apart. The various nuclei or subdivisions of the claustrum and endopiriform nuclear complex are represented with differing colors, while the lateral olfactory tract is represented in gray. See list for abbreviations

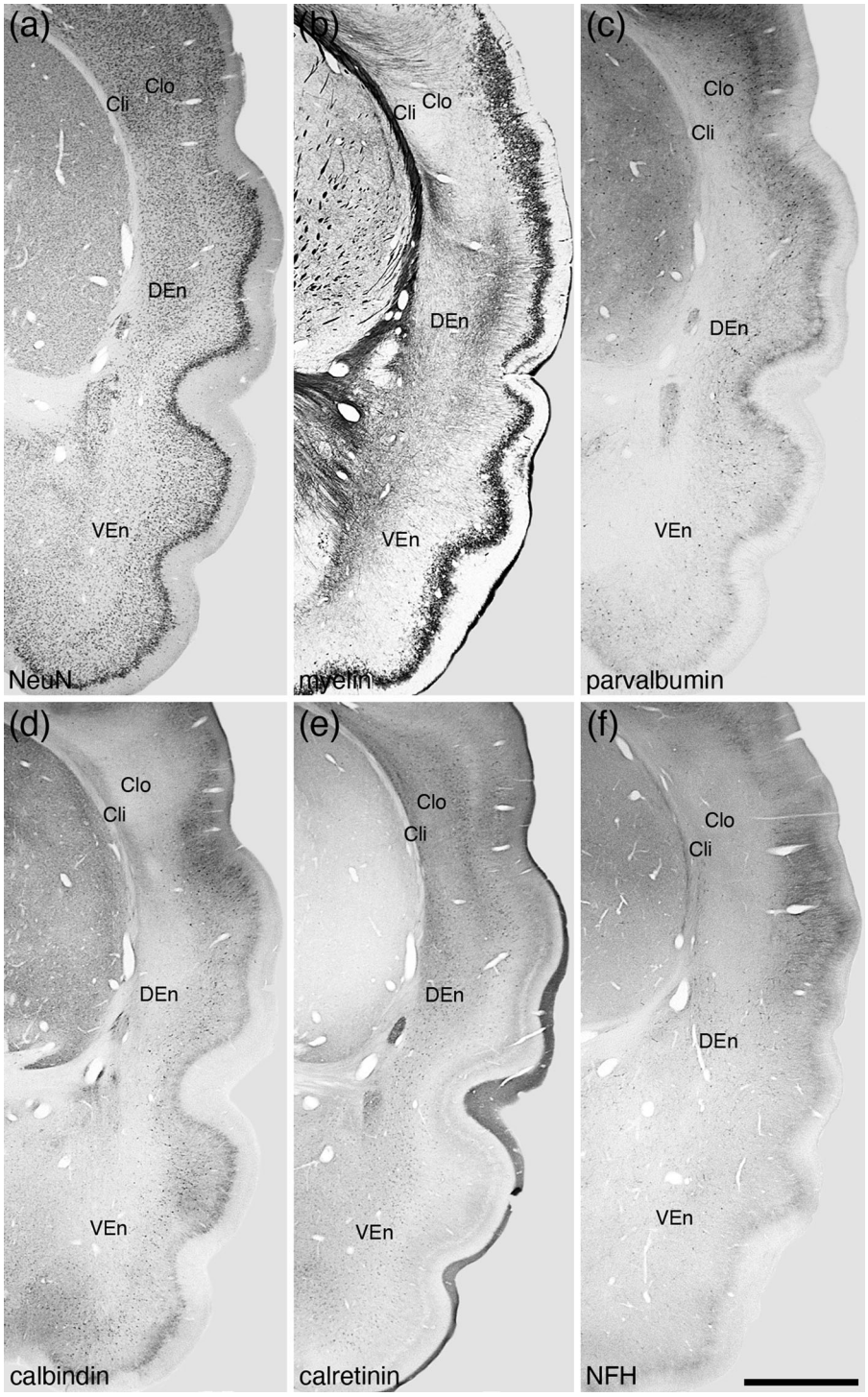

FIGURE 2 Photomicrographs of coronal sections through the claustrum (**Cl**) and endopiriform nuclear complex (**En**) of the tree pangolin stained for neuronal nuclear marker (**NeuN**, **a**), myelin (**b**), parvalbumin (**c**), calbindin (**d**), calretinin (**e**), and neurofilament H (**NFH**, **f**). Using this range of stains, the claustrum of the tree pangolin could be divided into inner (**Cli**) and outer (**Clo**) divisions, the differentiation of which is most clear in the parvalbumin (**c**), calbindin (**d**), calretinin (**e**), and neurofilament H (**f**) stained sections, but also apparent in the **NeuN** (**a**) and myelin (**b**) stains. The **En** could be divided into dorsal (**DEn**), ventral (**VEn**) and intermediate nuclei (IEn, not depicted), the distinction between **DEn** and **VEn** being primarily based on the calbindin (**d**) and calretinin (**e**) immunostaining. In all photomicrographs, medial is to the left and dorsal to the top. Scale bar in (**f**) = 2 mm and applies to all. See list for abbreviations

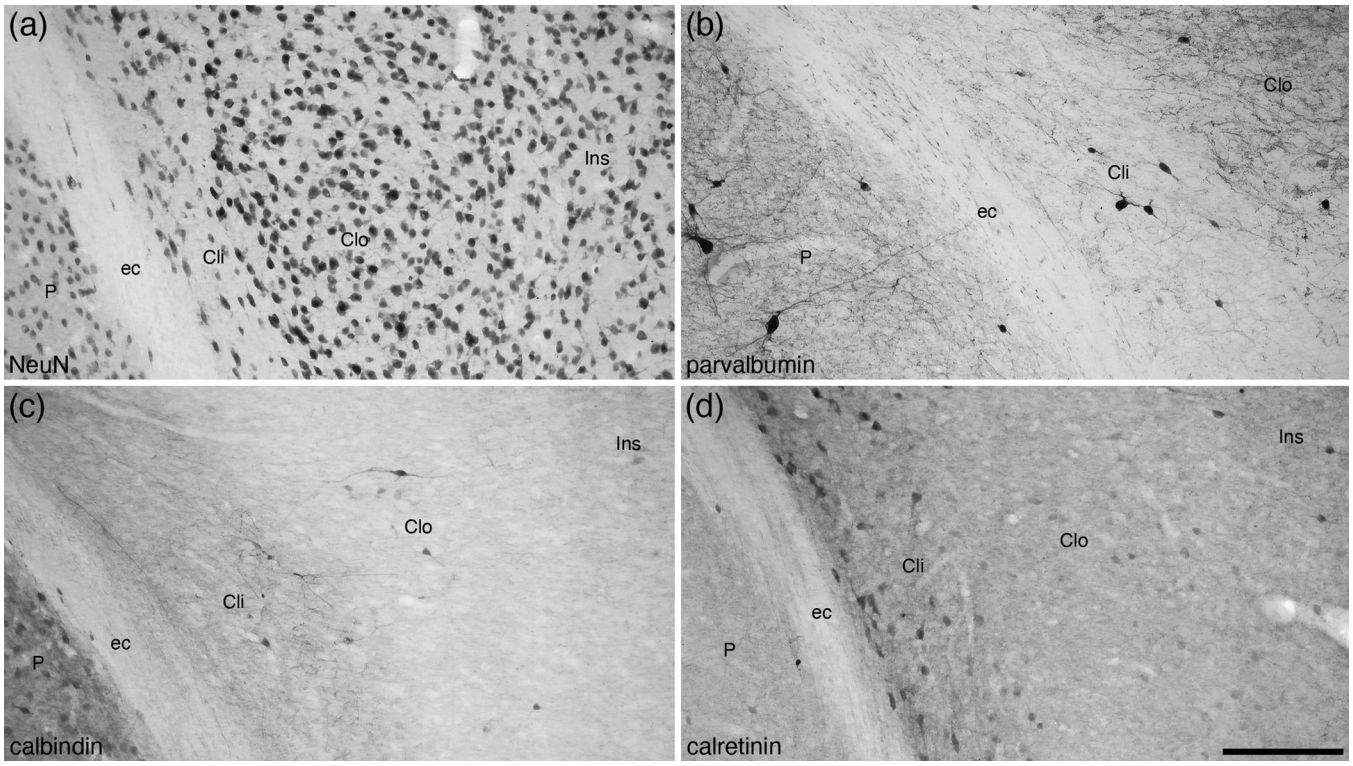

FIGURE 3 Photomicrographs of coronal sections through the tree pangolin brain showing the architectural appearance of the inner (**Cli**) and outer (**Clo**) divisions of the claustrum stained for neuronal nuclear marker (**NeuN**, **a**), parvalbumin (**b**), calbindin (**c**), and calretinin (**d**). Note the variation in cellular architecture (**a**) and the patterns of immunostaining (**b**-**d**) between the inner and outer divisions and the insular cortex (**Ins**). Also note the absence of an extreme capsule separating the **Clo** from the **Ins**, although a clear external capsule (**ec**) separates the **Cli** from the putamen (**P**). In all photomicrographs, medial is to the left and dorsal to the top. Scale bar in (**d**) = 200 μm and applies to all

density of parvalbumin-immunopositive axons is higher than the middle layer, but not as dense as the outer layer (Figure 5e,f). These features are those used to delineate and demarcate the three layers of the subcortical associational white matter in the tree pangolin (Figure 6).

3.2.2 | White matter interstitial cells

The range of stains used in the current study revealed the presence of WMICs (Figure 7). WMICs were revealed with the NeuN marker, parvalbumin and calretinin immunostains, although we recognize that a broader range of neurochemical types are likely to be revealed with additional immunostains, such as for neuronal nitric oxide synthase (e.g., Swiegers et al., 2018), somatostatin, neuropeptide Y, or neurotensin (e.g., Barbaresi et al., 2015; Tomioka & Rockland, 2007). With the NeuN immunostaining, neurons were observed throughout the subcortical white matter, but the greatest density of these neurons were in the outer layer of white matter (Figure 7a,c). A range of neuronal WMIC types were observed, and stereological analysis revealed that the median volume of the soma of these NeuN-immunopositive WMICs was 1012.1 μm^3 (range 294.8–2877.9 μm^3, 956 neurons analyzed). The total stereologically estimated number of NeuN-immunopositive WMICs was 3,231,332.

A small number of WMICs were parvalbumin-immunopositive (Figure 7d, g). Due to the small number of these neurons, no stereological analyses were undertaken. These primarily bipolar parvalbumin-immunopositive WMICs were found predominantly in the outer layer of white matter, close to the inner border of the cerebral cortex (Figure 7d, g). The number of primarily bipolar calretinin-immunopositive WMICs was substantially higher than that of the parvalbumin-immunopositive WMICs and exhibited a distribution similar to that of the NeuN-immunopositive WMICs (Figure 7e, h). Stereological analyses revealed that the median volume of the soma of these calretinin-immunopositive WMICs was 1088.1 μm^3 (range 174.8–2839.8 μm^3). The total stereologically estimated number of calretinin-immunopositive WMICs was 474,399, which represents approximately 14.7% of the entire WMIC population.

3.3 | Cerebral cortex

The cerebral cortex forms the dorsal, rostral, caudal, dorsomedial, lateral, and ventrolateral aspects of the tree pangolin brain (Figures 1, 6, and 8). The cerebral cortex of the tree pangolin contains both granular (with a layer 4) and agranular (without a layer 4) cortical regions. Within the granular regions layers 1– 6 are observed, while in the agranular

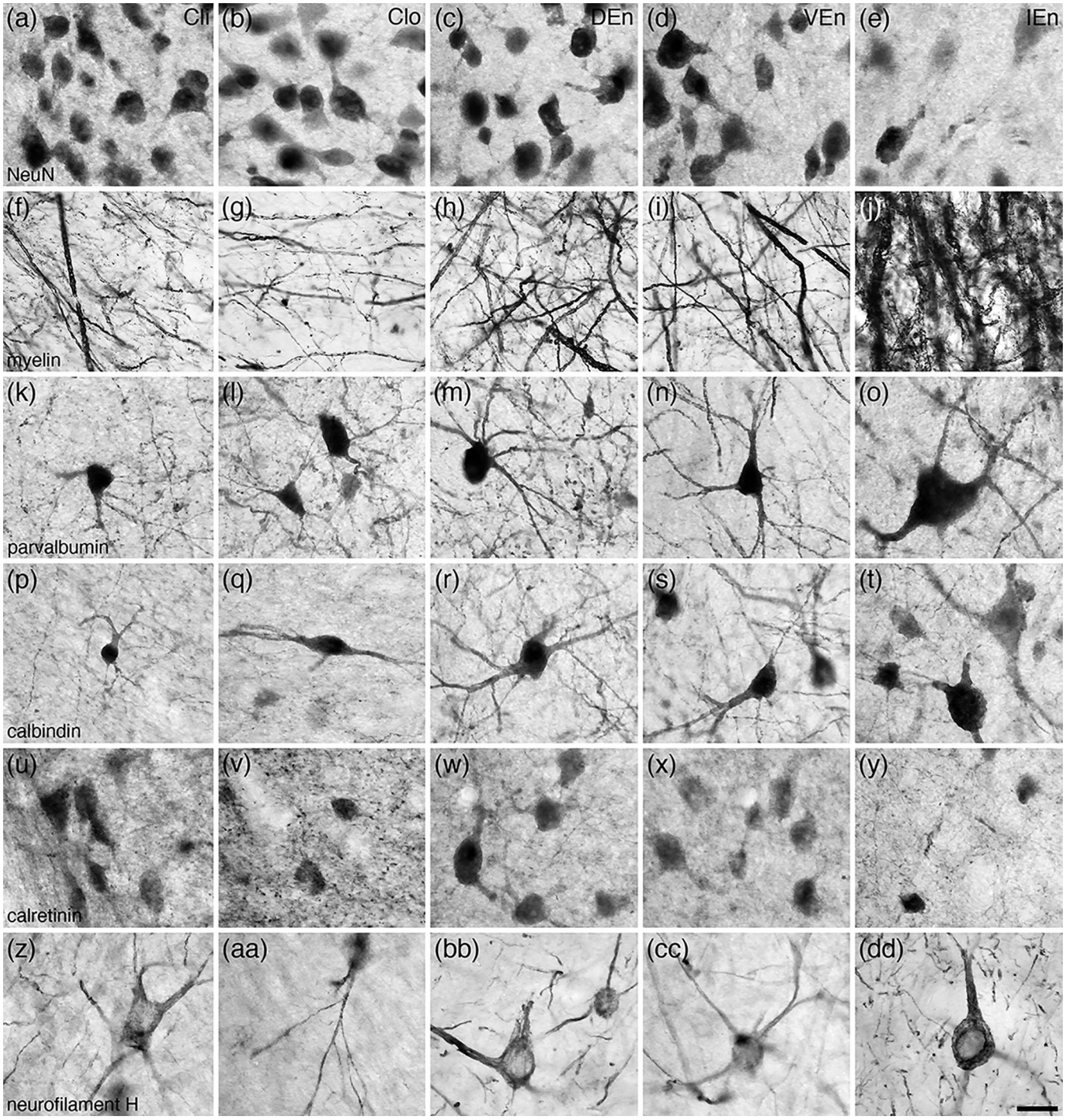

FIGURE 4 High magnification photomicrographs of coronal sections through the tree pangolin brain showing the architectural appearance of the nuclei forming the claustrum and endopiriform nucleus, including the inner division of the claustrum (**Cli**, **a**, **f**, **k**, **p**, **u**, **z**), the outer division of the claustrum (**Clo**, **b**, **g**, **l**, **q**, **v**, **aa**), the dorsal endopiriform nucleus (**DEn**, **c**, **h**, **m**, **r**, **w**, **bb**), the ventral endopiriform nucleus (**VEn**, **d**, **i**, **n**, **s**, **x**, **cc**), and the intermediate piriform nucleus (**IEn**, **e**, **j**, **o**, **t**, **y**, **dd**) nuclei stained for neuronal nuclear marker (**NeuN**, **a**-**e**), myelin (**f**-**j**), parvalbumin (**k**-**o**), calbindin (**p**-**t**), calretinin (**u**-**y**), and neurofilament H (**z**-**dd**). Note the variations in structural densities between the nuclei, which can be consistently employed to determine the extent of each of these nuclei. In all photomicrographs, medial is to the left and dorsal to the top. Scale bar in (**dd**) = 20 μm and applies to all

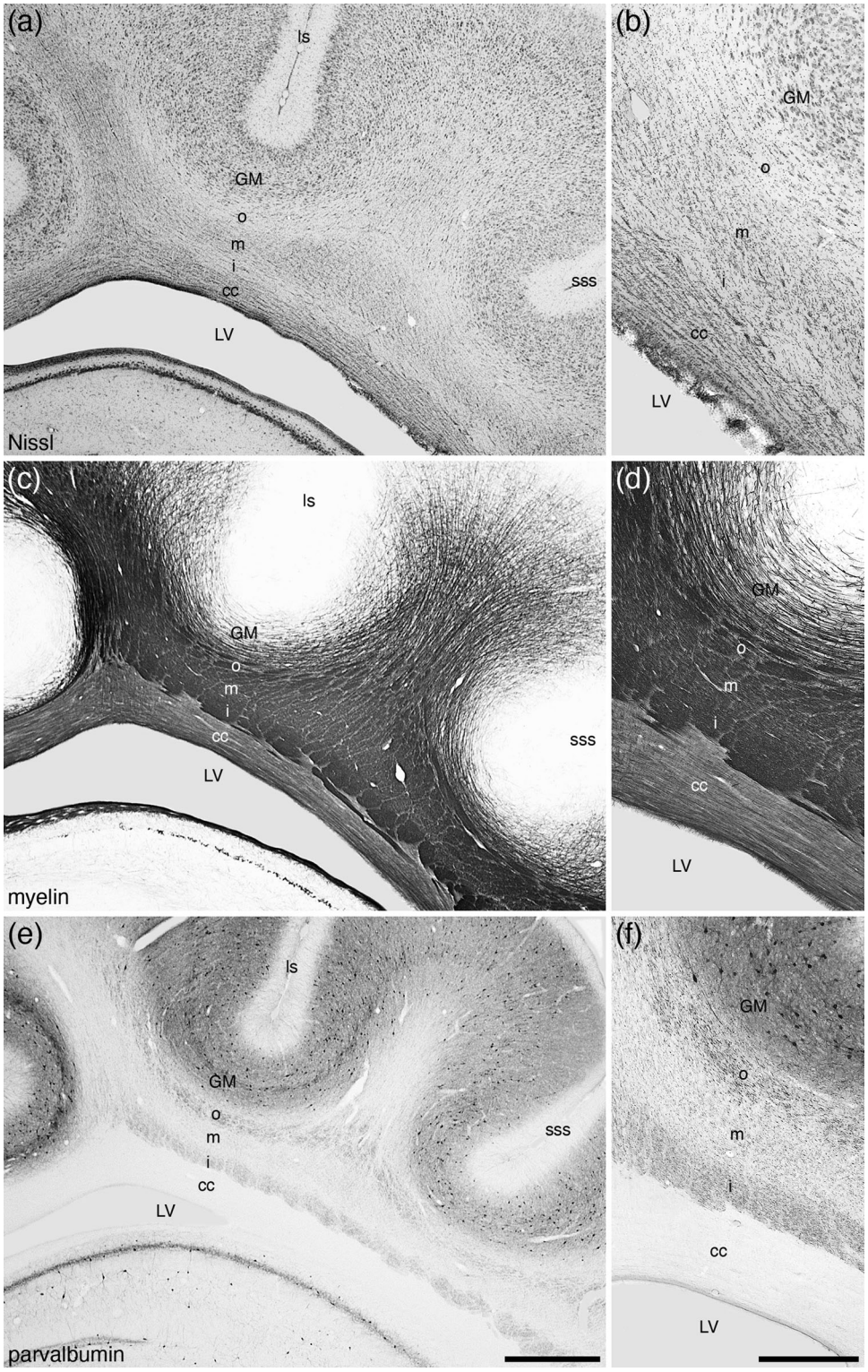

FIGURE 5 Lower (**a**, **c**, **e**) and higher (**b**, **d**, **f**) magnification photomicrographs of coronal sections through the white matter underlying the cerebral cortex (in this instance deep to the lateral, **ls**, and suprasylvian, **sss**, sulci) stained for Nissl (**a**, **b**), myelin (**c**, **d**), and parvalbumin (**e**, **f**) in the brain of the tree pangolin. Note how the cerebral white matter in this species forms three distinct layers, the outer (**o**), middle (**m**), and inner (**i**) layers, here imaged dorsal to the lateral expansion of the corpus callosum (**cc**) and the body of the lateral ventricle (**LV**). This lamination of the cerebral white matter, while distinct in both Nissl and myelin-stained sections, is particularly clear in the parvalbumin-stained sections (**e**, **f**). In all photomicrographs, medial is to the left and dorsal to the top. Scale bar in (**e**) = 1 mm and applies to **a**, **c**, and **e**. Scale bar in (**f**) = 500 μm and applies to **b**, **d**, and **f**

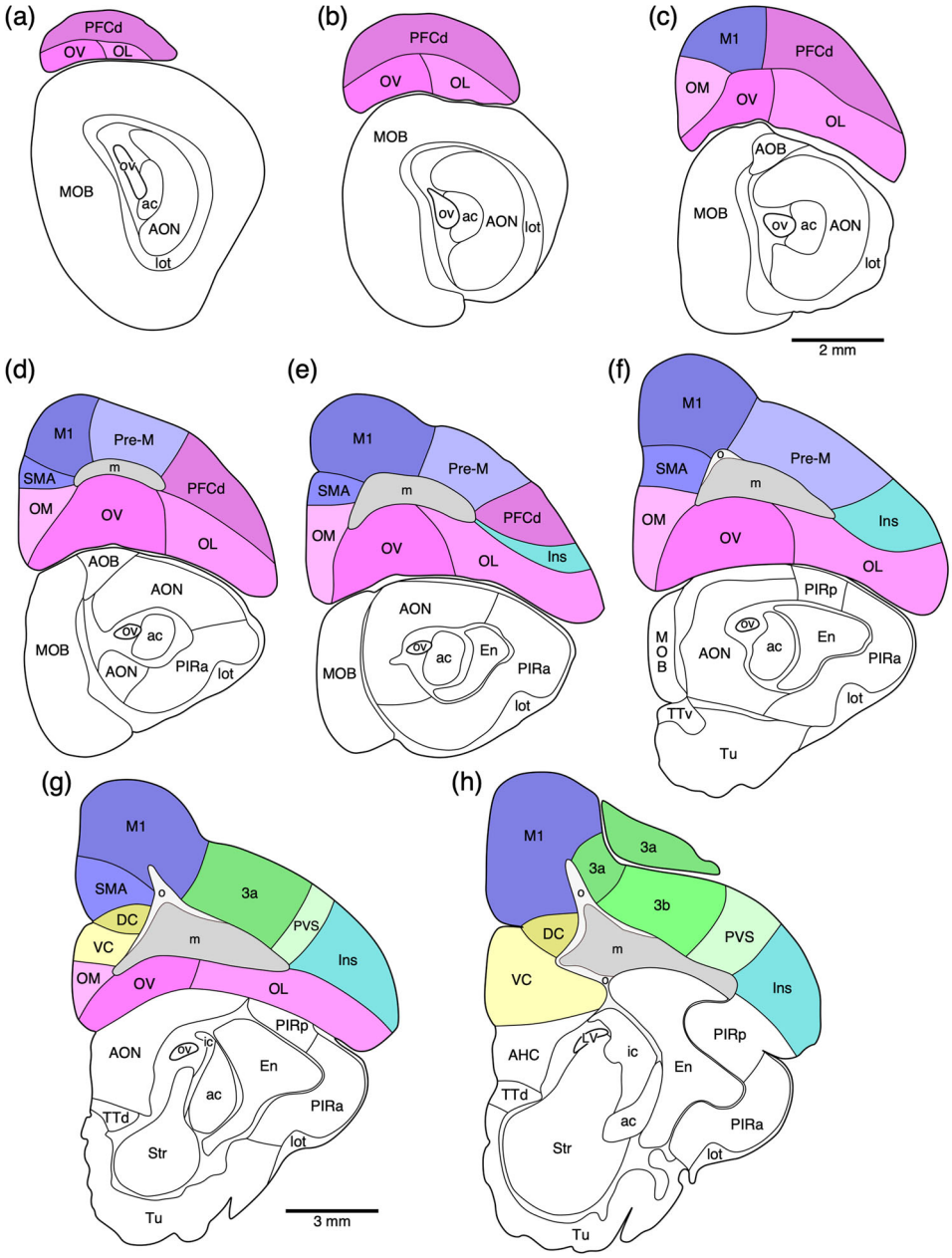

FIGURE 6 Diagrammatic reconstructions of coronal sections through the tree pangolin brain delineating the identified cortical areas and certain other subcortical structures. In all diagrams, dorsal is to the top and medial to the left. Diagram **a** represents the most rostral section drawn, while diagram **qq** represents the most caudal section. Each diagram is approximately 500 μm apart. The various cortical areas are represented with differing colors, with shades of the same colors identifying cortical regions. The layers of white matter are given in different shades of gray. See list for abbreviations

regions layers 1–3, 5, and 6 are observed. In all cortical areas, even the primary sensory regions, the laminar borders are not particularly sharp (Figure 9). A range of neuronal types are observed throughout the tree pangolin cerebral cortex (Figures 10–30), but it is of interest to note that both layers 2 and 4 do not contain a substantial number of granular neurons, these layers being primarily composed of pyramidal neurons (Figure 9). In addition, while layer 2 exhibits the expected higher density of neurons, as typically seen in mammals, layer 4 has a far lower density of neurons than generally observed for this cortical layer in mammals, perhaps due to the pyramidalization of the neuronal types forming this layer (Figure 9).

Our architectural analysis indicates that there are several cortical regions, each containing multiple, distinct cortical areas (Figures 6 and 8). Within the tree pangolin brain, in addition to the olfactory and limbic cortical regions previously described (Imam et al., 2018a, 2019a, 2022a), we noted putatively as there is no electrophysiological evidence to support these functionally assigned regions, a prefrontal cortical region, a motor cortical region, a somatosensory

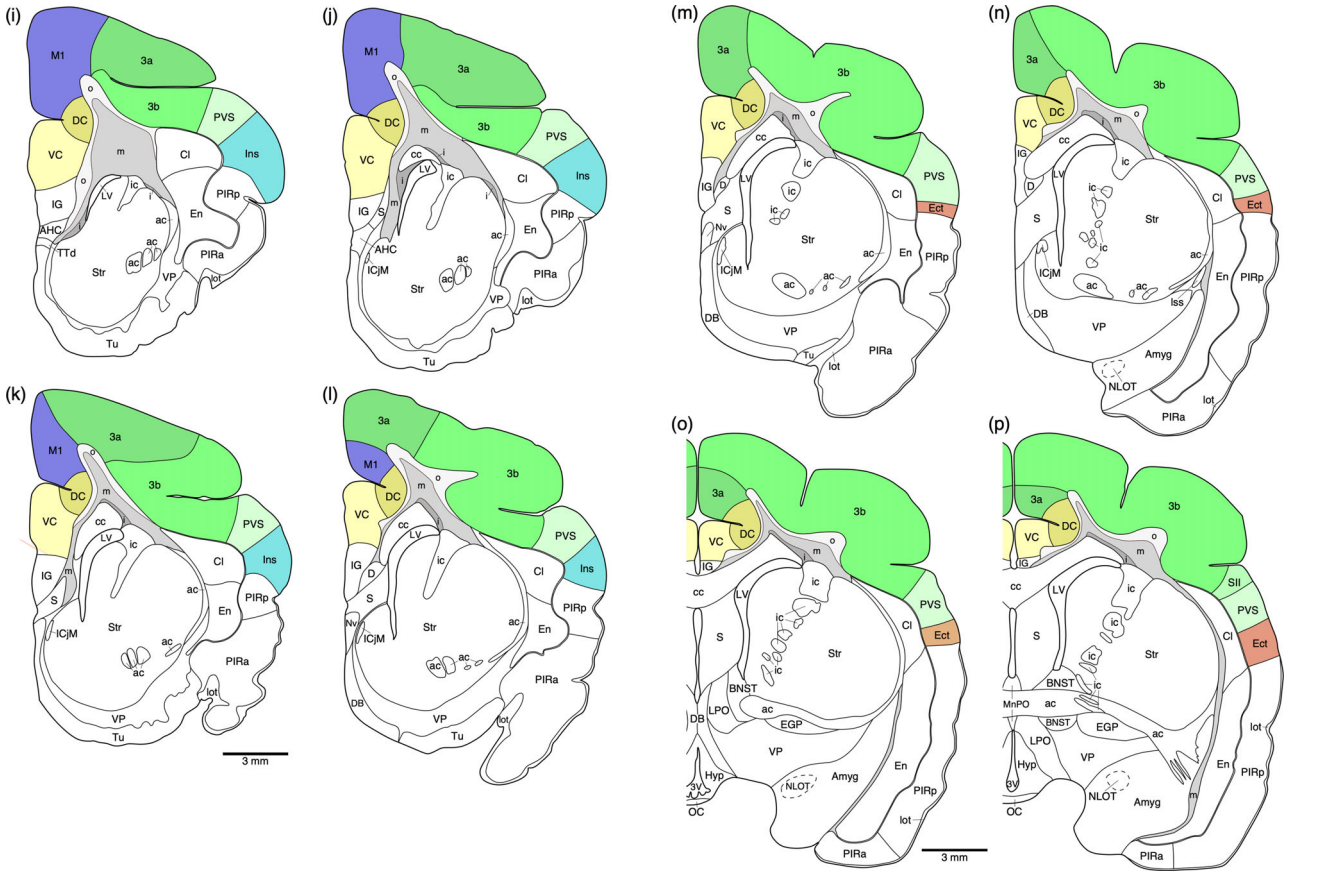

FIGURE 6 Continued

cortical region, a visual cortical region, an auditory cortical region, a pararhinal cortical region, a cingulate cortical region, and retrosplenial/postsplenial cortical region. The putative assignation of cortical regions and areas is based on comparisons primarily to carnivores, but also more broadly across mammals.

3.3.1 | The putative prefrontal cortical region

In the current analysis, we define the prefrontal cortical region as that cortex found rostral to the motor and premotor cortex (see below). Within this region of cortex, which occupies the rostral pole of the cerebral hemisphere or the orbital gyrus, we could distinguish four distinct cortical areas, a dorsal prefrontal cortical area (PFCd) located on the dorsolateral aspect of the hemisphere (Figures 6a–d and 8), and three (lateral—OL, ventral—OV, and medial—OM) prefrontal orbital cortical areas occupying the orbital frontal cortex (Figures 6a–d and 8). All four regions were agranular, in that a distinct layer 4 could not be identified, but the remaining five layers (1, 2, 3, 5, and 6) were identified in all cortical areas, although the layer borders were often indistinct (Figures 10 and 11).

The dPFC area (Figure 10a–h) exhibited a moderate density of neurons, with moderately dense myelination in layers 1, 5, and 6. Low densities of parvalbumin, calbindin, and calretinin neurons were observed throughout the layers, although a dense parvalbumin-immunopositive terminal network was present in layer 2. Vesicular glutamate transporter 2-immunoreactive boutons were observed in a low density throughout all layers, although layer 6 exhibited a higher density of these boutons. Neurofilament H-immunopositive neural structures exhibited a high density throughout layers 2–5, with lower densities in layers 1 and 6.

Within the OL (Figure 10i–p), distinct layer variations in neuronal density were observed, with layer 2 having the highest density, layers 5 and 6 having a moderate density with layer 3 having the lowest density apart from the cell sparse layer 1. Layers 1–3 exhibited a moderate density of myelinated fibers, while layers 5 and 6 had a higher myelin density. Parvalbumin-, calbindin-, and calretinin-immunopositive neurons were observed in a low density in layers 2–6. Vesicular glutamate transporter 2-immunoreactive boutons were observed in all layers, but with higher densities in layers 2 and upper layer 3. Neurofilament H-immunopositive neural structures were observed in all layers, with layer 3 exhibiting the highest density of labeled cells and dendrites, while layer 5 exhibited several immunopositive cell bodies.

Moderate densities of neurons were observed in layers 2–6 of the OV (Figure 11a–h), with layers 2 and 6 having slightly higher neuronal densities than layers 3 and 5. Layers 1 and 6 exhibited moderate densities of myelinated fibers, while layers 2, 3, and 5 had substantially lower myelin densities. A moderate density of parvalbumin-

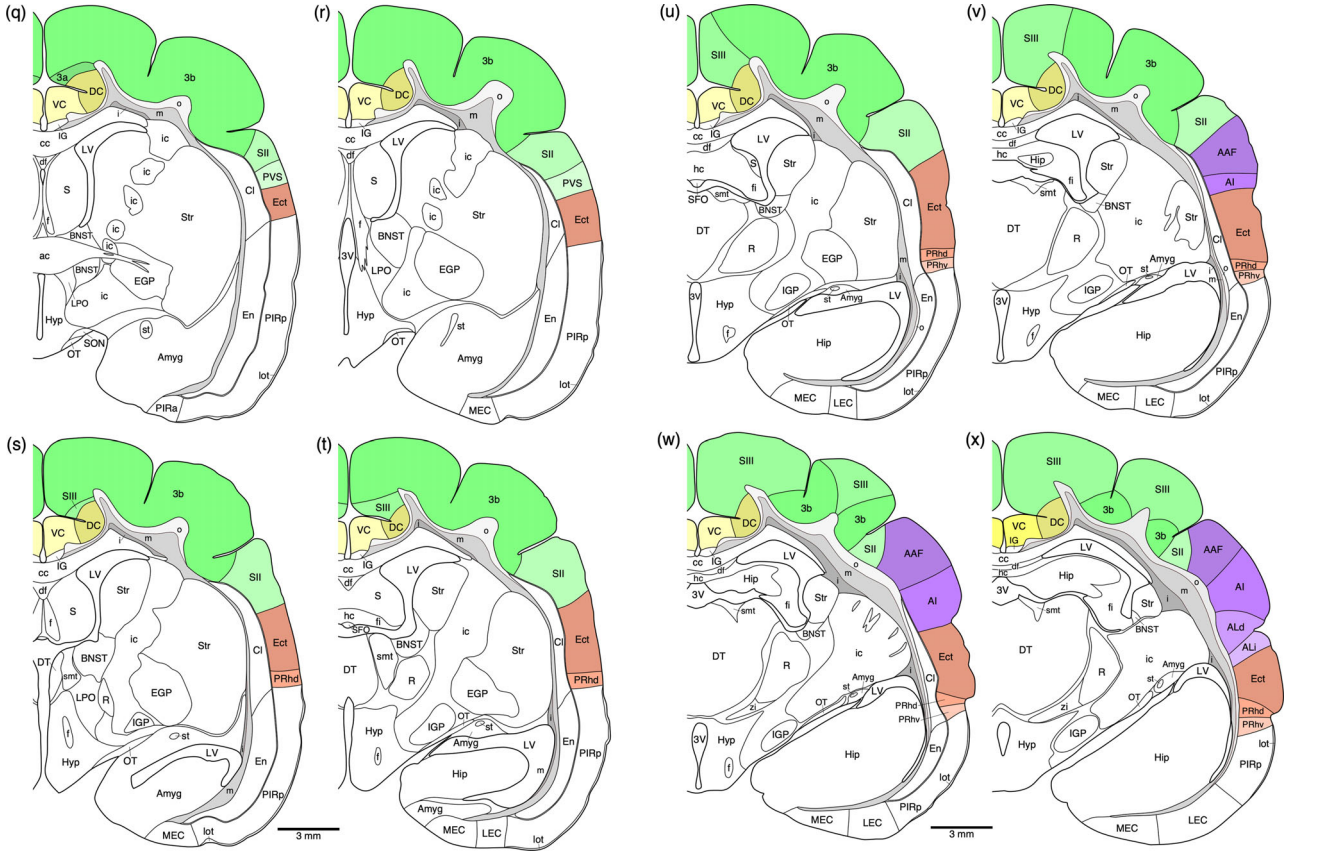

FIGURE 6 Continued

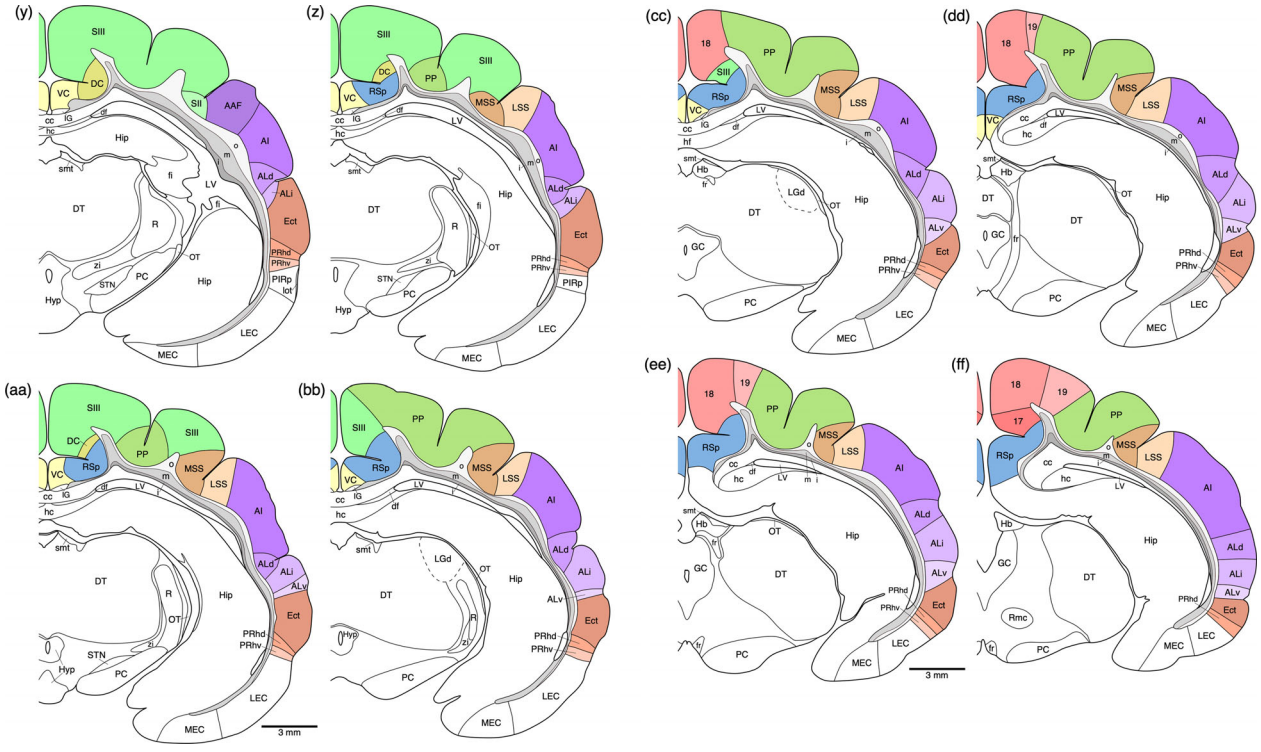

FIGURE 6 Continued

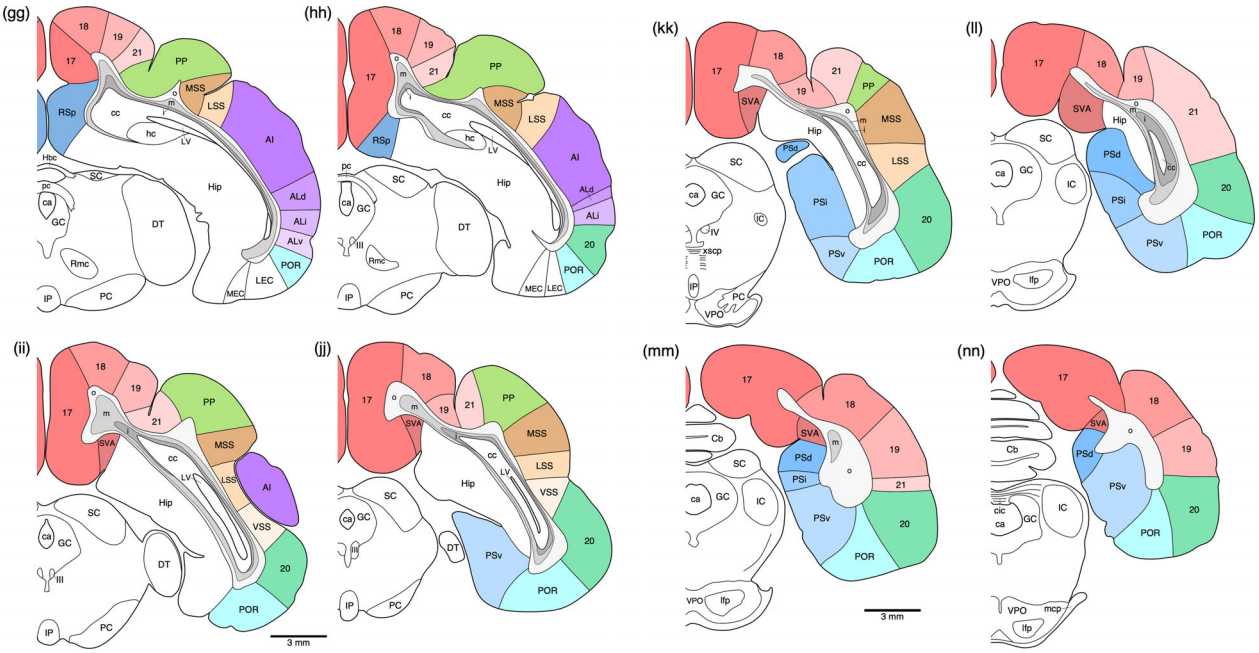

FIGURE 6 Continued

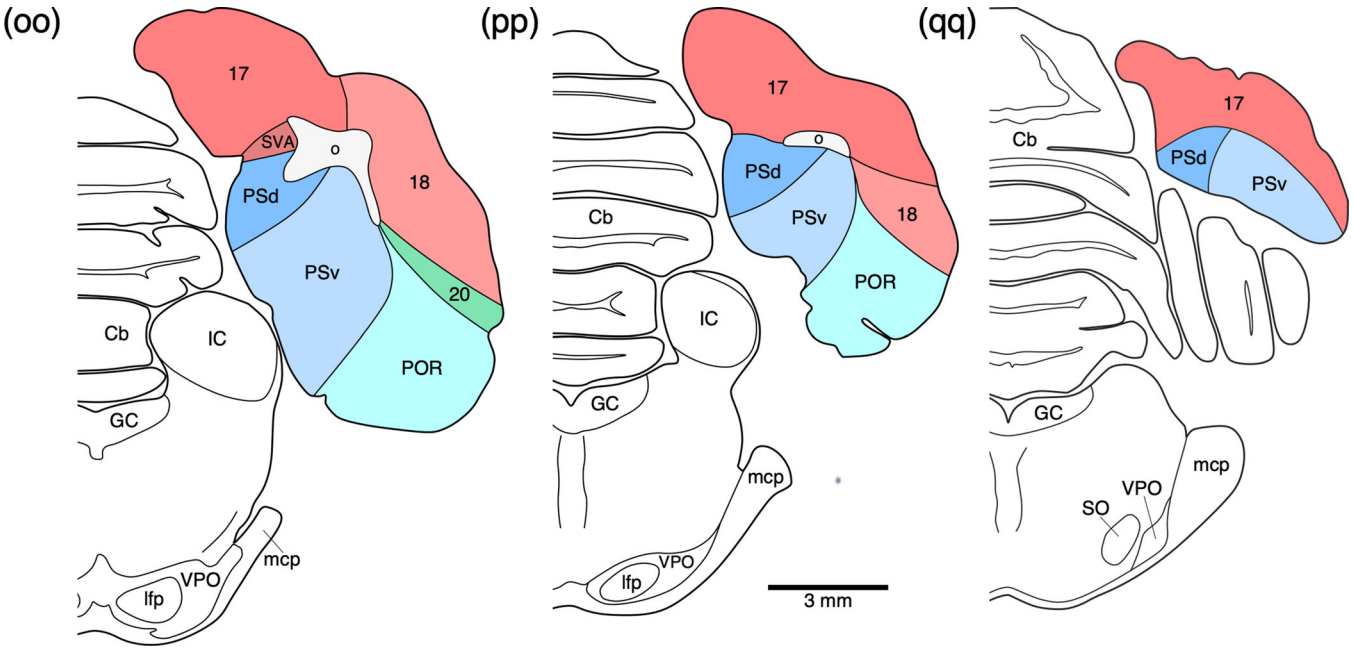

FIGURE 6 Continued

immunopositive neurons was observed in layers 2–6, with the density of these neurons being higher in layer 3. While layer 2 presented with a low-density parvalbumin-immunopositive terminal network, this was high in density in layer 3 and slightly lower in density in layers 5 and 6. Very few calbindin-immunopositive neurons were observed in the OV, primarily in layers 2 and 6, while a moderate density of calretinin-immunopositive neurons was noted in layers 3, 5, and 6. Vesicular glutamate transporter 2-immunoreactive boutons were observed in all layers, but a particularly high density of labeled boutons were observed in the upper half of layer 1. Moderate to low densities of neurofilament H-immunopositive neural structures were observed in layers 2–6.

The neuronal density throughout layers 2–6 of the OM (Figure 11i–p) were quite consistent, although layers 2 and 5 exhibited slightly higher densities. Myelin density was high in layers 3 and 5, lower in layers 6 and 1, with layer 2 showing a very low myelin density. A moderate density of parvalbumin-immunopositive neurons were observed in layers 2–6, with slightly higher densities of these neurons being observed in layers 3 and 6. A moderate- to high-density

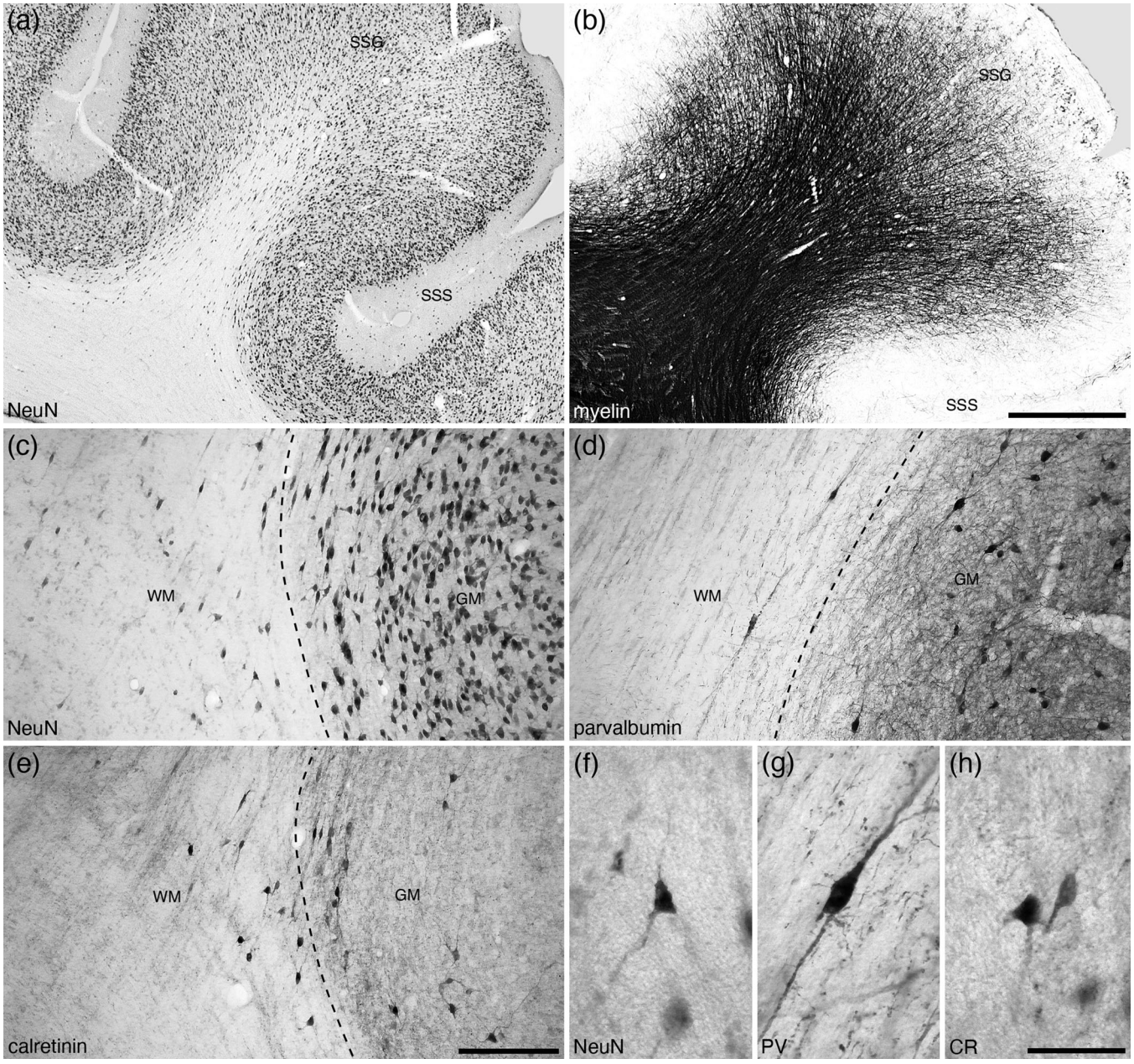

FIGURE 7 Photomicrographs, taken at various magnifications, of coronal sections through the cerebral cortex and underlying white matter of the suprasylvian gyrus (**SSG**) and sulcus (**SSS**) of the tree pangolin brain stained for neuronal nuclear marker (**NeuN**, **a**, **c**, **f**), myelin (**b**), parvalbumin (**d**, **g**), and calretinin (**e**, **h**), showing the distribution and density of the white matter interstitial cells (WMICs). Dashed lines in (**c**), (**d**), and (**e**) demarcate the approximate border between the cortical gray matter (**GM**) and the underlying white matter (**WM**). Note the presence of several WMICs in the white matter (**a**, **c**), some of which are parvalbumin-immunoreactive (**d**) and many more of which are calretinin-immunoreactive (**e**). In all photomicrographs, medial is to the left and dorsal to the top. Scale bar in (**b**) = 1 mm and applies to **a** and **b**. Scale bar in (**e**) = 200 μm and applies to **c**–**e**. Scale bar in (**h**) = 50 μm and applies to **f**–**h**

parvalbumin-immunopositive terminal network was observed in layers 2–6. Very few calbindin-immunopositive neurons were observed in OM, with these few neurons being located in layers 2 and 6, and palely stained calretinin-immunopositive neurons were observed layers 2–6. Vesicular glutamate transporter 2-immunoreactive boutons were observed in all layers, with the highest density of these boutons being observed in layer 2. Neurofilament H-immunopositive cell bodies were observed at a low density in layers 2 and 6, while higher densities of neurofilament H-immunopositive structures were observed in layers 3 and 5.

3.3.2 | The putative motor cortical region

The region of the tree pangolin cerebral cortex designated as a motor occupied the caudal aspect of the orbital gyrus, rostral aspect of the

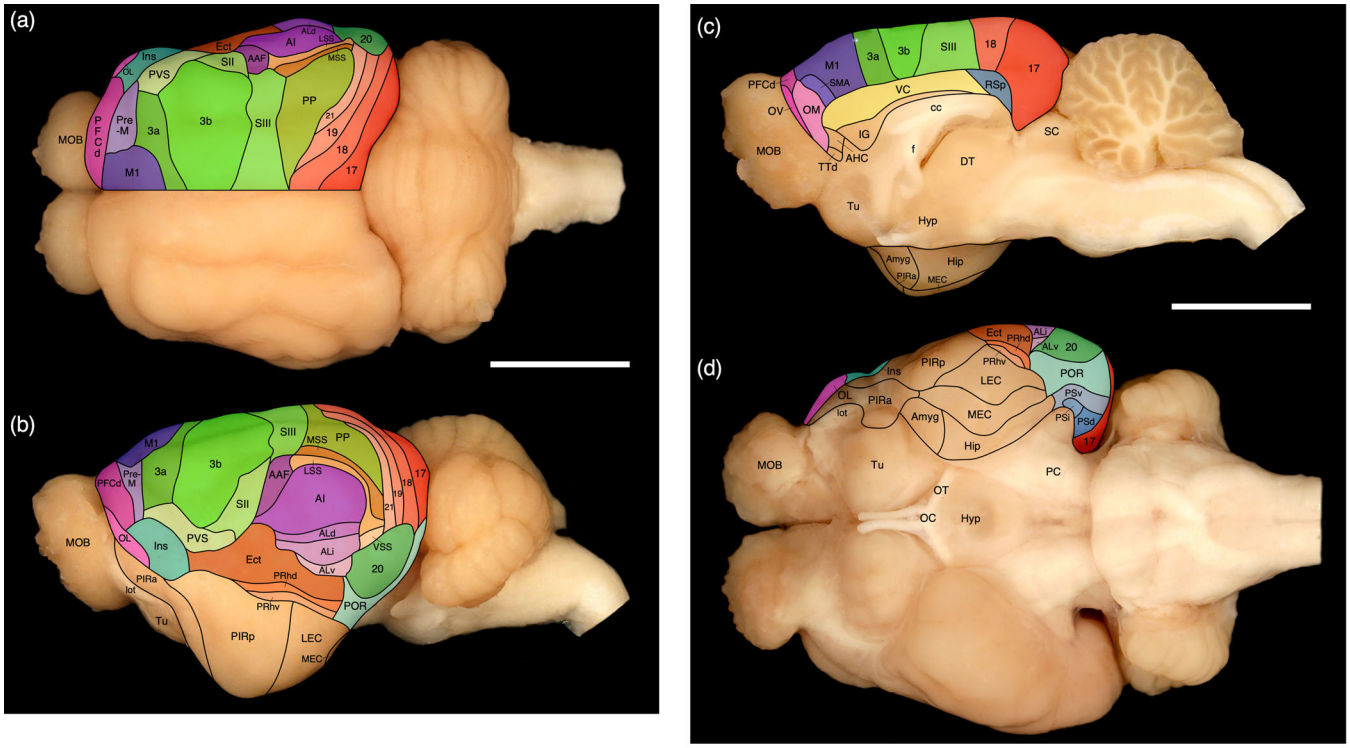

FIGURE 8 The locations of the various cortical areas of the tree pangolin (see Figure 6) superimposed on images of the brain: (**a**) dorsal view, (**b**) lateral view, (**c**) midsagittal view, and (**d**) ventral view. The colors of the cortical areas match those used in Figure 6. See list for abbreviations

sigmoid gyrus, the anterior portion of the lateral gyrus, and a portion of the medial wall of the cerebral hemisphere (Figures 6c–l and 8a–c). Within the motor cortex, we found evidence for three distinct cortical areas, the primary motor cortical area (M1), the supplementary motor cortical area (SMA), and the premotor cortical area (Pre-M) Figures 6c–l, 8a–c, 12, and 13a–h). All three cortical areas identified were agranular, in that a distinct layer 4 could not be identified, but the remaining five layers (1, 2, 3, 5, and 6) were identified, although the layer borders were often indistinct (Figures 12 and 13a–h).

Within M1 moderate variations in neuronal density were observed, with layers 2 and 5 exhibiting higher densities than layer 3 and 6, and a very low neuronal density being observed in layer 1 (Figure 12a–h). While layer 5 exhibited a higher neuronal density, no distinct gigantopyramidal neurons (Betz cells) were identified, although the general size of the neurons in layer 5 was larger than those seen in adjacent cortical areas. M1 was not heavily myelinated, with a low density of horizontally oriented axons at the layer1/2 boundary and a moderate density of myelin in layers 5 and 6. Only occasional parvalbumin-immunopositive neurons were observed in layers 2 and 5, with those in layer 2 being larger with distinct apical dendrites investing into layer 1. Layers 2–6 exhibited a high density of parvalbumin-immunopositive structures. Calbindin-immunopositive neurons were palely stained and found only in layers 2 and 3, while calretinin-immunopositive neurons were observed throughout layers 2–6. Vesicular glutamate transporter 2-immunoreactive boutons were observed in all layers, with the highest density of these boutons being observed in the very superficial part of layer 1 and a moderate density being observed in layer 3. NFH-immunopositive structures were observed in all cortical layers but were most dense in layers 2 and 3 where the occasional soma was immunolabeled.

The SMA has a very similar cyto- and myelo-architecture as seen in the M1, although both the density of neurons and myelinated axons is less (Figure 12i–p). Unlike M1, in the SMA, parvalbumin-immunoreactive neurons were observed in layers 3, 5, and 6, with the most neurons being observed in layers 3 and 6. Palely calbindin-immunopositive neurons were observed primarily in layer 2, with occasional neurons being observed in upper layer 3. Palely calretinin-immunopositive neurons were observed primarily in layer 3, with occasional neurons being observed in layer 2. Vesicular glutamate transporter 2-immunoreactive boutons were observed in all layers, with the highest density of these boutons being observed in the very superficial part of layer 1 and a moderate density being observed in layers 3 and 6. NFH-immunopositive structures were observed in all cortical layers, but the highest density of these was observed in layers 5 and 6, while occasional immunolabeled soma were observed in layer 3.

Within the PMA, the variation in neuronal densities was not as pronounced as observed in M1 and SMA, although layers 2 and 5 appear to have slightly higher neuronal densities than layers 3 and 6 (Figure 13a–h). The upper portion of layer 1 exhibited numerous horizontally oriented myelinated fibers, while lower layer 1 and layer 2 were myelin sparse. A moderate to high density of myelinated fibers was observed in layers 3–6, with radially arranged myelin fascicles being observed in layers 5 and 6. A low density of parvalbumin-immunopositive

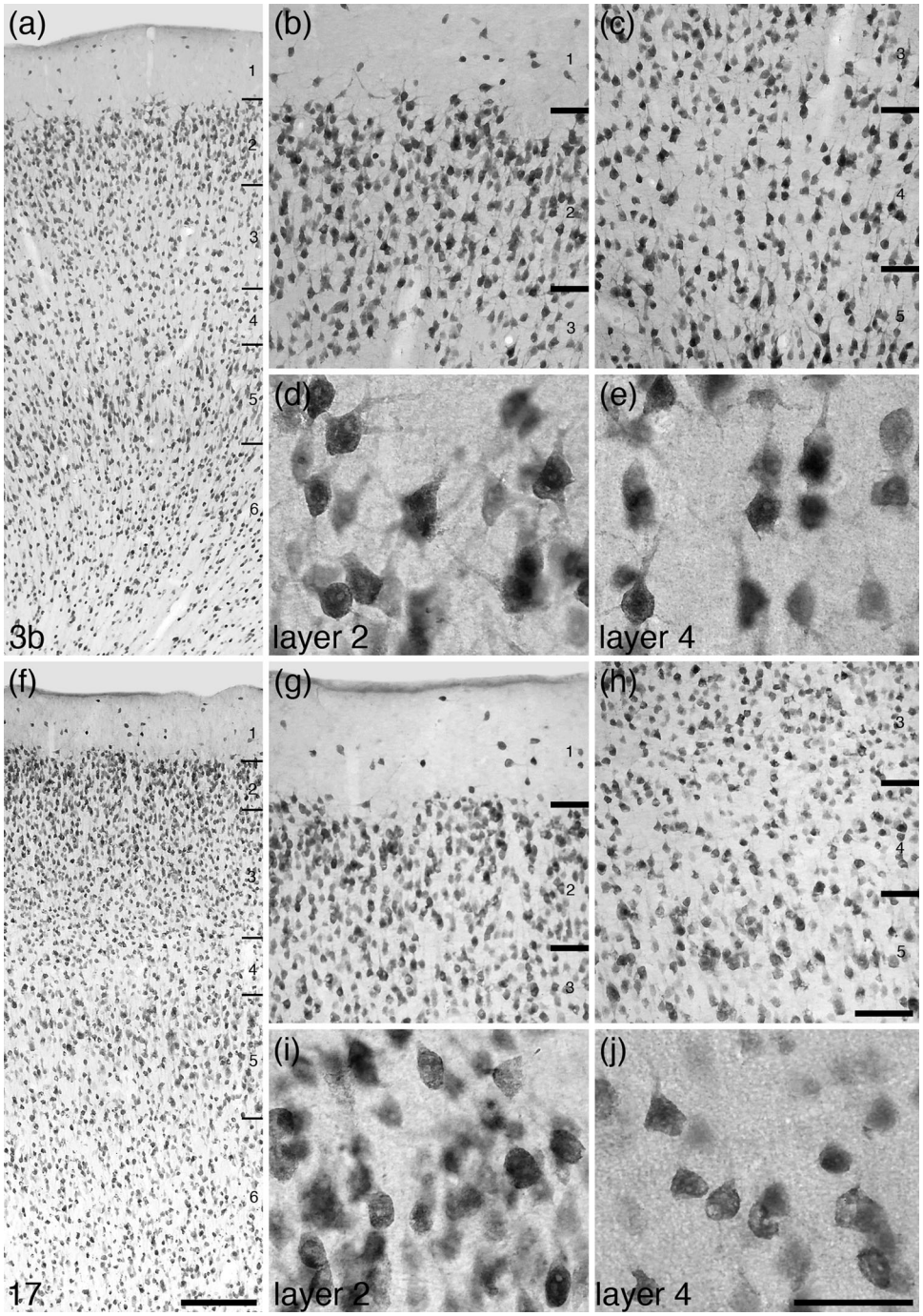

FIGURE 9 Photomicrographs at different magnifications of neuronal nuclear marker immunostaining coronal sections through the primary somatosensory (Brodmann area **3b**, **a**–**e**) and primary visual (Brodmann area **17**, **f**–**j**) cortical areas. In the cortex of the tree pangolin, the neurons of layers 2 and 4 appear to primarily consist of pyramidal neurons (layers labeled in **a**-**c** and **f**-**h**), rather than the typically reported granular neurons (**d**, **e**, **i**, **j**). Also note that layer 2 exhibits a high neuronal density, while layer 4 is a region of lower neuronal density. These characteristics of the cerebral cortex (only the granular cortex regarding layer 4) are found throughout the cerebral cortex of the tree pangolin. In all images, the pial surface is to the top. Scale bar in **f** = 250 μm and applies to **a**, **f**. Scale bar in **h** = 100 μm and applies to **b**, **c**, **g**, and **h**. Scale bar in **j** = 50 μm and applies to **d**, **e**, **i**, and **j**

neurons was observed in layers 2–6, with a high-density parvalbumin-immunopositive terminal network being present in these layers. Palely calbindin-immunopositive neurons were observed primarily in layer 2, with occasional intensely stained neurons being observed in layer 3. Calretinin-immunopositive neurons were observed primarily in layer 3, although occasional neurons were observed in layers 2 and 5. Vesicular glutamate transporter 2-immunoreactive boutons were observed in all layers, with a moderate density being observed in layer 3. NFH-immunopositive structures were observed in all cortical layers, but the highest density of these were observed in layers 1,

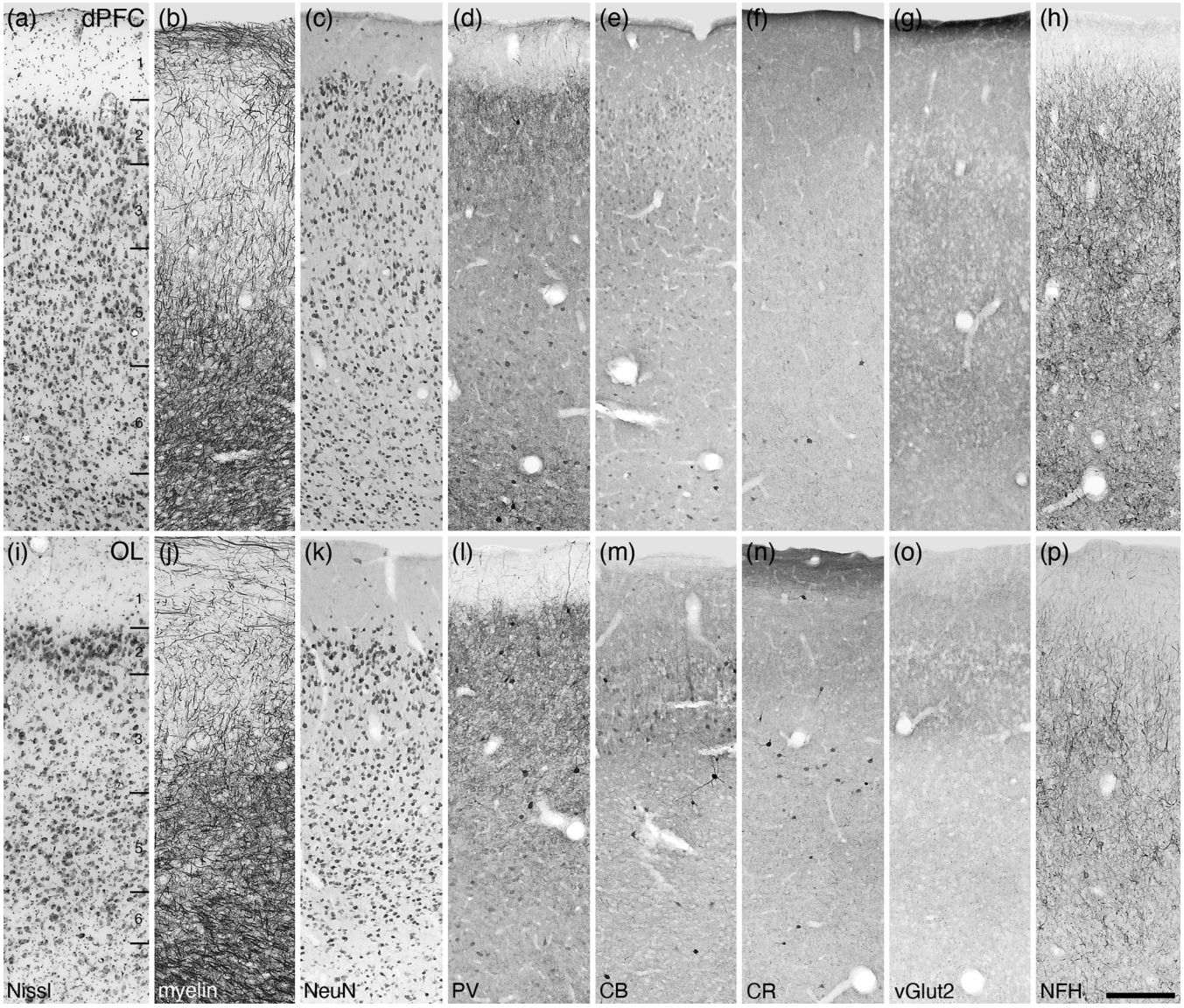

FIGURE 10 Photomicrographs of the dorsal prefrontal cortical area (**dPFC**, **a**-**h**) and the lateral orbital prefrontal cortical area (**OL**, **i**–**p**) within the frontal cortex of the tree pangolin stained for Nissl (**a**, **i**), myelin (**b**, **j**) neuronal nuclear marker (**NeuN**, **c**, **k**), parvalbumin (**PV**, **d**, **l**), calbindin (**CB**, **e**, **m**), calretinin (**CR**, **f**, **n**), vesicular glutamate transporter 2 (**g**, **o**), and neurofilament H (**NFH**, **h**, **p**). Both the **dPFC** and **OL** lack a distinct layer 4, being agranular cortical areas, while the remaining layers **1**–**3, 5,** and **6**, while present (layers labeled in **a** and **i**), do not display precise layer boundaries. In all images, the pial surface is to the top. Scale bar in **p** = 250 μm and applies to all

2, and 5, while occasional immunolabeled soma were observed in layer 3.

3.3.3 | The putative somatosensory cortical region

The region of the tree pangolin cerebral cortex designated as somatosensory was located on the medial wall of the cerebral hemisphere, the lateral gyrus, the sigmoid gyrus, the coronal gyrus, and through the anterior suprasylvian sulcus extending onto the dorsal aspect of the anterior ectosylvian gyrus (Figures 6g–cc and 8a–c). Within the somatosensory cortex, we found evidence for five distinct cortical areas, the rostral somatosensory area (3a or R), the primary somatosensory area (3b or SI), the caudal somatosensory area (SIII), the second somatosensory area (SII), and the parietoventral somatosensory area (PVS) (Figures 6g–cc, 8a–c, 13i–p, 14, and 15). All five cortical areas identified were granular, in that a layer 4 could be identified, although the layer borders were not always distinct (Figures 13i–p, 14, and 15).

The rostral somatosensory area, 3a or R, located caudal to the motor cortex and rostral to the primary somatosensory cortical area (3b), exhibited a moderate neuronal density throughout the cortical layers, although layers 2 and 5 appeared to have a higher density than layers 3, 4, and 6, and the neuron sparse layer 1 (Figure 13i–p). Area 3a was relatively myelin sparse, with moderate fiber densities observed in layers 1, 5, and 6. A low density of parvalbumin-immunopositive

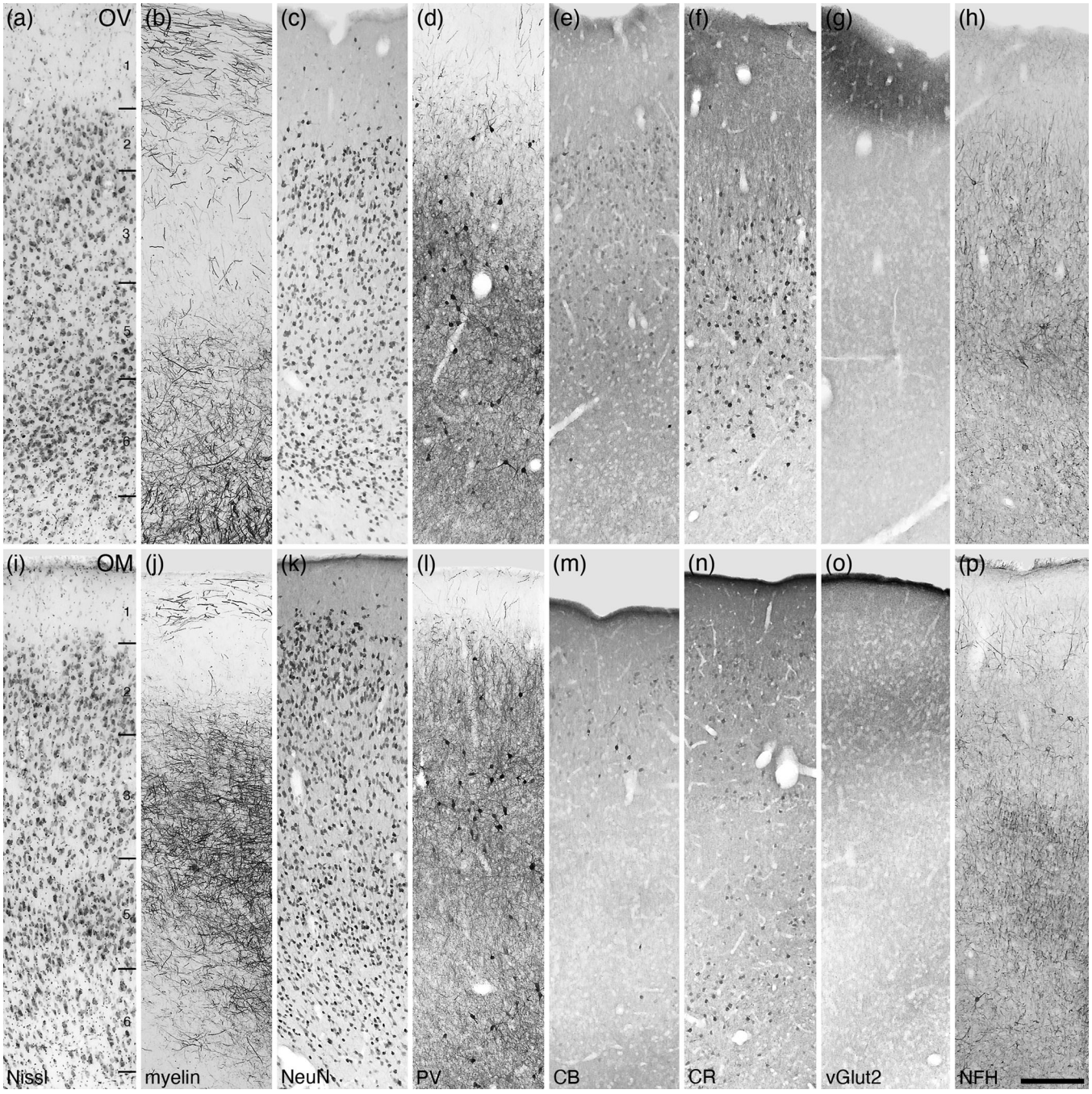

FIGURE 11 Photomicrographs of the ventral orbital prefrontal cortical area (**OV**, **a**-**h**) and the medial prefrontal orbital cortical area (**OM**, **i**-**p**) within the frontal cortex of the tree pangolin. Both the **OV** and **OM** lack a distinct layer 4, being agranular cortical areas, while the remaining layers **1–3, 5,** and **6**, while present (layers labeled in **a** and **i**), do not display precise layer boundaries. All conventions, scale bar, and abbreviations as in Figure 10

neurons was observed in layers 2–6, with a high-density parvalbumin-immunopositive terminal network being preset in these layers. Palely calbindin-immunopositive neurons were observed primarily in layers 2 and 3, while a low density of intensely stained calretinin-immunopositive neurons was observed in layers 2, lower layer 3, and layer 5. Vesicular glutamate transporter 2-immunoreactive boutons were observed in all layers, with a moderate density being observed in lower layer 3 and most prominent in the thin layer 4. NFH-immunopositive structures were observed in all cortical layers, but the highest density of these was observed in layers 3, 4, and 6.

The primary somatosensory area, 3b or SI, located caudal to area 3a, presents with a moderate neuronal density throughout the layers, with layer 2 appearing to have the highest relative density (Figure 14a–h). The density of myelinated fibers was substantially higher in area 3a compared to area 3a, with a substantial number of horizontally oriented fibers being present in lower layer 3 and

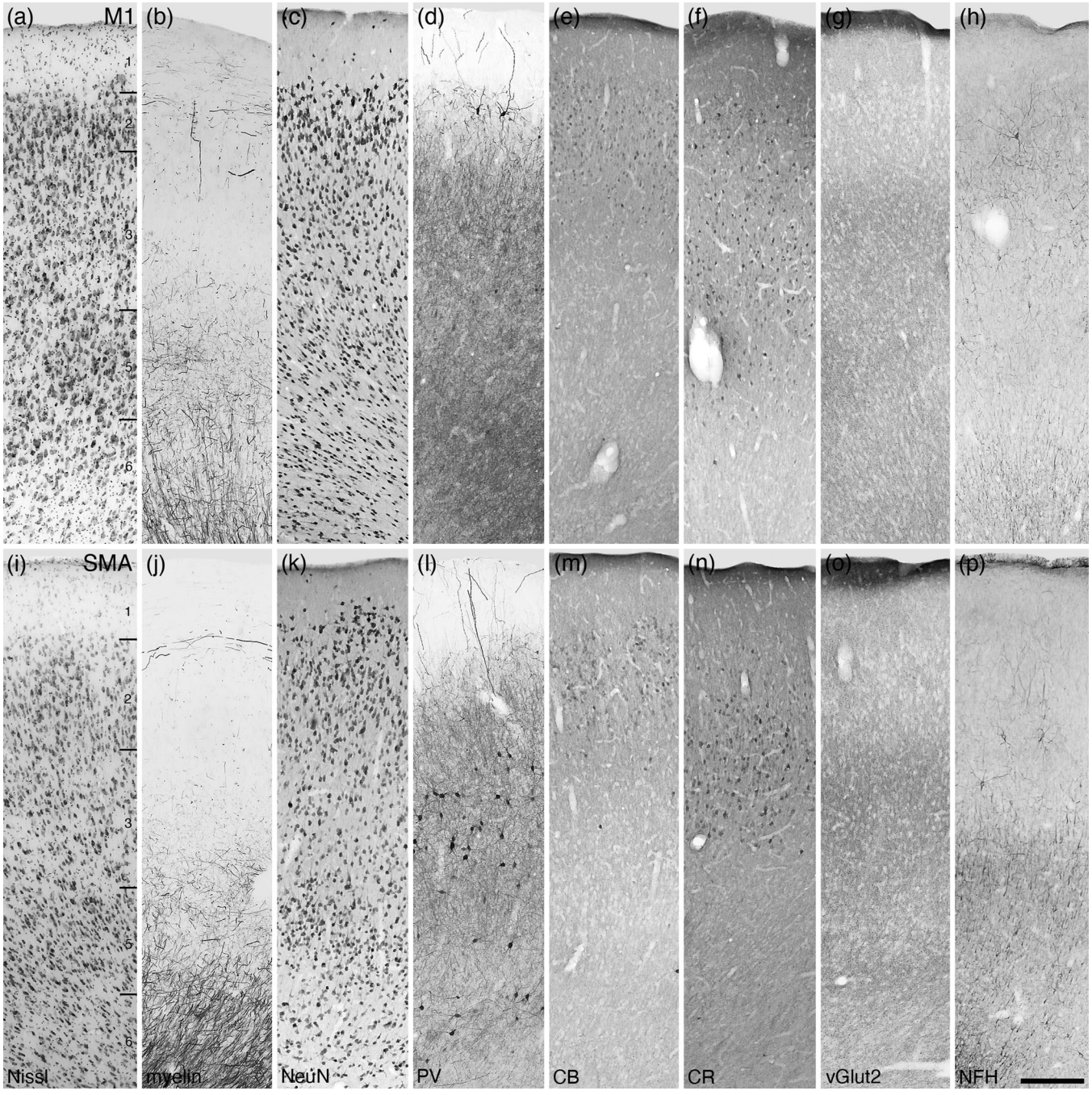

FIGURE 12 Photomicrographs of the primary (**M1**, **a**–**h**) and supplementary (**SMA**, **i**-**p**) motor cortical areas of the tree pangolin. Both the **M1** and **SMA** lack a distinct layer 4, being agranular cortical areas, while the remaining layers **1**–**3, 5,** and **6**, while present (layers labeled in **a** and **i**), do not display precise layer boundaries. All conventions, scale bar, and abbreviations as in Figure 10

layer 4, with distinct radially oriented myelinated fascicles being present in layers 5 and 6. Parvalbumin-immunopositive neurons and terminal networks were observed in all layers, with layers 2, 3, and 5 containing the highest densities of these immunopositive structures. Palely calbindin-immunopositive neurons were observed in layers 2 and 3, with the occasional large multipolar and small bipolar calbindin-immunopositive neuron being observed in layer 5. Calretinin-immunopositive neurons were primarily located in layer 5, with a few neurons being observed in layers 2 and 3. Vesicular glutamate transporter 2-immunoreactive boutons were observed in all layers, with the highest bouton density being observed in layers 2 and 3. Immunostaining for neurofilament H revealed structures throughout all layers, with these being most dense in layers 2 and 3, and the occasional soma being immunolabeled in layer 4.

The third somatosensory cortical area, or SIII, was located caudal to area 3b. The neuronal density in this region was similar to that observed in area 3b, but with less variation in density across the layers (Figure 14i–p). Myelin densities were similar to those

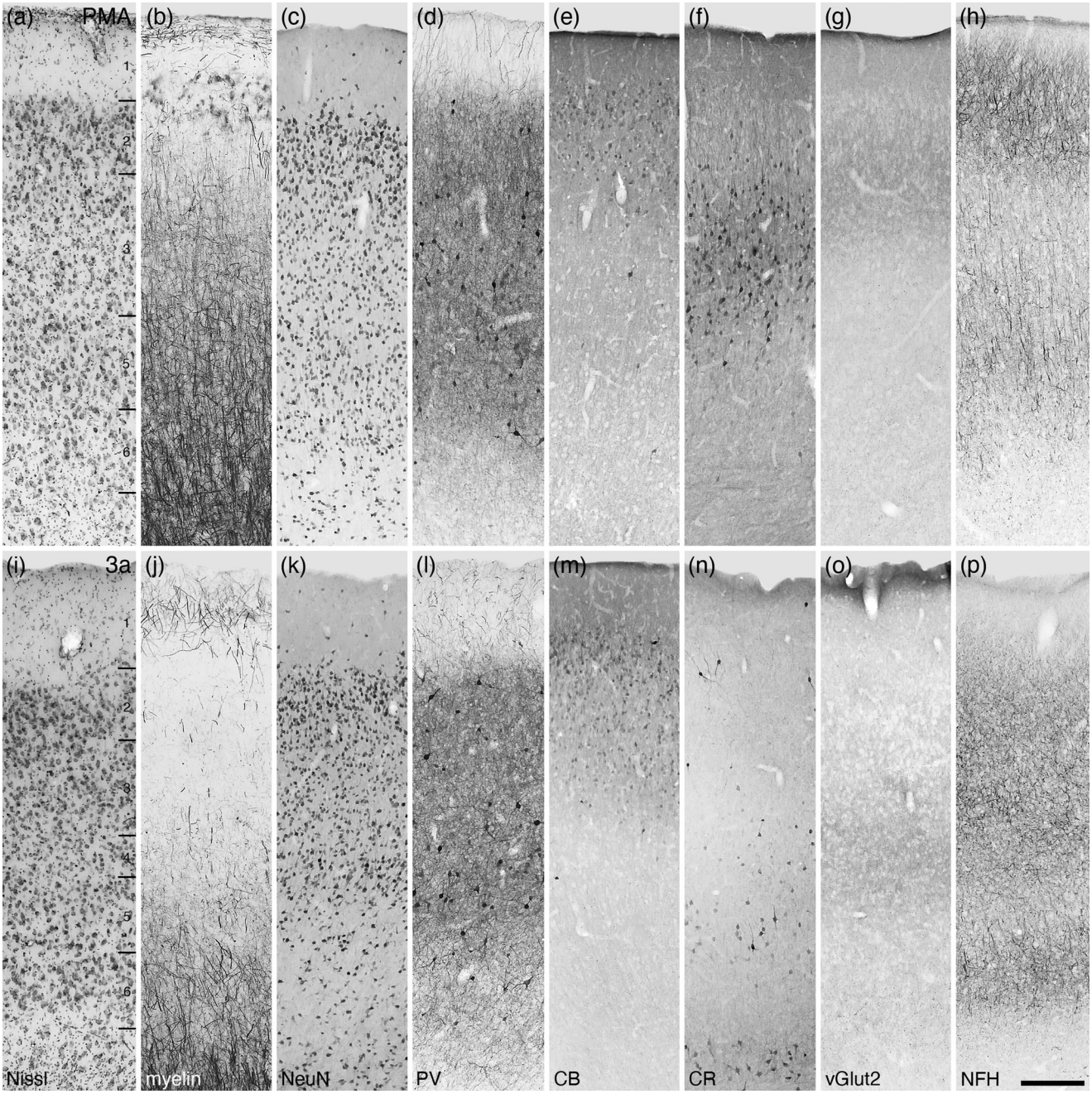

FIGURE 13 Photomicrographs of the premotor cortical area (**PMA**, **a**–**h**) and the rostral somatosensory area (Brodmann area **3a**, **i**-**p**) of the tree pangolin. While the **PMA** lacks a distinct layer 4, the sensory region **3a** exhibits a thin layer 4 with a low neuronal density. In both of these cortical areas, precise layer boundaries are not present. Note that the **CR** (**f**, **n**), **vGlut2** (**g**, **o**), and **NFH** (**h**, **p**) immunostaining is different between the two cortical areas, providing the markers for labeling the transition from motor cortical regions to somatosensory cortical regions. All conventions, scale bar, and abbreviations as in Figure 10

observed in area 3b, but the density of horizontally oriented fibers in layers 3 and 4 appeared lower. Similarly, the density of radially oriented fascicles in layers 5 and 6 was slightly lower than observed in area 3b. Parvalbumin-immunopositive neurons and terminal networks were observed in all layers, with layers 2, 3, and 5 containing the highest densities of these immunopositive neurons and layer 3 having the densest terminal network. Moderately intensely stained calbindin-immunopositive neurons were observed in layers 2 and 3, with the occasional small bipolar calbindin-immunopositive neuron being observed in layer 5. Calretinin-immunopositive neurons were primarily located in layer 5, with a few neurons being observed in layers 3 and 6. Vesicular glutamate transporter 2-immunoreactive boutons were observed in all layers, with the highest bouton density being observed in layers 2 and 3, but it should be noted that this density was substantially less than observed in the adjacent area 3b. Immunostaining for neurofilament H revealed structures throughout all layers, with

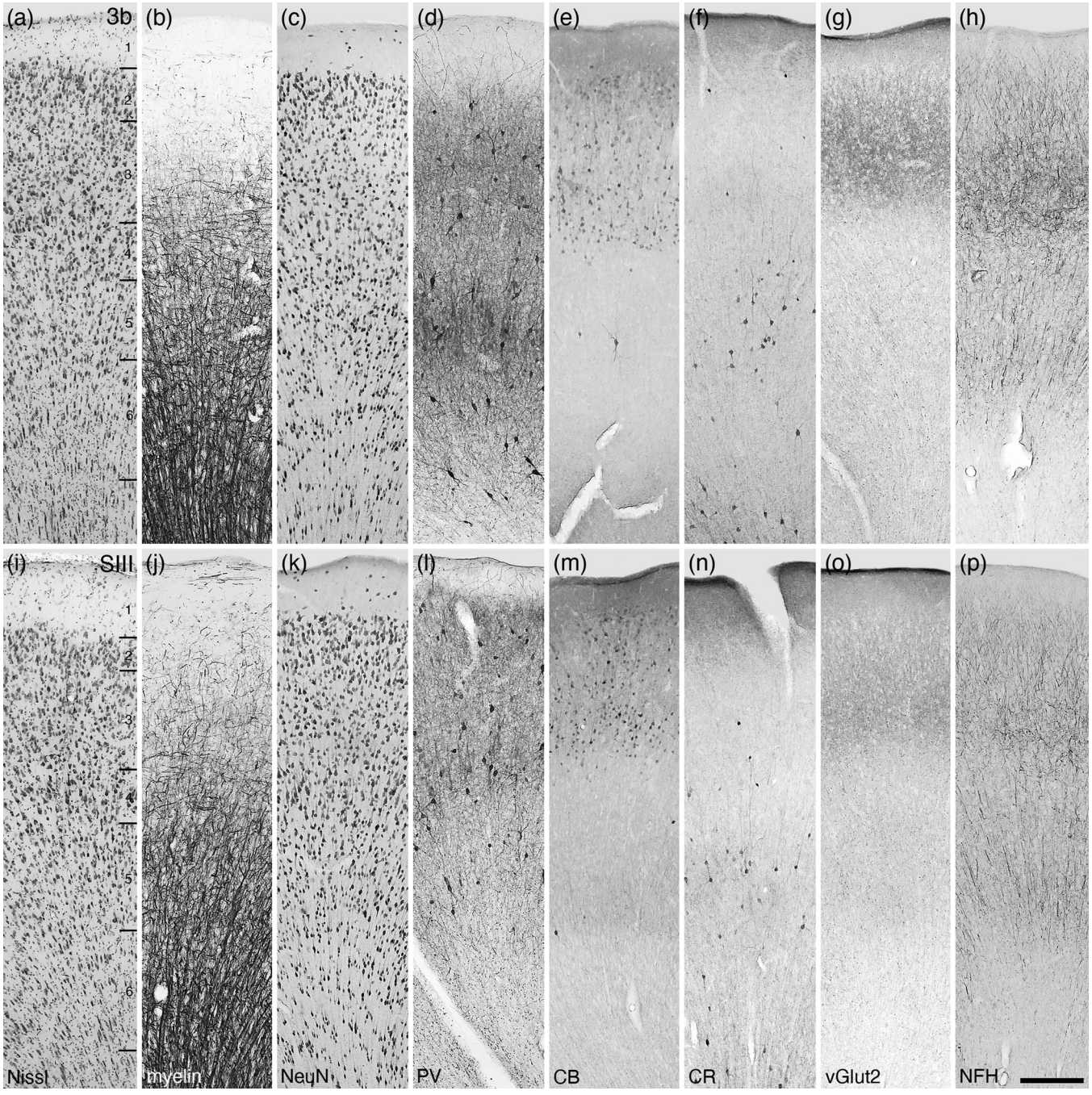

FIGURE 14 Photomicrographs of the primary somatosensory area (Brodmann area **3b** or **SI**, **a**–**h**) and the third somatosensory area (**SIII**, **i**–**p**) of the tree pangolin. In these two cortical areas, a distinct layer 4 is present, although the neurons within this layer are primarily pyramidal. All conventions, scale bar, and abbreviations as in Figure 10

these being most dense in layers 2 and 3, although substantially less dense than observed in area 3b.

In the lateral aspect of the somatosensory cortical region, two areas, the parietoventral (PVS), rostrally, and second (SII), caudally, somatosensory areas were identified on the banks of the rostral portion of the suprasylvian sulcus and the rostral surface of the anterior ectosylvian gyrus (Figure 8a, b). The neuronal density within PVS appears to be lower than surrounding cortical areas, with layer 5 exhibiting the highest relative density, with the lowest density being in layer 4 (apart from the neuron sparse layer 1) (Figure 15a–h). PVS also exhibited a low density of myelinated fibers, with only scattered fibers observed in layers 1–4, with loosely arranged radially oriented fibers found in layers 5 and 6. Parvalbumin-immunopositive neurons and terminal networks were observed in layers 3–6, with layers 4 and 5 containing the highest densities of these immunopositive structures. Moderately intensely stained calbindin-immunopositive neurons were observed in layers 2 and 3, with the occasional bipolar calbindin-immunopositive neuron being observed in layers 4 and 5.

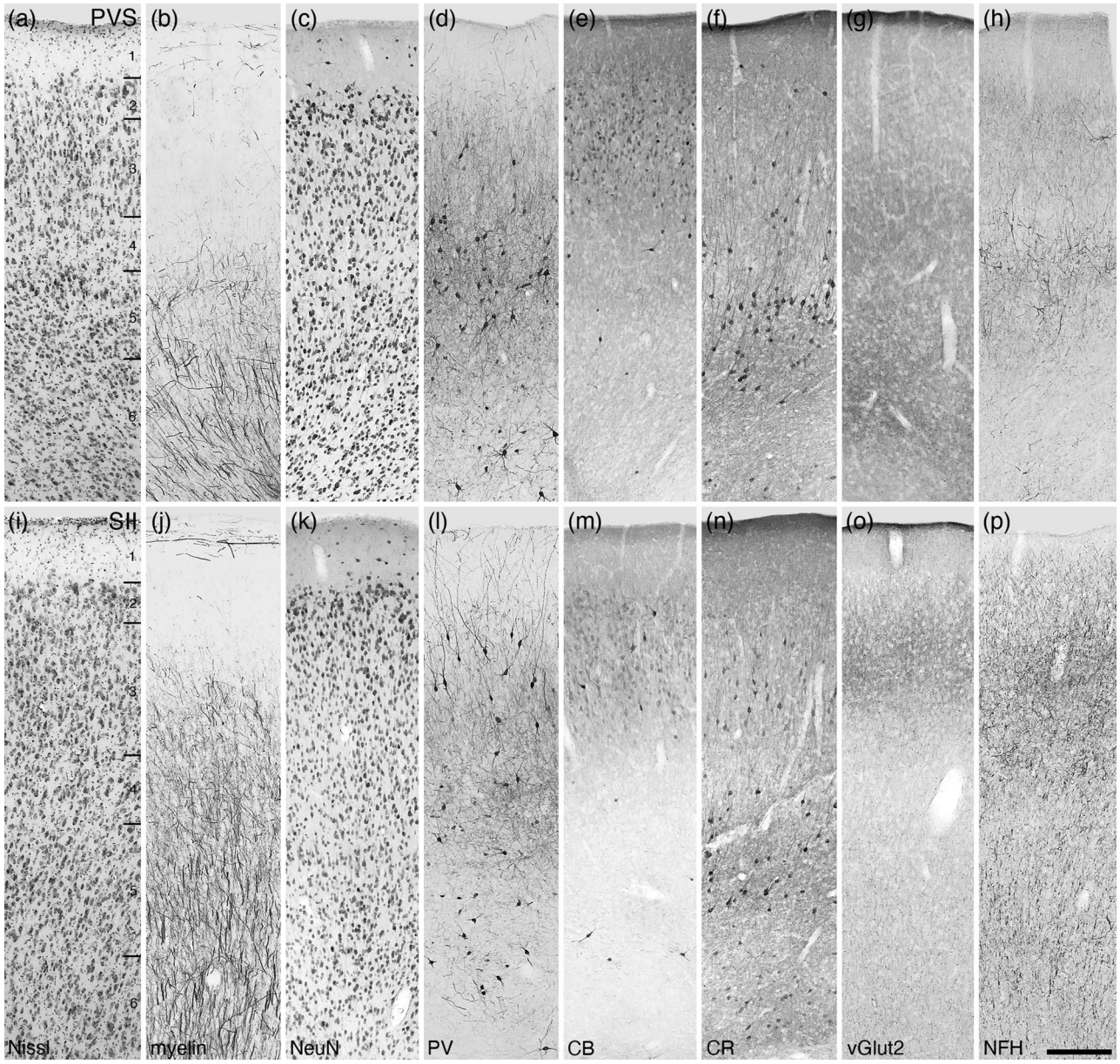

FIGURE 15 Photomicrographs of the parietoventral somatosensory area (**PVS**, **a-h**) and the second somatosensory area (**SII**, **i–p**) of the tree pangolin. Note the low density of neurons in layer 4, and how in both, the upper border of layer 5 is demarcated by the presence of **CR**-immunopositive neurons. All conventions, scale bar, and abbreviations as in Figure 10

Calretinin-immunopositive neurons were primarily located in layer 5, with scattered neurons being observed in the remaining layers. Vesicular glutamate transporter 2-immunoreactive boutons were observed in all layers, with the relatively highest bouton densities being observed in layers 3 and 6. A low density of neurofilament H-immunopositive structures was observed in all layers of PVS, with the relatively highest densities observed in layer 2 and particularly layer 5.

The second somatosensory area, SII, exhibited a consistent moderate neuronal density throughout all layers, although layer 4 appears to have a slightly lower density than the other layers (Figure 15i–p). The density of myelinated fibers is higher in SII than observed in PVS, with radially oriented fibers extending through layers 3–6, with small, but distinct radially oriented fascicles being observed in layers 5 and 6. Parvalbumin immunostaining revealed neurons in layers 2–4, with those in layer 2 exhibiting dendrites extending into layer 1, those in layers 3–6 being slightly smaller in size compared to the layer 2 neurons, with dendrites appearing to remain within their designated layer. The density of parvalbumin-immunopositive terminal networks was highest in layers 3 and 4. Several palely calbindin-immunoreactive neurons were observed in layers 2 and 3, with scattered intensely calbindin-immunoreactive neurons being observed in layers 2, 3, 5, and 6. Calretinin-immunopositive neurons were primarily located in layers 3 and 5, with scattered neurons being observed in layer 6. Vesicular glutamate transporter 2-immunoreactive boutons were observed in all layers, with the highest bouton density being observed in layer 3. Immunostaining for neurofilament H revealed structures throughout

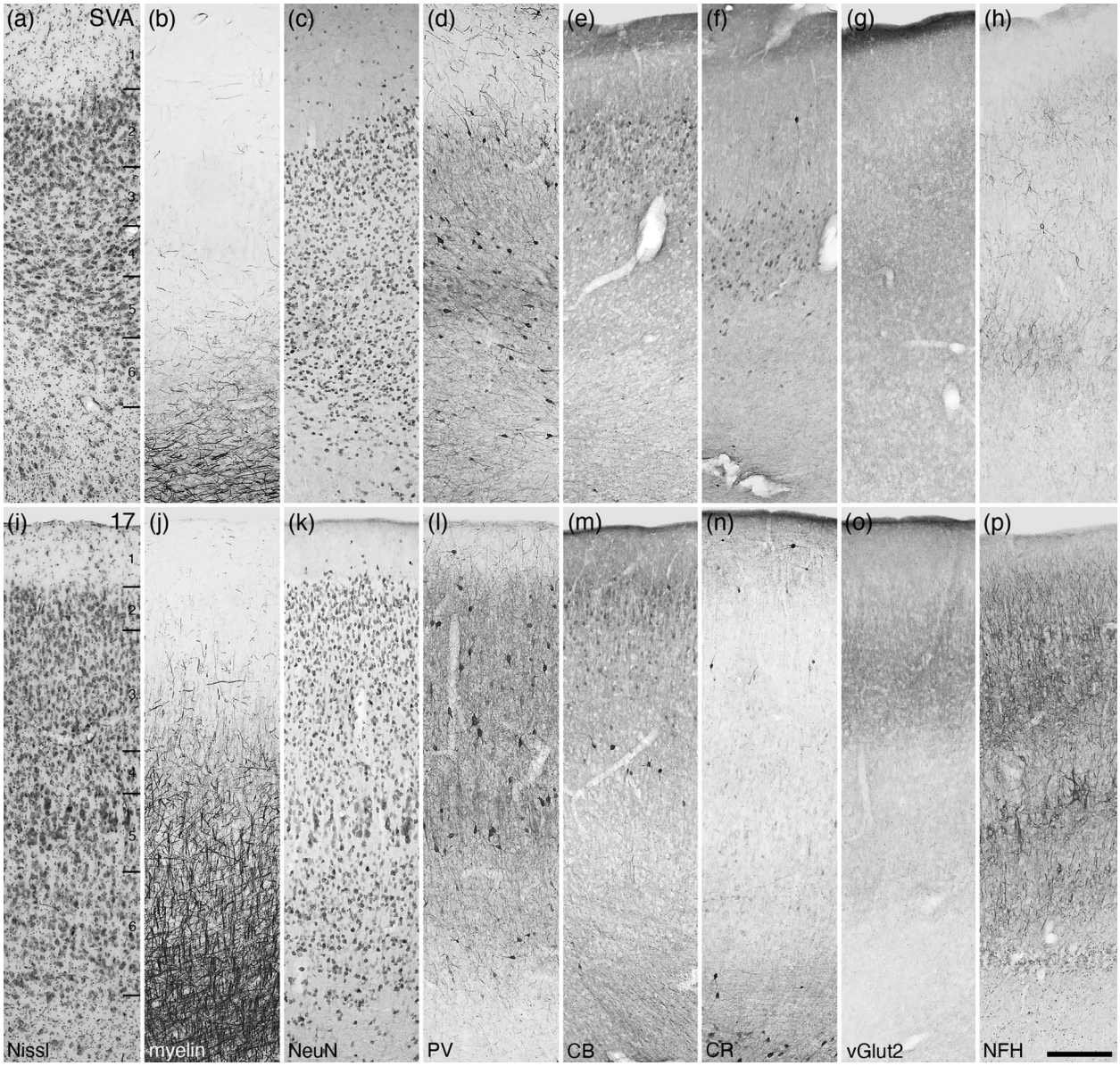

FIGURE 16 Photomicrographs of the splenial visual area (**SVA**, **a**–**h**) and the primary visual area (Brodmann area **17**, **i**–**p**) of the tree pangolin. While the laminar boundaries are somewhat indistinct in the **SVA**, these are clearer in area **17**, although layer 4 is relatively cell sparse and composed of pyramidal cells. All conventions, scale bar, and abbreviations as in Figure 10

all layers, with these being most dense in layers 2 and 3, although substantially densities of structures were observed in the remaining layers.

3.3.4 | The putative visual cortical region

The region of the tree pangolin cerebral cortex designated as visual occupied the external and medial aspects of the caudal portion of the cerebral hemisphere, within which we could identify 10 distinct cortical areas/territories (Figures 6z–qq and 8). These include what may be termed the occipital visual areas (the splenial visual area [SVA], and areas 17, 18, 19, and 21), a posterior parietal region (PP), a laterally located temporal region (area 20), and the suprasylvian visual region (with medial, lateral, and ventral divisions). This visual cortical region occupied the cortex forming the caudal half of the lateral and suprasylvian gyri, as well as the medial and lateral banks of the caudal aspects of the lateral and suprasylvian sulci, and the caudal portion of the medial wall of the hemisphere (Figure 8).

The putative occipital visual cortical areas

The SVA was observed to be a small cortical area, located between the primary visual cortex (area 17) and the hippocampal formation (Figure 6ii–oo). While six layers are evident in this area, the laminar boundaries are relatively indistinct (Figure 16a–h). While layer 1 is neuron sparse, a moderate density of neurons is observed throughout layers 2–6, with layer 2 having a slightly higher neuronal density than the other layers.

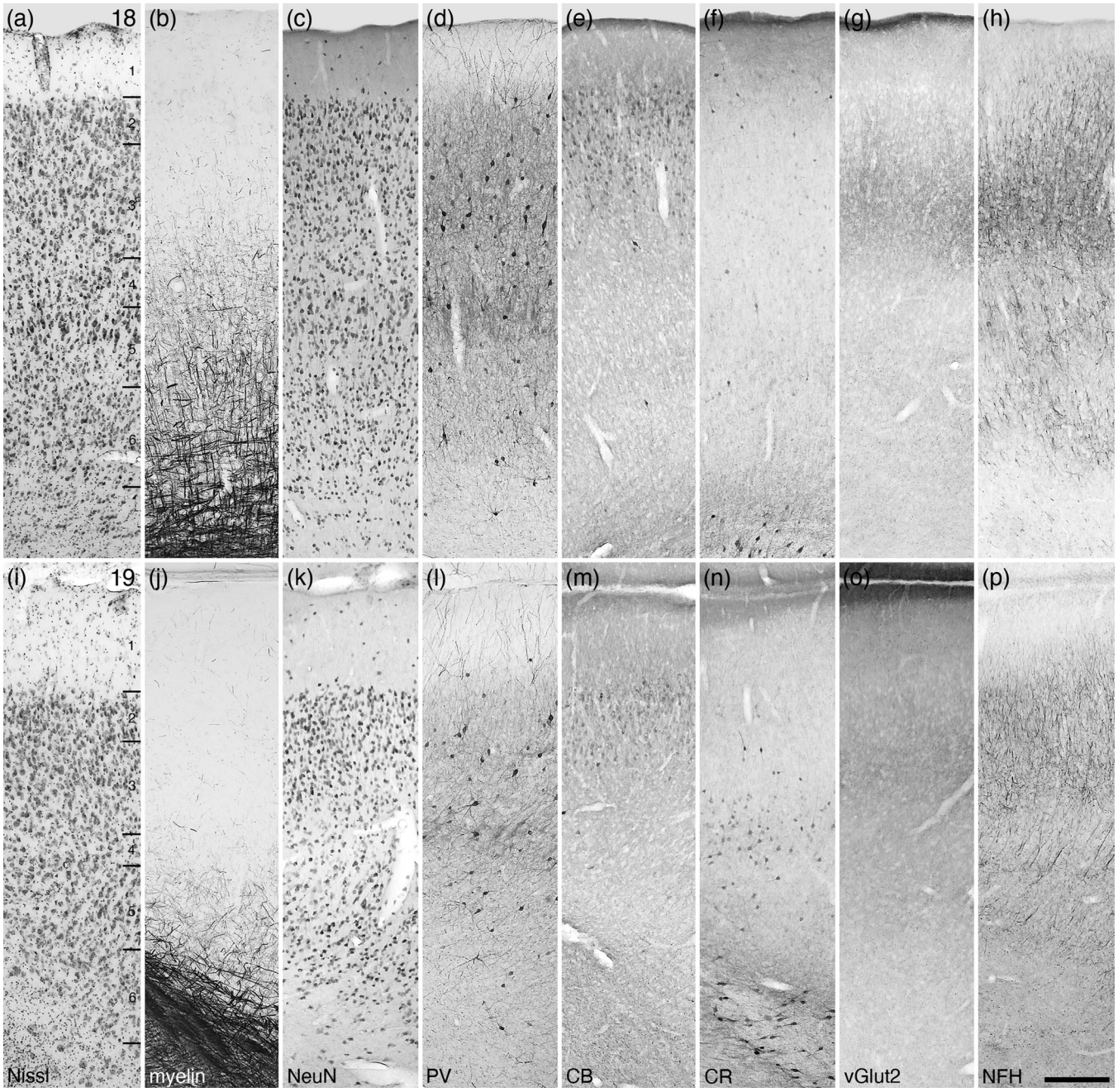

FIGURE 17 Photomicrographs of the second visual area (Brodmann area **18**, **a**-**h**) and the third visual area (Brodmann area **19**, **i**–**p**) of the tree pangolin. The laminar boundaries are less clear than in area 17 (see Figure 16i–p), with layer 4 becoming less distinct with distance from area 17. All conventions, scale bar, and abbreviations as in Figure 10

The SVA is very myelin-sparse, with a low density of myelinated fibers being observed in layers 5 and 6. Parvalbumin-immunopositive neurons and other neuronal structures are observed throughout all layers of the SVA, with layers 2, 3, and 5 housing the majority of neurons, with the highest density of other structures being observed in layer 4. Palely calbindin-immunoreactive neurons were observed primarily in layers 2 and 3, with scattered intensely calbindin-immunoreactive neurons being observed in layers 2 and 3. Calretinin-immunopositive neurons were primarily observed in the internal half of layer 3 and throughout layer 4, with occasional neurons being observed in layers 2, 5, and 6. A relatively low density of vesicular glutamate transporter 2-immunoreactive boutons was observed in all layers, with the highest bouton density being observed in layers 3 and 4. Immunostaining for neurofilament H revealed structures throughout all layers, with these being most dense in layers 2 and 6, with occasional neurofilament H-immunopositive neurons being noted in layers 3 and 4.

The primary visual area, or Brodmann area 17, occupied the caudal aspect of the lateral gyrus, as well as the caudal aspect of the medial wall of the cerebral hemisphere (Figures 6ff–qq and 8). Of all the cortical areas observed in the tree pangolin, area 17 presented

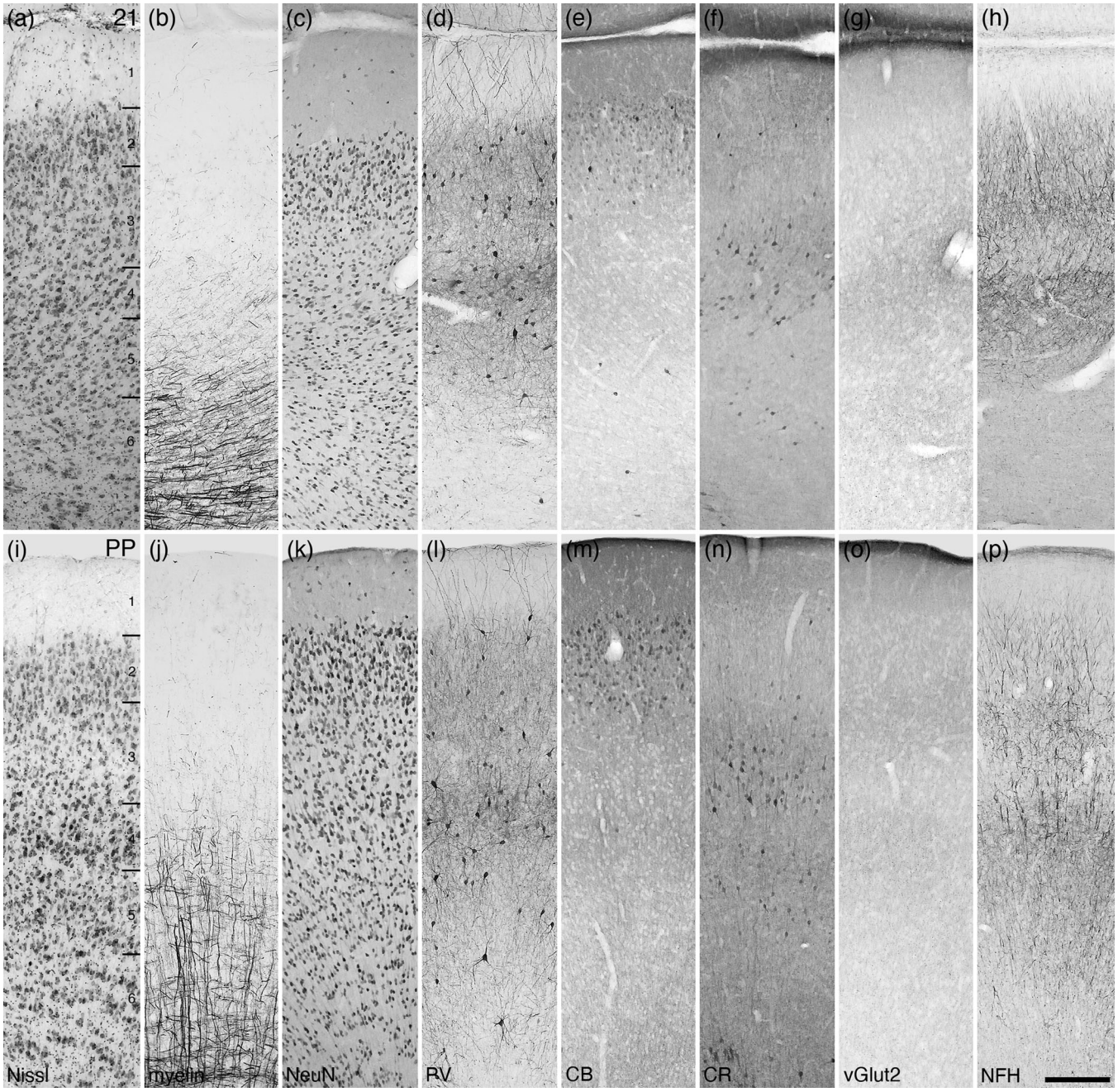

FIGURE 18 Photomicrographs of the fourth visual area (Brodmann area **21**, **a**–**h**) and the posterior parietal cortical region (**PP**, **i**-**p**) of the tree pangolin. While the laminar boundaries are not as distinct as in other visual cortical areas, the range of stains used guide the delineation of the boundaries. All conventions, scale bar, and abbreviations as in Figure 10

with the most distinct layers, with six layers being readily apparent (Figure 16i–p). In a relative sense, the overall neuronal density within area 17 appears to be slightly higher than adjacent cortical area, with layer 2 exhibiting the highest neuronal density. Layer 4 was relatively neuron sparse, while in the outer half of layer 5, large neurons were observed with the inner half being relatively neuron sparse. Myelinated axons were observed in layers 3-6, with an increase in density with depth and the presence of distinct radial fascicles and horizontally oriented fibers being observed in layers 5 and 6. Parvalbumin-immunopositive neurons were observed in all cortical layers, except layer 4, with layers 2, 3, and 5 containing the majority of these neurons. Parvalbumin-immunopositive structures were observed in all layers, with layer 5 exhibiting the highest density. Palely stained calbindin-immunopositive neurons were observed in layers 2 and 3, while in layer 4, a low density of intensely stained neurons was observed. Very few calretinin-immunopositive neurons were observed in layers 1, 3, and 6. Vesicular glutamate transporter 2-immunoreactive boutons were observed in all layers, with the highest bouton density being observed in layers 3 and 4. Neurofilament H-immunoreactive structures were observed in all layers, with the highest density being observed in

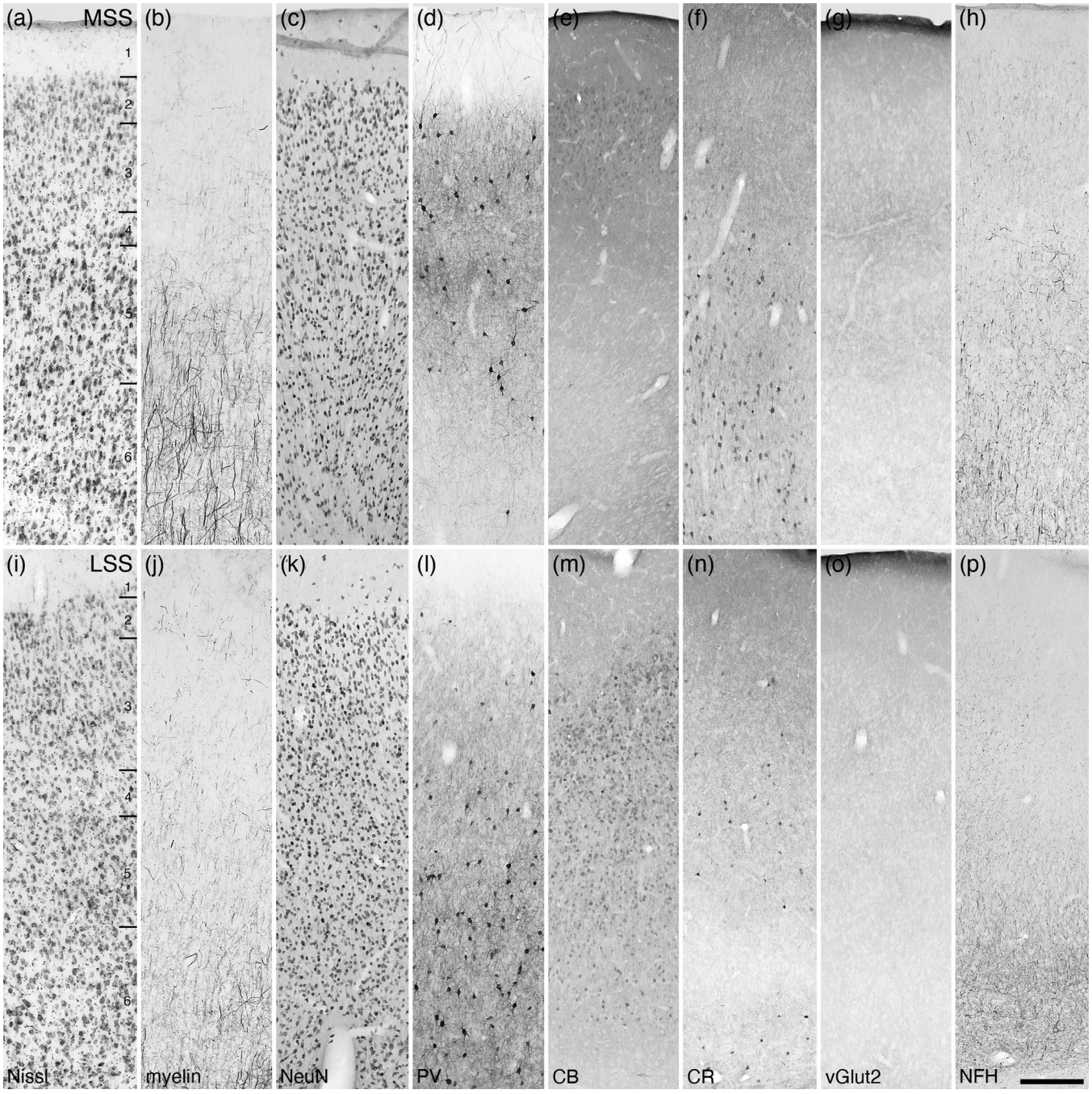

FIGURE 19 Photomicrographs of the medial (**MSS**, **a-h**) and lateral (**LSS**, **i–p**) suprasylvian cortical regions of the tree pangolin. The varied staining patterns of neurons immunopositive for **PV**, **CB,** and **CR** guide the division of this cortical region into the various areas. All conventions, scale bar, and abbreviations as in Figure 10

layers 2, 3, 5, and 6, with the larger neurons of layer 5 showing intense immunoreactivity.

The second visual area, or Brodmann area 18, was localized to the caudal aspect of the lateral gyrus and the caudal aspect of the medial wall of the cerebral hemisphere (Figures 6cc–pp and 8). Area 18 presented with six layers, although the layer boundaries were not as distinct as observed in area 17 (Figure 17a–h). The highest relative neuronal density was observed in layer 2, with distinctly larger neuronal soma being observed in layer 5 and distinctly smaller neuronal soma being observed in layer 6. Layer 4 and the inner half of layer 5 exhibited the lowest relatively neuronal densities (apart from the neuron sparse layer 1). Layers 1–3 were myelin sparse, with densities of myelin increasing with depth in the cortex and distinct radial fascicles and horizontally oriented fibers being most evident in layer 6. Parvalbumin-immunopositive neurons were observed in layers 2–6, with layer 3 presenting with the highest relative density of these neurons. Parvalbumin-immunopositive dendrites were observed in all layers, layer 3 being particularly dense in these structures,

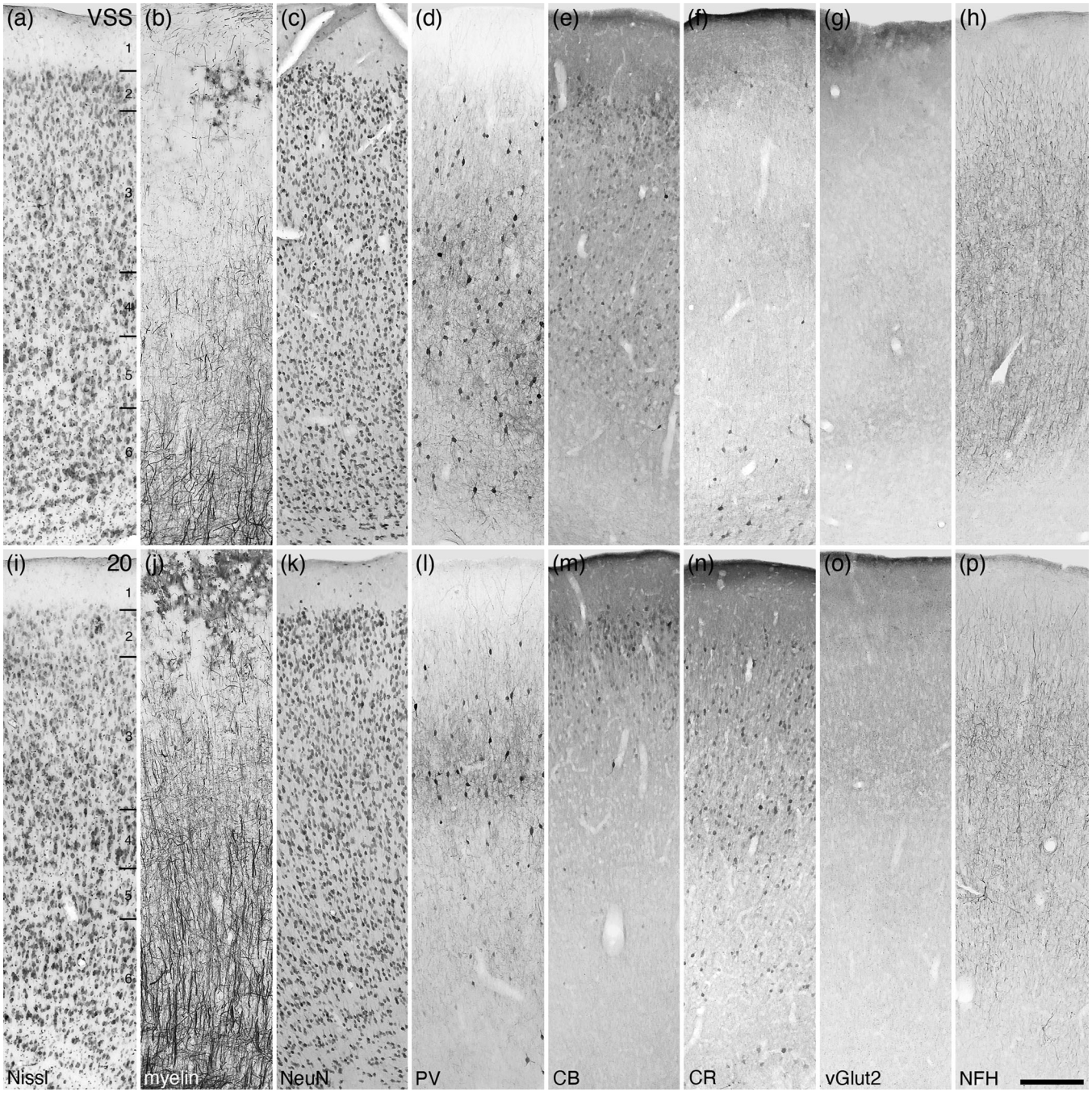

FIGURE 20 Photomicrographs of the ventral suprasylvian cortical region (**VSS**, **a**–**h**) and the temporal cortical region (Brodmann area **20**, **i**-**p**) of the tree pangolin. The staining patterns of neurons immunopositive for **PV**, **CB,** and **CR** guide the demarcation of these cortical areas. All conventions, scale bar, and abbreviations as in Figure 10

with layer 5 exhibiting an intense parvalbumin-immunopositive neuropil staining. Palely stained calbindin-immunopositive neurons were observed in layers 2 and upper layer 3, with the occasional intensely stained neuron being observed in lower layer 3 and layer 6. A few calretinin-immunopositive neurons were observed in layers 2 and 5, with a distinct relatively high density of vesicular glutamate transporter 2-immunoreactive boutons being observed in layers 3 and 4. Neurofilament H-immunopositive structures were observed in all layers, these being most dense in layer 3, while the larger neurons in layer 5 were also labeled.

The third visual area, or Brodmann area 19, was localized to the caudal aspect of the lateral gyrus and the caudal bank of the lateral sulcus (Figures 6dd–nn and 8a,b). While the six cortical layers were evident, the distinction of the layer boundaries was less precise than in areas 17 and 18 (Figure 17i–p). Relative neuronal density was the highest in layers 2 and 3, with the thin layer 4 being relatively neuron sparse. Area 19

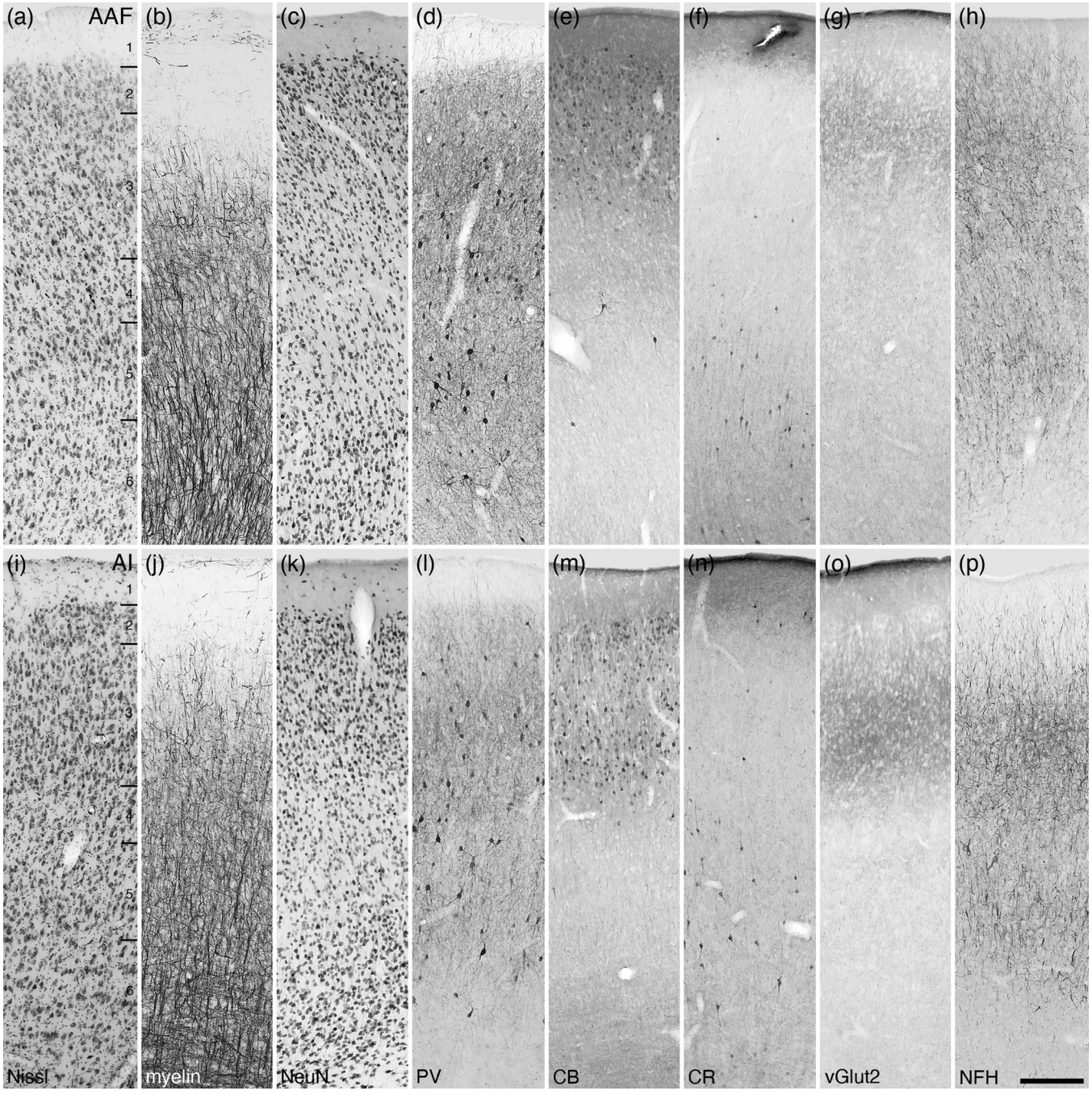

FIGURE 21 Photomicrographs of the anterior auditory field (**AAF**, **a**–**h**) and the primary auditory cortical area (**AI**, **i**–**p**) of the tree pangolin. The laminar variances in myelin, **CB,** and **vGlut2** staining guide the demarcation of these areas. All conventions, scale bar, and abbreviations as in Figure 10

exhibited a low density of myelin, although a moderate to low density of myelinated fibers was observed in layers 5 and 6, although distinct radial fascicles and horizontally oriented fibers were not obvious. Parvalbumin-immunopositive neurons were observed in all layers, the majority of which were in layer 3, while parvalbumin-immunopositive dendrites were observed in all layers, with layer 3 having the highest relative density. Palely stained calbindin-immunopositive neurons were observed in layer 2, with the occasional intensely stained neuron being observed in layer 2 and lower layer 3. Palely stained calretinin-immunopositive neurons were observed primarily in layer 5, with a few neurons being noted in layers 3 and 6. Vesicular glutamate transporter 2-immunoreactive boutons were observed in all layers, with the highest relative bouton density being observed in layers 3 and 4. Neurofilament H-immunopositive structures were observed in all layers, these being most dense in layer 3.

The fourth visual area, or Brodmann area 21, was localized to the caudal aspect of the suprasylvian gyrus and the rostral bank of the lateral sulcus (Figures 6gg–mm and 8a,b). Neurons were observed in

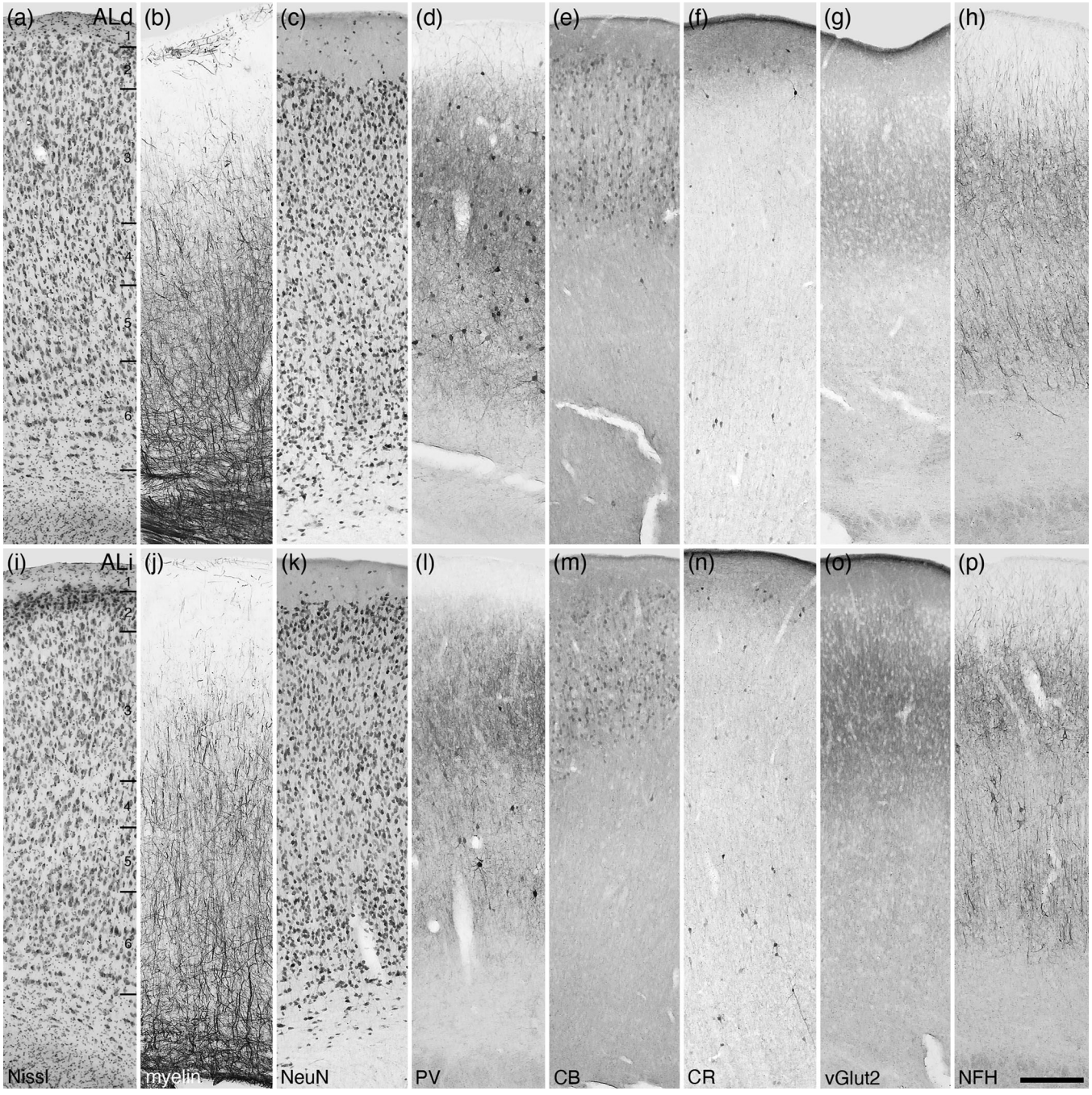

FIGURE 22 Photomicrographs of the dorsal (**ALd**, **a**–**h**) and intermediate (**ALi**, **i-p**) areas of the lateral auditory cortex of the tree pangolin. The laminar variances in myelin, **PV**, **vGlut2,** and **NFH** staining guide the demarcation of these areas. All conventions, scale bar, and abbreviations as in Figure 10

all six cortical layers, although very few are present in layer 1 and the relatively highest density of neurons was observed in layer 2 (Figure 18a–h). As with area 19, this cortical area exhibited a low density of myelinated fibers, the majority of which were observed in layers 5 and 6. Parvalbumin-immunoreactive neurons were observed in layers 2–6, the majority of which were found in layers 3 and 5. Parvalbumin-immunopositive dendrites were observed in all layers, with layers 2, 3, and 5 having the highest relative density, while layers 1, 4, and 6 exhibiting lower relative densities. Palely stained calbindin-immunopositive neurons were observed primarily in layer 2 and the very upper portion of layer 3, with the occasional intensely stained neuron being observed in layers 2, 5, and 6. Calretinin-immunopositive neurons were observed primarily in layers 3, 4, and 5, with a few neurons being noted in the upper portions of layer 2 and at the border of layer 6 and white matter. Vesicular glutamate transporter 2-immunoreactive boutons were observed in all layers, with the highest relative bouton density being

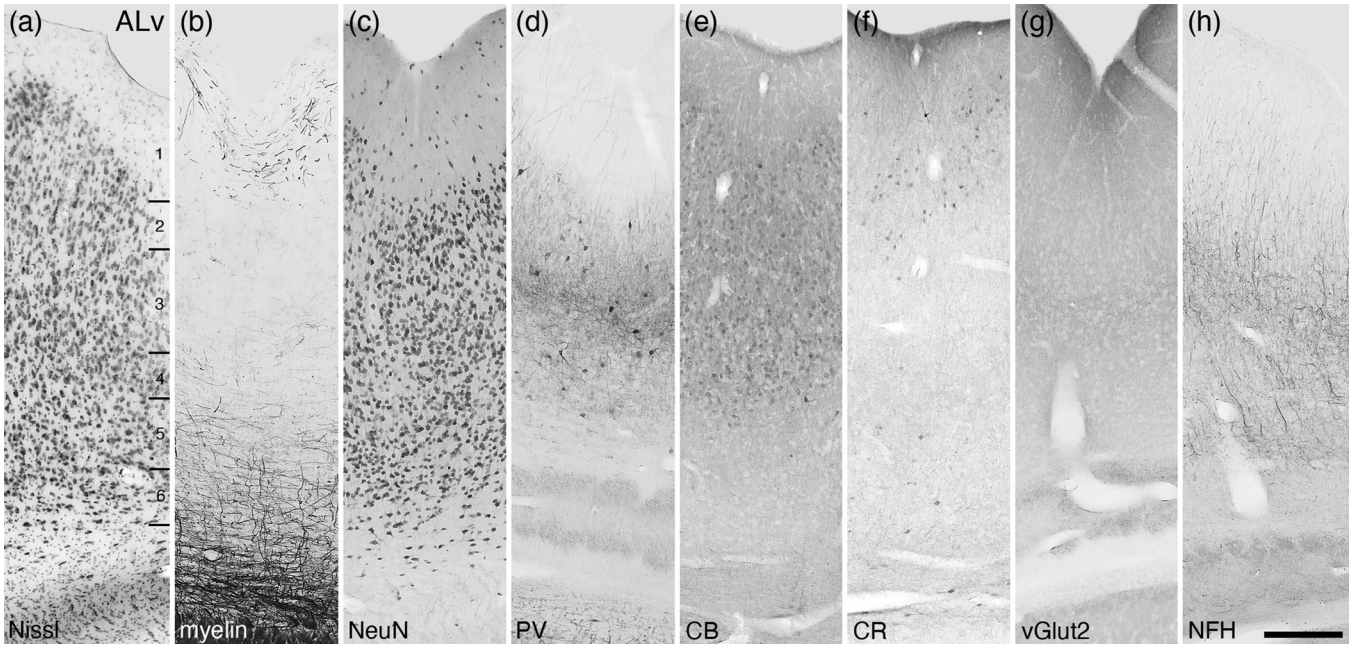

FIGURE 23 Photomicrographs of the ventral area of the lateral auditory cortex (**ALv**) of the tree pangolin. Note the restricted distribution and presence of structures stained for **PV**, **vGlut2,** and **NFH** in comparison to the adjacent auditory areas (see Figure 22). All conventions, scale bar, and abbreviations as in Figure 10

observed in layer 4. Neurofilament H-immunopositive structures were observed in all layers, these being most dense in layers 3 and 5, and less dense in layers 1, 2, 4, and 6.

The putative posterior parietal cortical region

In carnivores and other mammalian species, the posterior parietal cortex is often parcellated into two cortical areas (Pigarev, & Rodionova, 1998; Manger et al., 2002b), but in the tree pangolin, with the range of stains employed, we could only accurately delineate the posterior parietal region and not identify distinct areas within this region. The posterior parietal region of the tree pangolin cerebral cortex was located on the lateral and suprasylvian gyri, as well as in the medial and lateral banks of the lateral sulcus (Figures 6aa–kk and 8a,b). This cortical region exhibited six cortical layers, although the laminar boundaries were not especially sharp (Figure 18i–p). Relative neuronal densities were highest in layers 2 and 4, while the upper cortical layers 1, 2, and 3 were relatively myelin sparse. In layers 4, 5, and 6, a moderate density of myelinated fibers were observed, these fibers being observed as thin radial fascicles and horizontally oriented fibers. Parvalbumin-immunopositive neurons were localized to layers 2–6 with the highest relative density being observed in layer 4. Parvalbumin-immunopositive dendrites were observed in all layers, the highest density of these being in layer 4. Calbindin-immunopositive neurons were found primarily in layer 2, while calretinin-immunopositive neurons were primarily located in layer 3 although some are observed in layer 5. Vesicular glutamate transporter 2-immunoreactive boutons were observed in all layers, with slightly higher relative bouton density being observed in layers 3 and 5. Neurofilament H-immunopositive structures were observed in all layers, these being most dense in layers 5 and 3, and less dense in other layers.

The putative suprasylvian visual cortical region

In carnivores, up to six cortical areas have been identified within the medial and lateral banks of the suprasylvian sulcus (Homman-Ludiye et al., 2010; Palmer et al., 1978), but in the current study of the tree pangolin, with the range of stains employed, only three areas could be identified; however, there is an organizational resemblance of this cortical region to that observed in carnivores. The three areas identified in the suprasylvian region of the tree pangolin cortex we term the medial (MSS), lateral (LSS), and ventral (VSS) suprasylvian areas, based on their locations occupying the medial bank, lateral bank, and caudoventral portion of suprasylvian sulcus, respectively (Figures 6z–kk and 8a,b).

Within the MSS, six cortical layers could be distinguished, although the laminar boundaries are not precise, and the supragranular layers appear to be thinner in relation to surrounding cortical regions (Figure 19a–h). The relatively highest neuronal density was observed in layer 2, while layer 4 exhibited the relatively lowest neuronal density (apart from the neuron sparse layer 1). Myelinated axons were observed in all layers, although the density of these was highest in layers 5 and 6 where radially oriented fibers, which did not form distinct fascicles, were evident. Parvalbumin-immunopositive neurons were observed primarily in layers 2, 3, and 5, with only occasional neurons observed in layers 4 and 6. The relative density of parvalbumin-immunopositive dendrites followed this laminar pattern. Very palely stained calbindin-immunopositive neurons were observed in layers 2 and 3, while moderately intensely calretinin-immunopositive neurons were observed in layers 4, 5, and 6. Vesicular glutamate transporter

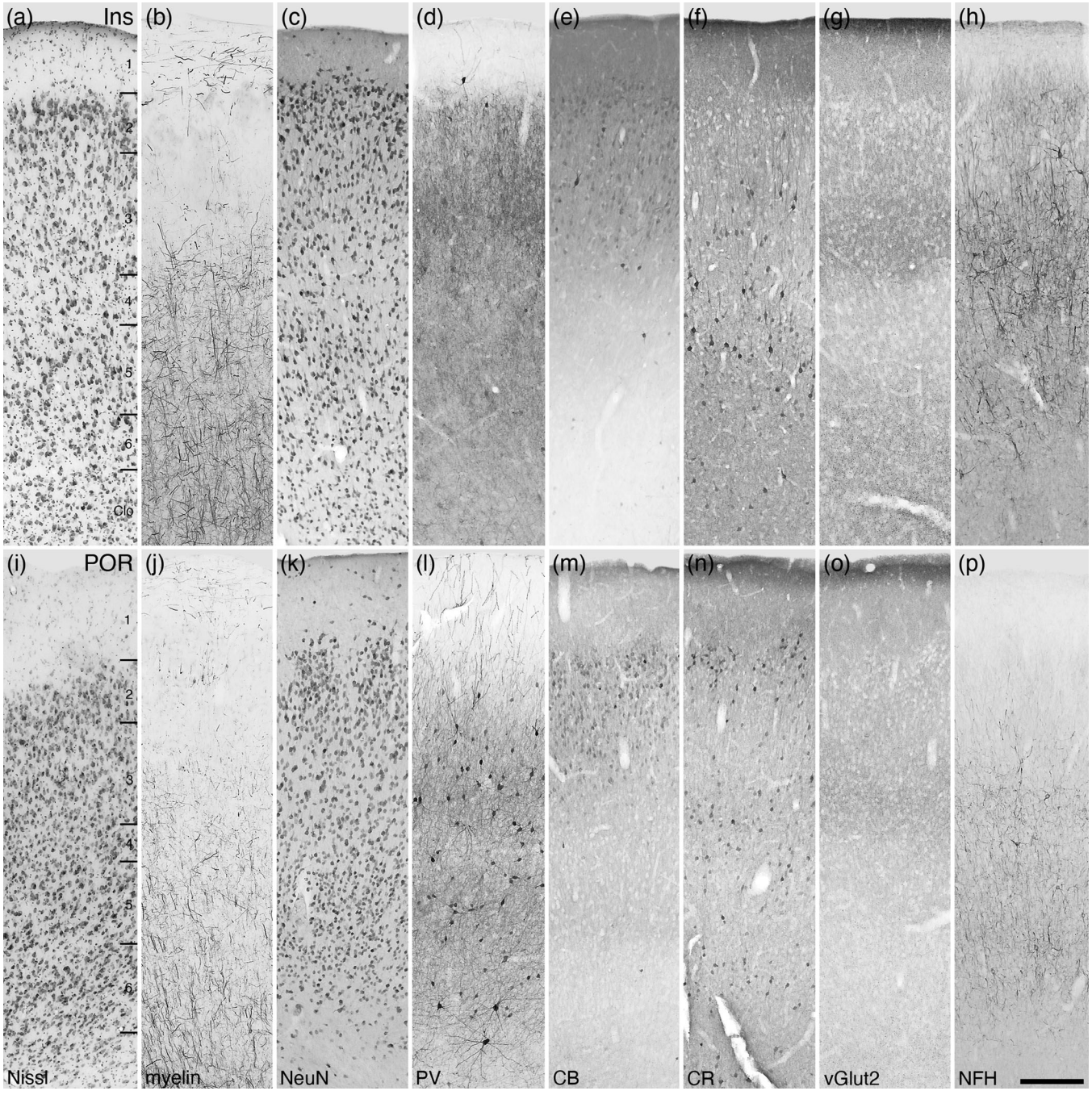

FIGURE 24 Photomicrographs of the insular (**Ins**, **a-h**) and postrhinal (**POR**, **i-p**) areas of the tree pangolin. The laminar variances in myelin, **PV**, **CR,** and **NFH** staining guides the demarcation of these areas. All conventions, scale bar, and abbreviations as in Figure 10

2-immunoreactive boutons were observed in all layers, with slightly higher relative bouton density being observed in layers 4 and 5. Neurofilament H-immunopositive structures were observed in all layers, these being most dense in layers 5 and 6.

Within the LSS, six cortical layers were observed, although the laminar boundaries are less distinct than observed in the MSS (Figure 19i–p). The relative neuronal density throughout these layers did not appear to alter substantially between layers. While myelinated fibers were found in all layers of the LSS, their density was quite low, with layer 6 showing the highest relative density. Parvalbumin-immunopositive neurons were observed in layers 2–6, although the relative density of these neurons was low in layers 2, 3, and 4, with these neurons being primarily located in layers 5 and 6. The density of parvalbumin-immunopositive dendrites followed a similar laminar pattern. Palely stained calbindin-immunopositive neurons were observed in layers 2–6 with no apparent differences in density between layers. Scattered calretinin-immunopositive neurons were observed primarily in layer 5 of the LSS. Vesicular glutamate transporter 2-immunoreactive boutons were observed in all layers, with a very slightly higher relative bouton density being observed in layer

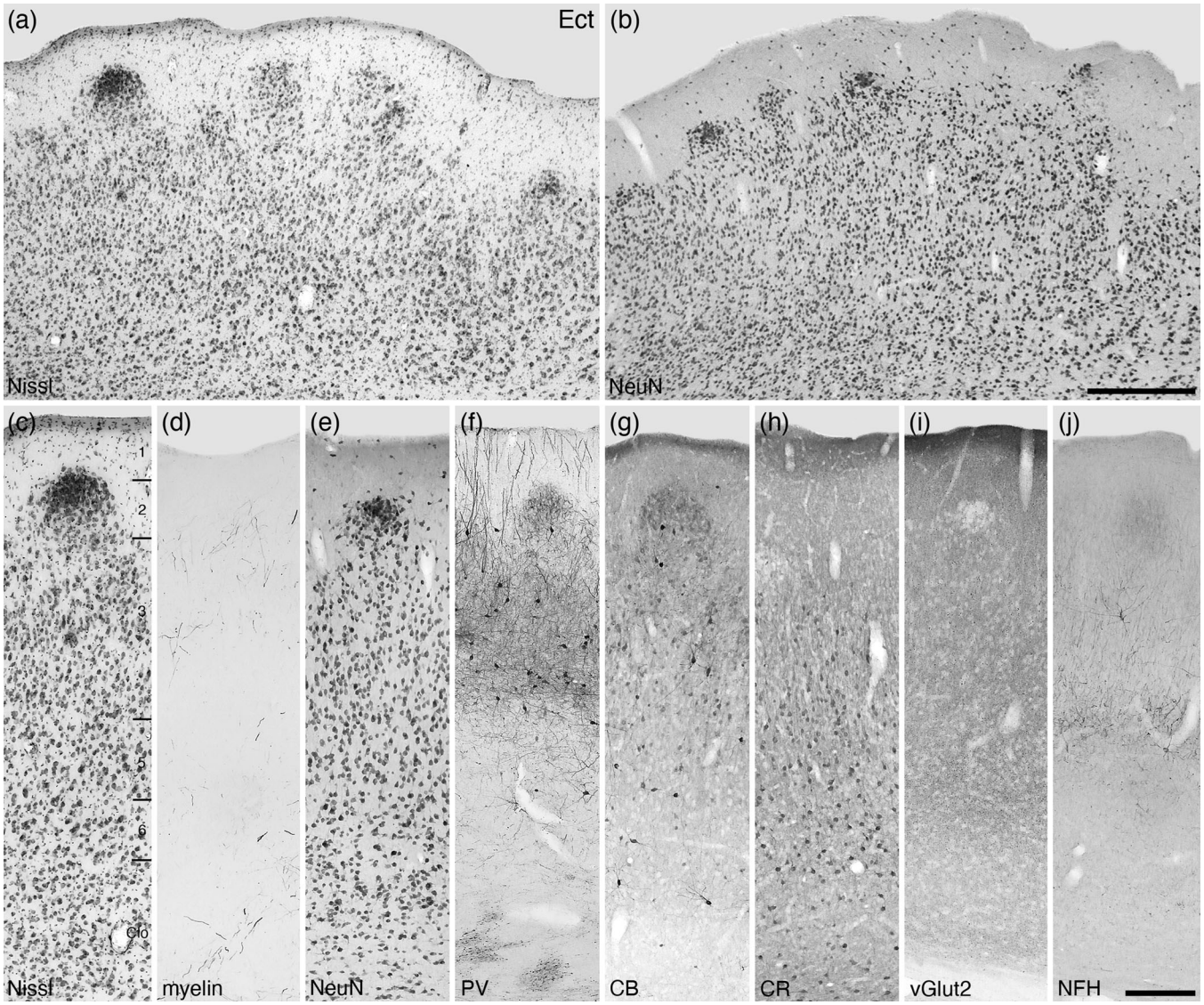

FIGURE 25 Photomicrographs of the ectorhinal cortical area (**Ect**) of the tree pangolin. This agranular five layered cortex lies directly external to the outer division of the claustrum (**Clo**). Note the neuronal clusters that form layer 2 of this cortical area (**a**, **b**, **c**, **e**), which are also evident with **PV** (**f**), **CB** (**g**), **vGlut2** (**i**), and **NFH** (**j**) immunostaining. In all images, the pial surface is to the top. Scale bar in **b** = 500 μm and applies to **a**–**b**. Scale bar in **j** = 250 μm and applies to **c**–**j**. All conventions and abbreviations as in Figure 10

3. Neurofilament H-immunopositive structures were observed in all layers, but these were most dense in layer 6.

A small cortical region at the ventrolateral aspect of the suprasylvian sulcus, at the point where the sulcus became very shallow (Figures 6ii–jj and 8b), was designated as the ventral suprasylvian region (VSS). This six-layered cortical region exhibited a relatively consistent neuronal density through the layers, although layer 2 exhibited a slightly higher relative neuronal density than the other layers (Figure 20a–h). Compared to the adjacent suprasylvian cortical region (MSS and LSS), the VSS was more densely myelinated, with distinct horizontally oriented fibers in upper layer 1, with layers 2 and 3 being more myelin sparse, while layers 4–6 had a higher myelin density, with distinct radially oriented fibers in layer 6. Parvalbumin-immunopositive neurons were observed in layers 2–6, with a relatively homogeneous distribution of these neurons throughout these layers. Palely stained calbindin-immunopositive neurons were found throughout layers 2–6, with layer 2 exhibiting the highest density of these neurons. The occasional intensely calbindin-immunopositive neuron was observed in layer 3. Scattered calretinin-immunopositive neurons were observed in lower layer 1 and layer 6 of the VSS. Vesicular glutamate transporter 2-immunoreactive boutons were observed in all layers, with a very slightly higher relative bouton density being observed in layers 5 and 6. A homogeneous distribution of neurofilament H-immunopositive structures was observed in all layers.

The putative temporal visual cortical region

The temporal region of the visual cortex in carnivores is typically comprised of three distinct cortical areas (Manger et al., 2004; Tusa

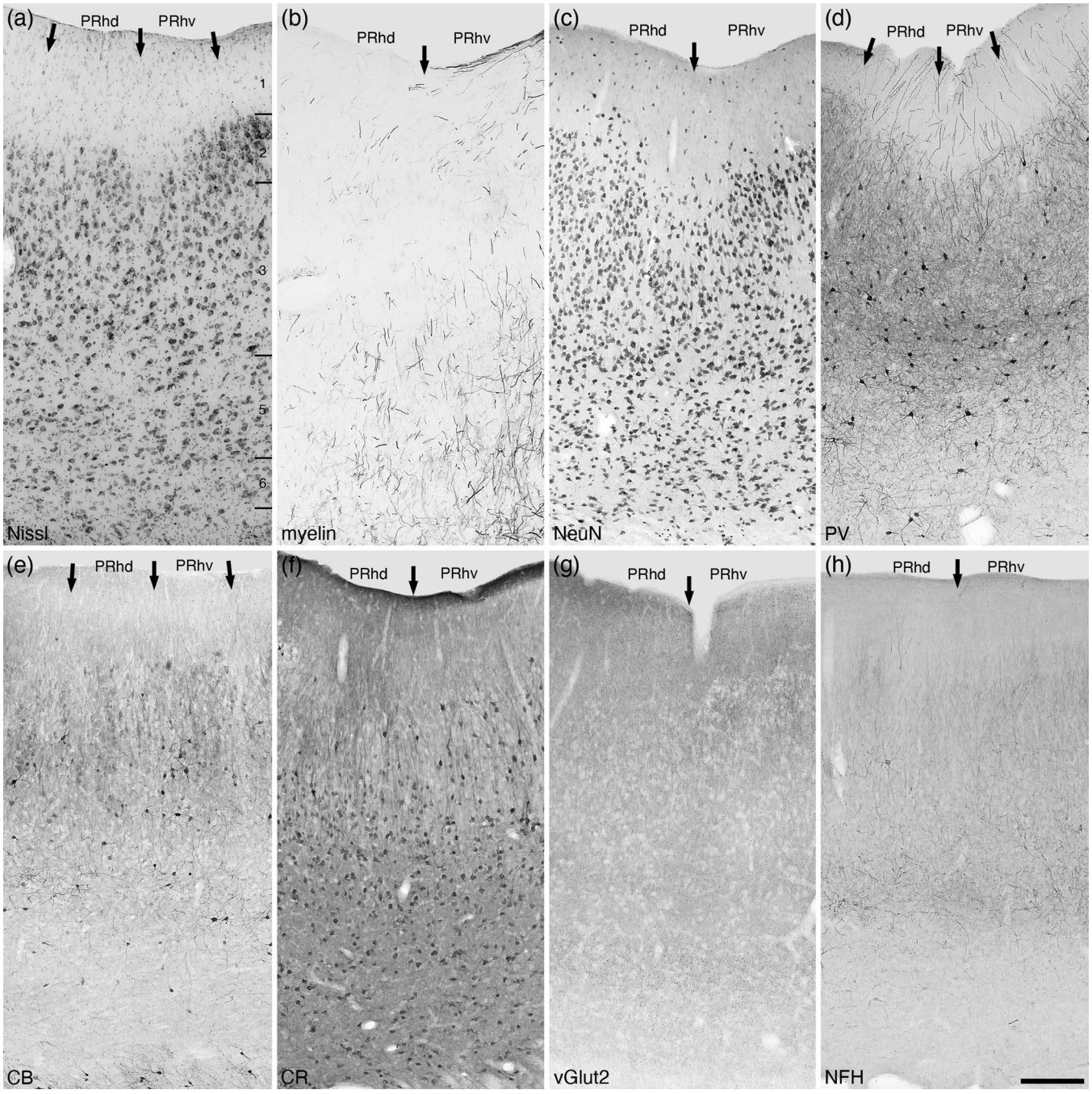

FIGURE 26 Photomicrographs of the perirhinal cortical areas of the tree pangolin. These agranular five layered cortical areas lie dorsally adjacent to the entorhinal cortex. The perirhinal cortex could be subdivided into dorsal (**PRhd**) and ventral (**PRhv**) areas, although there are only subtle differences between these two small cortical areas (the borders of which are marked with **arrows**), such as variances in the densities of parvalbumin (**d**) and calbindin (**e**) immunopositive neurons in layer 3. All conventions, scale bar, and abbreviations as in Figure 10

& Palmer, 1980). In the tree pangolin, with the range of stains used in the current study, this region was cyto-, myelo-, and chemoarchitectonically homogenous and could not be reliably parcellated into distinct cortical areas. The temporal visual cortical region, or Brodmann area 20, of the tree pangolin was located in the caudal ventrolateral aspect of the cerebral cortex (Figures 6hh–oo and 8a,b,d). Area 20 presented with six cortical layers, although the laminar boundaries were not particularly distinct (Figure 20i–p). The neuronal density was homogeneous throughout all cortical layers except the neuron sparse layer 1 and a relatively higher neuronal density being observed in layer 2. Myelinated fibers were present in all cortical layers, with the density of these fibers increasing with depth in the cortex and with distinct radial fascicles being evident in layers 5 and 6. Parvalbumin-immunopositive structures were observed in all cortical layers, although the majority of these structures were observed in layer 3. Palely stained calbindin-immunopositive neurons

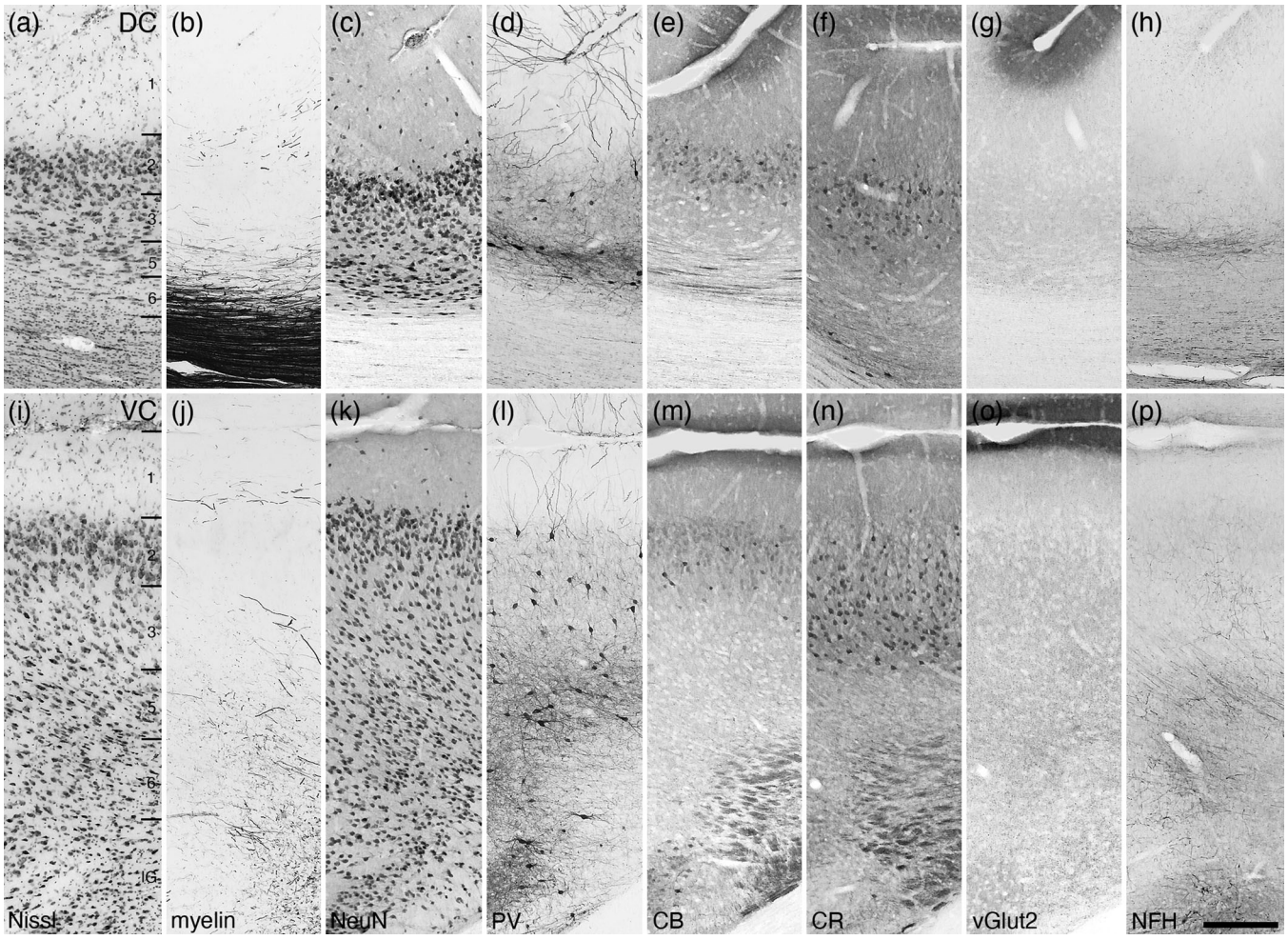

FIGURE 27 Photomicrographs of the dorsal (**DC**, **a**–**h**) and ventral (**VC**, **i**-**p**) cingulate cortical areas of the tree pangolin. Both areas lack a layer 4, with the **DC** being thinner than the **VC** due to the **DC** being located around the fundus of the cingulate sulcus. Note that the **PV** (**d**, **l**), **CR** (**f**, **n**), and **NFH** (**h**, **p**) immunostaining is different between the two cortical areas. All conventions, scale bar, and abbreviations as in Figure 10

were found in layer 2 and upper layer 3, with the occasional intensely stained neuron in lower layer 3. A relatively moderate density of calretinin-immunopositive neurons were observed throughout layers 2–6, although the density was slightly lower in layer 5. Vesicular glutamate transporter 2-immunoreactive boutons were observed in all layers, with a very slightly higher relative bouton density being observed in layers 3 and 4. Neurofilament H-immunopositive structures were observed in all layers, with the highest density being observed in layer 3, while the occasional soma was revealed in layers 4 and 5.

3.3.5 | The putative auditory cortical region

The region defined as auditory cortex was located on the anterior and posterior arms of the ectosylvian gyrus, dorsal, and caudal to the sylvian sulcus. Within this region, we could identify five distinct cortical areas, including the anterior auditory field (AAF), the primary auditory cortex (AI), and a lateral auditory cortical region that could be parcellated into dorsal (ALd), intermediate (ALi), and ventral (ALv) cortical areas (Figures 6v–ii and 8b).

The AAF, found on the anterior arm of the ectosylvian gyrus (Figure 8a, b), is a six-layered cortical area that has a relatively homogeneous distribution of neurons through the layers, although there appears to be a relatively higher neuron density in layer 2 and a lower neuronal density in layer 4 (Figure 21a–h). A low density of horizontally oriented myelinated fibers was found in layer 1, while layer 2 and myelin sparse, and the density of myelin increased with depth in the cortex. In layers 5 and 6, distinct radially oriented myelinated fascicles were present. Parvalbumin-immunopositive neurons were found in layers 2–6, with layers 3 and 5 having the relatively highest density of these neurons. Parvalbumin-immunopositive dendrites were observed in all cortical layers, with these being most dense in layers 2 and 3. Palely stained calbindin-immunopositive neurons were observed in layers 2 and 3, while the occasional intensely stained neuron is observed in layer 5. The majority of calretinin-immunopositive neurons are localized to layers 5 and 6, although scattered neurons were seen in layers 1–4. Vesicular glutamate transporter 2-immunoreactive

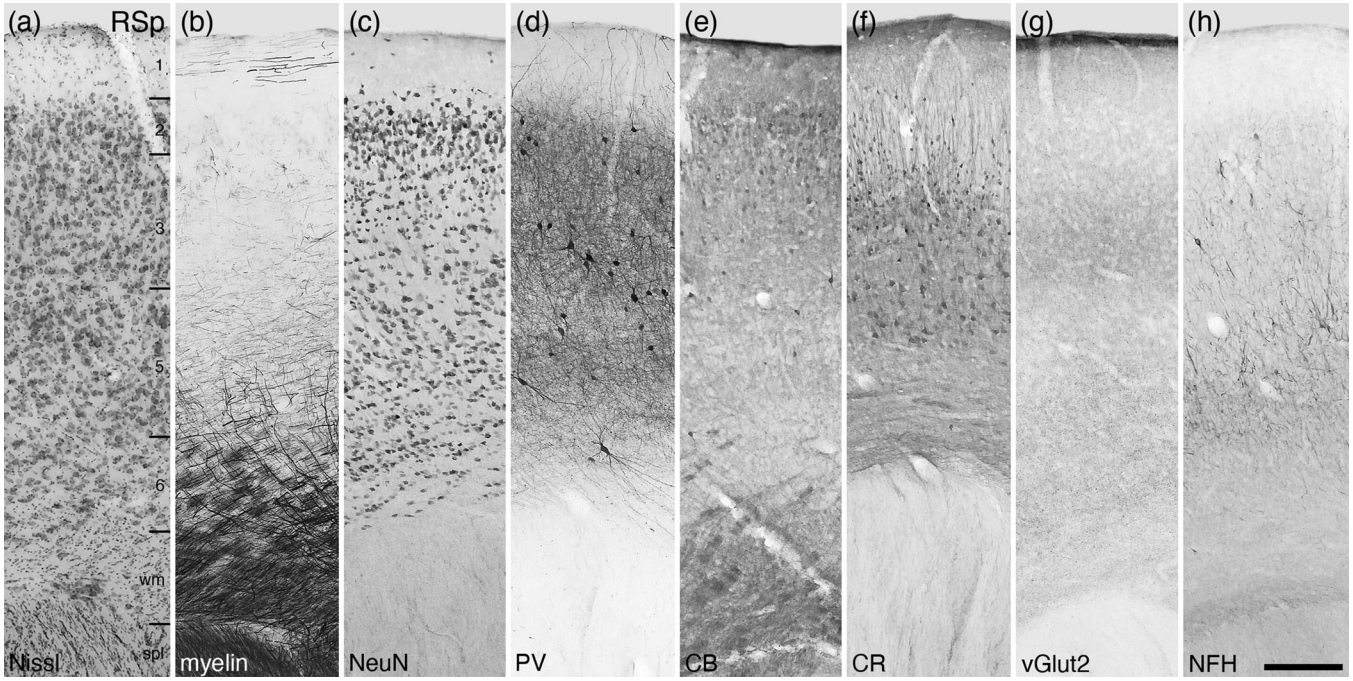

FIGURE 28 Photomicrographs of the retrosplenial cortical area (RSp) of the tree pangolin. This agranular five-layered cortical area lies above the splenium (**spl**) of the corpus callosum, separated from the splenium by a small region of white matter (**wm**). All conventions, scale bar, and abbreviations as in Figure 10

boutons were observed in all layers, with a higher relative bouton density being observed in layer 3. Neurofilament H-immunopositive structures was observed in all layers, with the highest densities being observed in layers 3 and 5.

The primary auditory cortex, AI, is also six-layered cortical area that exhibits a relatively higher neuron density in layer 2 and a slightly lower neuronal density in layer 4 (Figure 21i–p). Layers 1 and 2 are myelin sparse, and the density of myelin increases with depth in the cortex, with distinct radially oriented myelinated fascicles being observed in layers 4–6. Parvalbumin-immunopositive neurons and dendrites are found in layers 2–6, with the relatively density of these neurons being homogeneous across the layers. Palely and intensely stained calbindin-immunopositive neurons are observed only in layers 2 and 3. The majority of calretinin-immunopositive neurons are found in layers 4–6, with a few scattered neurons observed in layers 2 and 3. Vesicular glutamate transporter 2-immunoreactive boutons were observed in all layers, with a significantly higher relative bouton density being observed in layers 3 and 4. Neurofilament H-immunopositive structures were observed in all layers, with the highest densities being observed in layers 3, 5, and 6, as well as the occasional larger neuronal soma being labeled in layer 5.

Lateral to the primary auditory cortex, on the ventral aspect of the posterior arm of the ectosylvian sulcus (Figures 6x–hh and 8b), are three small cortical areas that we designate as the lateral auditory cortical areas, dorsal (ALd), intermediate (ALi), and ventral (ALv). Laterally adjacent to the primary auditory cortex, the ALd presents with a six-layered cortex, with moderately distinct laminar boundaries (Figure 22a–h). The density of neurons across the cortical layers is relatively homogeneous, with a slightly higher neuronal density in layer 2 and a slightly lower neuronal density in layer 4. Horizontally oriented myelinated fibers are found in upper layer 1, while layers 2 and upper layer 3 are myelin sparse. Myelin density increases with depth in the cortex, with distinct radially and horizontally oriented fibers being observed in layers 5 and 6. Parvalbumin-immunoreactive neurons were found in layers 2–6, with the highest relative density of these neurons being observed in layers 3 and 5. Parvalbumin-immunostained dendrites were observed in all layers, with layers 3 and 4 containing the highest densities of these structures. Calbindin-immunoreactive neurons are found primarily in layers 2 and 3, with the occasional neuron being observed in layers 4 and 6. Scattered calretinin-immunopositive neurons are observed in all layers, the majority of which were found in layers 1 and 6. Vesicular glutamate transporter 2-immunoreactive boutons were found in all layers, with a significantly higher relative bouton density being observed in layers 3 and 4. Neurofilament H-immunopositive structures were observed in all layers, with the highest densities being observed in layers 3 and 5, as well as the occasional neuronal soma being labeled in layers 5 and 6.

The ALi, located lateral the ALd, also evinced a six-layered cortex (Figure 22i–p), with similar cytoarchitecture to the ALd (see above). The ALi was less heavily myelinated that the ALd, with increasing densities of myelin from the middle of layer 3 to layer 6. Radially oriented fibers were observed from lower layer 3 to layer 6, with horizontally oriented fibers being located only in layer 6. Very few parvalbumin-immunopositive neurons were observed in the ALi, with most of these being observed in layer 5, with the occasional neuron being seen in layers 3 and 4. The highest density of parvalbumin-immunopositive

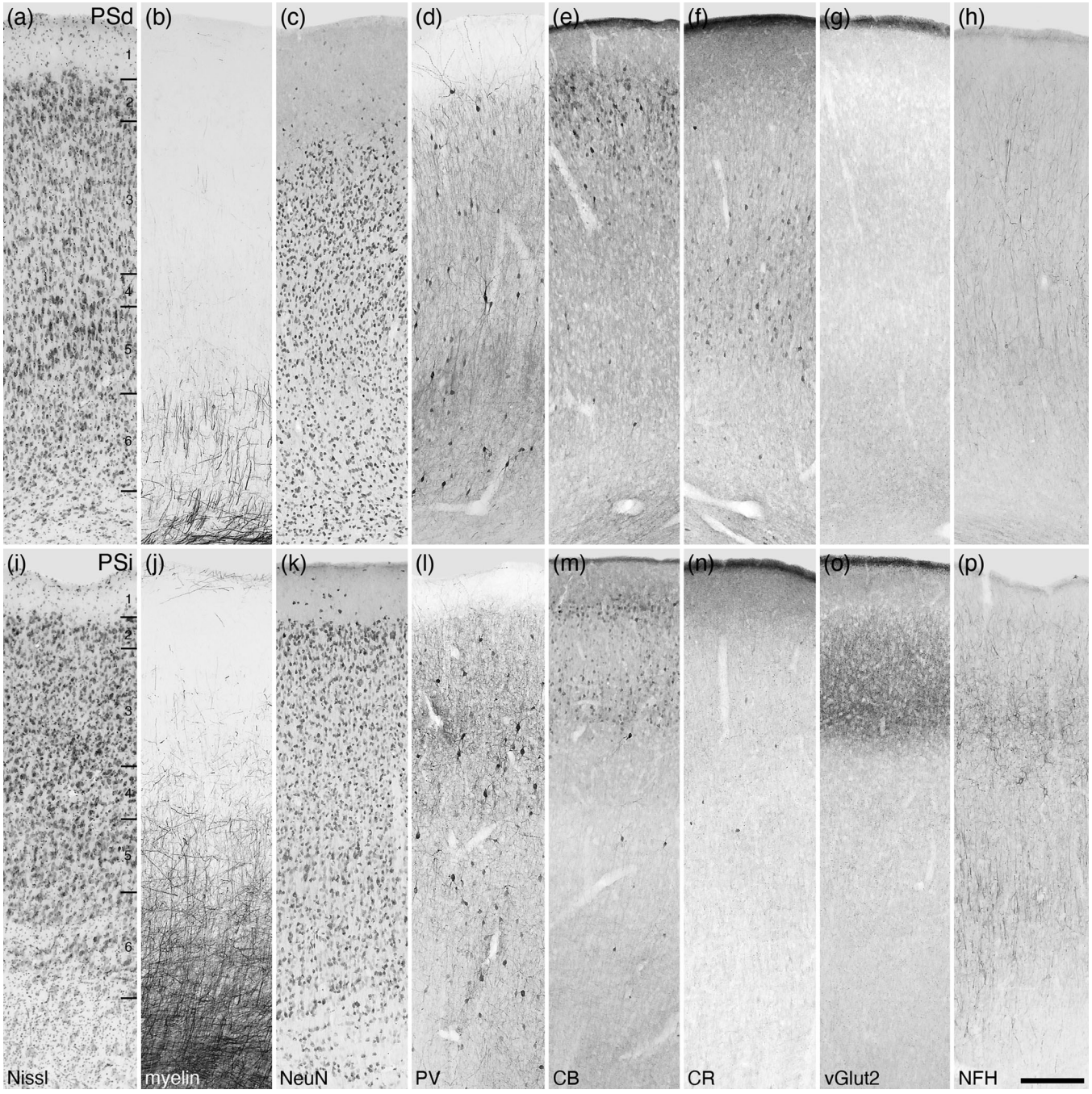

FIGURE 29 Photomicrographs of the dorsal (**PSd**, **a**–**h**) and intermediate (**PSi**, **i**–**p**) areas of the postsplenial cortical region of the tree pangolin. The laminar variances in myelin, **PV**, **CB**, **CR**, **vGlut2,** and **NFH** staining guide the demarcation of these areas. All conventions, scale bar, and abbreviations as in Figure 10

dendrites in the ALi was observed in layer 3. Calbindin-immunopositive neurons were observed in layers 2 and 3, with the very occasional cell observed in layer 4. Scattered calretinin-immunopositive neurons were observed in all cortical layers, the majority being observed in layers 1 and 6. Vesicular glutamate transporter 2-immunoreactive boutons were present in all layers, with a significantly higher relative bouton density being observed in layers 3 and 4. Neurofilament H-immunopositive structures were observed in all layers, with the highest density being observed in layer 3. The occasional neurofilament H-immunopositive neuronal soma was labeled in layers 3, 4, and 5.

The ALv was located lateral to the ALi, and exhibited a relatively homogeneous distribution of neurons through layers 2–6 (Figure 23a–h). The laminar borders in this cortical area were not particular distinct, but were present. Horizontally oriented myelinated fibers were observed in layer 1, while layers 2–4 were myelin sparse, and a relatively low density of horizontally and radially oriented fibers being observed in layers 5 and 6. A relatively low density of

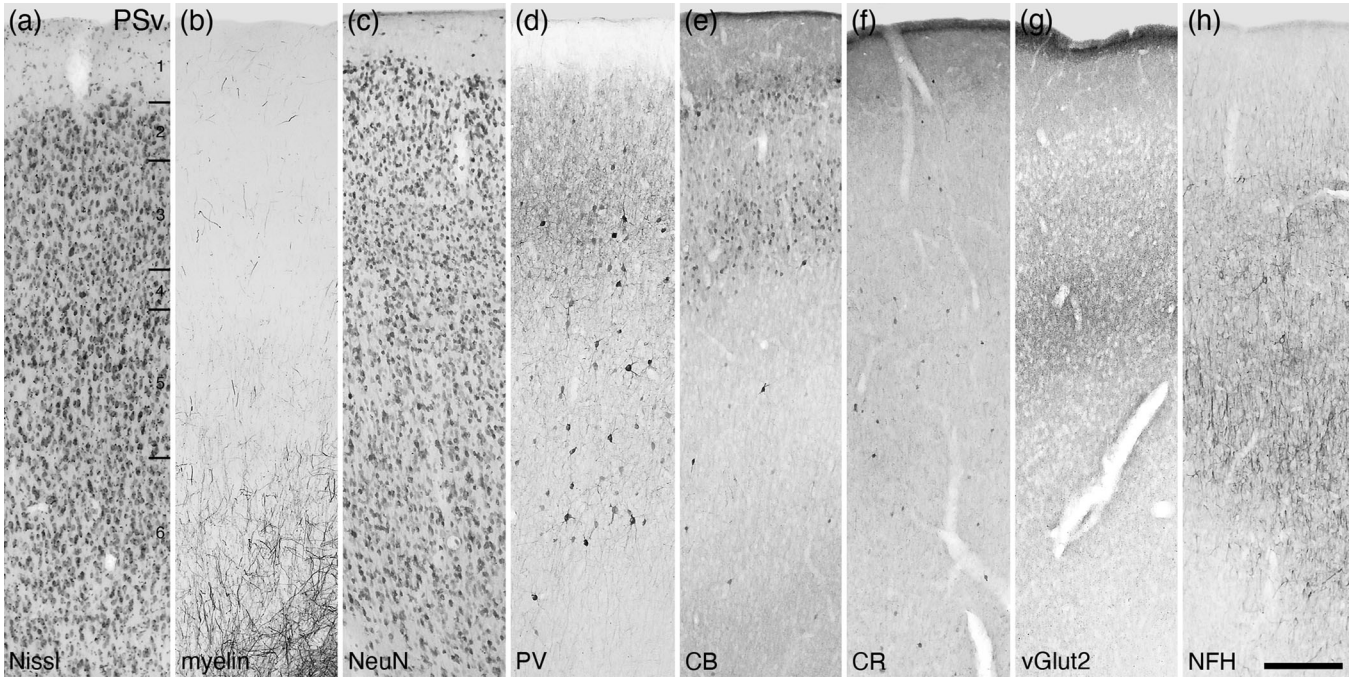

FIGURE 30 Photomicrographs of the ventral area of the postsplenial cortical region (**PSv**, **a-h**) of the tree pangolin. Note the different distribution and presence of structures stained for myelin, **vGlut2,** and **NFH** in comparison to the adjacent postsplenial areas (see Figure 24). All conventions, scale bar, and abbreviations as in Figure 10

parvalbumin-immunopositive neurons were observed in layers 2–5, with layer 3 showing the highest relative density of parvalbumin-immunopositive dendrites. Palely stained calbindin-immunopositive neurons were observed in layers 2–5, while calretinin-immunopositive neurons were mostly location in layers 2, 3, and 6. A relatively low density of vesicular glutamate transporter 2-immunoreactive boutons was present in all layers, with a slight increase in relative density in layers 3 and 4. Neurofilament H-immunopositive structures were observed in all layers, with the highest density being observed in layer 3, and the occasional immunopositive neuronal soma being observed in layers 3 and 4.

3.3.6 | The putative pararhinal cortical region

At the very lateral aspect of the neocortex, mediodorsally adjacent to the rhinal sulcus that defines the boundary of the piriform and entorhinal cortex, a cluster of five cortical areas could be delineated. These include, in rostral to caudal order, the insular cortical area (Ins), the ectorhinal cortical area (Ect), the dorsal (PRhd) and ventral (PRhv) perirhinal cortical areas, and the postrhinal cortical area (POR) (Figures 6e–pp and 8a,b,d).

The cortical region that we term the insular cortex, due to its location above the claustrum and lateral to the prefrontal, motor and somatosensory cortical regions (Figures 6e–l and 8a,b), was a six-layered cortical area (Figure 24a–h). Layer 2 contained the relatively highest density of neurons, while apart from the cell sparse layer 1, layer 4 contained the lowest density of neurons. A low density of horizontally oriented myelinated fibers was observed in layer 1, and in layers 4–6, a mixture of horizontally and radially oriented fibers was observed with radially oriented fibers observed in layers 4 and 6. Myelinated fibers were mostly absent from layers 2 and 3. A high density of parvalbumin-immunopositive dendrites was observed in layers 2–6, with occasional parvalbumin-immunopositive neurons being observed in layers 1 and 2. Calbindin immunostaining revealed palely stained neurons in layers 2 and 3, with the occasional more intensely stained neuron in layers 3 and 4. Calretinin-immunopositive neurons were observed in layers 3–6, with layer 5 containing the highest relative density, followed by layers 3, 6, and 4 in descending order of relative neuronal density. Vesicular glutamate transporter 2-immunoreactive boutons were observed in all layers, with the highest bouton density being observed in the inner half of layer 3. Structures immunopositive to neurofilament H were observed in moderate to high density in layers 2–6, with layers 3 and 4 showing the highest density of immunopositive structures as well as the occasional immunopositive soma.

The ectorhinal cortical area exhibited the most distinct cytoarchitecture of all cortical areas in the tree pangolin cerebral cortex, having distinct high-density neuronal clusters forming layer 2 (Figure 25). The ectorhinal cortical area was agranular, composed of five layers, and was very myelin sparse. The internal half of the neuron sparse layer 1 was interrupted by the distinct layer 2 neuronal clusters. Layers 3, 5, and 6 contained moderate relative densities of neurons, with the neuronal soma of layer 3 being slightly smaller on average that those of layer 5, while the relative neuronal density was slightly lower in layer 6. The ectorhinal cortex exhibited parvalbumin-immunopositive neurons and other structures in all layers, although

the highest densities were observed in layers 2 and 3, with occasional neurons in layer 5 and no parvalbumin-immunopositive neurons in layer 6. The parvalbumin-immunopositive terminal network in layer 2 of the ectorhinal cortex revealed the layer 2 clusters. A low density of calbindin-immunopositive neurons was revealed in all cortical layers, with layers 2 and 3 housing more neurons than the other layers. Calbindin-immunopositive neuropil staining revealed the layer 2 clusters. Moderate densities of calretinin-immunopositive neurons were observed in layers 3, 5, and 6, with those in layer 3 appearing to have smaller soma than those in layers 5 and 6. Vesicular glutamate transporter 2-immunoreactive boutons were observed in all layers, with the relatively highest bouton density being observed in layer 5. Vesicular glutamate transporter 2-immunoreactive boutons appeared to be quite low in density in the regions of the layer 2 clusters. Structures immunopositive for neurofilament H were primarily located in layer 3, with the inner half of layer 3 exhibiting the highest density, while the outer half of layer 3 housed the occasional immunopositive soma. Weak neurofilament-H immunopositive neuropil staining revealed the layer 2 clusters.

The perirhinal cortex was also agranular and composed of five layers (Figure 26). The perirhinal cortex could be divided into dorsal (PRhd) and ventral (PRhv) areas, although the differences between these areas were subtle. In both areas, the neuron sparse layer 1 was located external to a neuron dense layer 2. A moderate density of neurons was observed layer 3, with layer 5 having a relatively lower density of neurons, the density increasing slightly in layer 6. Both areas exhibited a low density of myelin, although the myelin density in layers 5 and 6 of the PRhv appeared slightly higher than the PRhd. Parvalbumin-immunopositive neurons and other structures were observed throughout the cortical layers, but the density of parvalbumin-immunopositive neurons was relatively higher in layer 3 of the PRhd compared to layer 3 of the PRhv. Calbindin-immunopositive neurons were observed in layers 2–5, and the density of calbindin-immunopositive neurons was higher in layer 3 of the PRhv compared to layer 3 of the PRhd. Calretinin-immunopositive neurons were observed in layers 2–5, with the density of calbindin-immunopositive neurons being higher in layer 2 of the PRhv compared to layer 2 of the PRhd. Vesicular glutamate transporter 2-immunoreactive boutons were observed in all layers of both areas, with the highest bouton density being observed in layer 2 in both areas. Immunostaining for neurofilament H revealed structures throughout all layers, with these being most dense in layers 3 and 5 of both areas, with the occasional neurofilament H-immunopositive neuronal soma being observed in layer 3 of the PRhd.

The POR was located caudal to the termination of the rhinal sulcus, occupying the ventrocaudal aspect of the cerebral hemisphere (Figures 6gg–pp and 8b,d). This six-layered cortical area exhibited heterogeneous relative to neuronal densities throughout the layers, with layer 1 being neuron sparse, layer 2 presenting with roughly delineated higher density neuronal clusters, layer 3 having a lower density of neurons and containing some larger neuronal soma, with layers 4, 5, and 6 having a similar neuronal density to layer 3, but being composed of small neurons (Figure 24i–p). The density of myelin in the POR was sparse, exhibiting a steady increase in density with depth in the cortex, with layers 5 and 6 having distinct radially oriented fibers. Parvalbumin-immunopositive neurons were observed in layers 2–6, with layer 3 having the highest relative density of these neurons, while in layer 6, large multipolar pyramidal neurons being evident. Predominantly palely stained, with the occasional intensely stained, calbindin-immunopositive neurons were present only in layers 2 and 3. Calretinin-immunopositive neurons were observed in layers 2–6, with layers 2, 4, and 6 having the highest relative density of these neurons. Vesicular glutamate transporter 2-immunoreactive boutons were observed in all layers, with the highest bouton density being observed in layers 3 and 4. A low relative density of neurofilament H-immunopositive structures was noted in all layers, with these being most dense in layers 3, 5, and 6, with the occasional neurofilament H-immunopositive neuronal soma being observed in layers 4 and 6 of the POR.

3.3.7 | The putative cingulate cortical region

Within the cortex forming the cingulate gyrus and sulcus, we could identify the dorsal (DC) and ventral (VC) cingulate cortical areas. The DC was primarily located around the fundus of the cingulate sulcus, while the VC occupied the cingulate gyrus on the medial wall of the cerebral hemisphere (Figures 6g-dd and 8c). The DC and VC exhibited a very similar cyto-, myelo-, and chemoarchitecture (Figure 27), although the location of the dorsal area surrounding the fundus of the cingulate gyrus makes these differences subtle in nature. Both areas exhibited a five layered cortex, with no clear layer 4 evident. Layer 2 contained the highest neuronal density, followed by layer 5, with layers 3 and 6 having a lower cell density and layer 1 being neuron sparse. Both areas were myelin sparse, with horizontally oriented fibers occurring at the layer 1/2 border and layers 5 and 6 showing a low density of fibers, these being oriented primarily horizontally in the dorsal cingulate area and radially in the ventral cingulate area. Parvalbumin-immunopositive neurons and other structures were observed in all layers, with the highest density of both being observed in layer 5. The density of parvalbumin-immunopositive neurons appears higher in layer 3 of the VC when compared to the DC. In addition, the vertically oriented apical dendrites of layer 2 neurons that invest into layer 1 appear to be more numerous in the DC compared to the VC. Calbindin-immunopositive neurons, both palely and intensely immunostained, are primarily found in layer 2 in both areas. Calretinin-immunopositive neurons were noted to be located within layer 3 in both areas, with an apparent increase in neuronal numbers in layer 3 of the VC compared to the DC. Vesicular glutamate transporter 2-immunoreactive boutons were observed in all layers of both areas, with both areas exhibiting the highest density of these boutons in the upper half of layer 1. Vesicular glutamate transporter 2-immunoreactive boutons showed the highest relative density in layers 5 and 6 of the DC, while the density of these boutons appears consistent across layers 2–6 in the VC, although at higher densities than observed in the DC. Immunostaining for neurofilament H revealed structures throughout all layers, although in both areas, the highest density of these structures was noted in layer 5. A greater density of

neurofilament H-immunopositive structures was observed in layer 3 of the VC compared to the DC.

3.3.8 | The putative retrosplenial and postsplenial cortical areas

The retrosplenial cortical area (RSp) and three postsplenial cortical areas (dorsal PSd, intermediate PSi, and ventral PSv) comprise the caudal rim of the cerebral cortex that bridges the region between the hippocampal formation, and the cingulate cortex dorsally (the RSp) and the entorhinal cortex ventrally (the postsplenial areas) and the postrhinal and primary visual cortical areas caudally (the postsplenial areas) (Figures 6z–qq and 8c,d).

The retrosplenial cortex, found between the hippocampal formation and the cingulate cortex (Figures 6z–hh and 8c), appears to be composed of a single cortical area. Within the RSp, a moderate density of neurons was observed to form five layers, with a discernable layer 4 (Figure 28). The highest density of neurons was observed in layer 2, followed by layers 5 and 6, with layers 3 and the neuron sparse layer 1 exhibiting lower neuronal densities. A low density of myelinated axons was observed in this cortical area, with distinct horizontally oriented fibers being present in layers 1, 5, and 6, while in layers 5 and 6, radially oriented fibers were observed. Very few myelinated fibers were observed in layers 2 and 3. Parvalbumin-immunopositive structures were observed in all cortical layers, with a low density of neurons being found in layers 2–6, while these layers exhibited a high-density parvalbumin-immunopositive dendrites. Palely stained calbindin-immunopositive neurons were observed in layer 2 and upper layer 3, while the occasional intensely immunostained neuron was observed in layers 3 and 5. Intensely stained calretinin-immunopositive neurons with small soma were observed in layers 2 and 3, while in layer 5, palely stained larger neurons were observed. Vesicular glutamate transporter 2-immunoreactive boutons were observed in all layers and showed the highest relative density in the very superficial portion of layer 1 and in layers 3 and 6. Immunostaining for neurofilament H revealed structures throughout layers 2–6, although the highest density of these structures was noted in layer 5. Neurofilament H-immunopositive soma were observed in layer 3.

The dorsal post-splenial area (PSd) was a six-layered cortical area, characterized by a higher relative density of neurons in layer 2, a lower relative density of neurons in layer 4, and relatively larger neuronal somata in layer 5 (Figure 29a–h). This cortical area was very myelin sparse with loosely packed radially oriented fibers observed in layer 6. Parvalbumin-immunopositive neurons were found in layers 2–6, these being most common in layers 2, 4, and 6, with a substantive parvalbumin-immunopositive neuropil staining observed in layer 5. A mixture of palely and intensely calbindin-immunoreactive neurons was observed primarily in layer 2 and upper layer 3. Calretinin-immunopositive neurons were observed in lower layer 3, layer 4, and layer 5, with the occasional neuron in layer 6. A relative low density of vesicular glutamate transporter 2-immunoreactive boutons was observed in all layers with a slight increase in relative density in layers 3 and 6. A relatively low density of neurofilament H-immunopositive structures was found in all cortical layers, with a slightly higher density observed in layers 3 and 5, as well as the occasional soma in layer 5.

The intermediate postsplenial area (PSi) also had six layers, but with a relatively homogeneous neuronal density across layers, although it is slightly higher in layer 2 (Figure 29i–p). Layers 1–3 were relatively myelin sparse, while the density of both horizontally and readily oriented fibers increased with depth in the cortex through layers 4, 5, and 6. Parvalbumin-immunopositive neurons were found in layers 2–6, the majority of these neurons being observed in layers 3 and 5. The density of parvalbumin-immunopositive dendrites was highest in layer 3. Calbindin-immunopositive neurons were primarily found in layer 2 and inner layer 3, with scattered neurons in the other layers. Only a very few calretinin-immunopositive neurons were observed in the PSi, these being in layers 3 and 4. A relatively higher density of vesicular glutamate transporter 2-immunoreactive boutons was observed in all layers of the PSi (compared with the PSd) with a significant increase in relative density in layer 3. Neurofilament H-immunopositive structures were found in all cortical layers, with a slightly higher density observed in layers 3 and 5, as well as the occasional soma in layer 3.

The six-layered ventral postsplenial area (PSv) evinced a relatively homogeneous neuronal density throughout the layers, with the subgranular cortical layers appearing to have slightly larger neurons than the supragranular layers (Figure 30). Parvalbumin-immunopositive neurons were observed in layers 3–6, the majority of which were located in layers 3 and 5. The layer 5 parvalbumin-immunopositive neurons appeared to have larger soma than those in layer 3. The distribution of calbindin-immunopositive neurons in the PSv was similar to that observed in the PSi, with neurons found in layer 2 and inner layer 3, as well as scattered neurons in layers 4–6. A slightly higher number of calretinin-immunopositive neurons (in comparison to the PSi) were observed in all layers of the PSv, but these neurons were not numerous. Vesicular glutamate transporter 2-immunoreactive boutons were observed in all layers of the PSv with a significant increase in relative density in layer 4. Neurofilament H-immunopositive structures were found in all cortical layers, with a higher density observed in layer 5, as well as the occasional soma in layers 3 and 5.

4 | DISCUSSION

The current study provides a comprehensive analysis of portions of the pallial telencephalon of the tree pangolin that had not been previously described, including the claustrum and endopiriform nucleus, the subcortical white matter including the WMICs, and the cerebral cortex. Descriptions of the olfactory portions of the pallial telencephalon (Imam et al., 2018a), the hippocampal formation (Imam et al., 2019a), and amygdaloid complex (Imam et al., 2022a, b) have been provided previously and are not considered here. The organization of the pallial telencephalon of the tree pangolin is consistent with that observed across mammals generally, although subtle variations are present. Here we compare and contextualize the organization of the pallial telencephalon observed in the tree pangolin with that in other mammal

species, noting both the conserved organization as well as the subtle variations revealed, and whether these subtle variations may relate to the life history of the tree pangolin. Additionally, nothing specifically distinct about the organization of the tree pangolin cerebral cortex was noted, in that no additional regions or areas that do not appear to have equivalents in other mammals were noted.

4.1 | Claustrum and endopiriform nuclear complex

The anatomical organization of the claustrum and endopiriform nuclear complex have been examined across a broad range of mammals (e.g., Baizer et al., 2014; Johnson et al., 1994; Kowianski et al., 1999; Real et al., 2003; Smith et al., 2018). In the tree pangolin, we noted the absence of a distinct white matter region (the extreme capsule) separating the claustrum and endopiriform nuclear complex from the overlying neocortex and piriform cortex, respectively, which has been termed claustrum Type 1 (Kowianski et al., 1999). The absence of a visible, distinct, extreme capsule separating these nuclei from the overlying cortex is thought to be the primitive, or basal, condition in mammals based on the absence/presence of the extreme capsule across mammals (Johnson et al., 1994). The Carnivora, which is the sister order of the pangolins (Pholidota; Foley et al., 2016) are noted to have a distinct extreme capsule (Johnson et al., 1994; Patzke et al., 2014). In this respect, the organization of these nuclei in the tree pangolin correlates with the basal mammalian condition, and any potential advantage to neural processing acquired through the presence of the extreme capsule (which remains unknown) would not be afforded to the tree pangolin. In addition, it appears that the presence of an extreme capsule has evolved multiple times across mammals (Johnson et al., 1994), although the variations in the detailed appearance of the extreme capsule (Kowianski et al., 1999) indicate that these are likely to be multiple independent evolutionary events in the various lineages where present.

The range of stains used in the current study allowed the delineation of inner and outer divisions of the claustrum in the tree pangolin. Rostrally, the outer division of the claustrum appears to form "islands" within the inner division, but caudally, these form two distinct lamina that run parallel to the inner surface of the cerebral cortex (see Figure 1). This insular and laminar organization has been observed in the claustrum of other mammals using a range of approaches (e.g., Baizer et al., 2014; Real et al., 2003; Smith et al., 2018), indicating that what is observed in the tree pangolin supports the concept that the claustrum is not a homogeneous structure with a unitary function, but that this heterogeneity is likely related to the connectivity of claustral divisions to different regions, or portions within a region, of the cerebral cortex (e.g., Baizer et al., 2014).

An extensive range of markers have established the organization of the claustrum in the laboratory rat (for review, see Smith et al., 2018). In the rat, there appears to be no variation in neuronal density throughout the claustrum (Smith et al., 2018), a variation that was observed between the inner (lower neuronal density) and outer (higher neuronal density) divisions of the tree pangolin. In the laboratory, rat parvalbumin immunostaining is reported to be richer in the ventral claustrum compared with the dorsal claustrum (Smith et al., 2018), which parallels the richer parvalbumin immunostaining the outer division and poorer staining in the inner division of the tree pangolin claustrum. Thus, very tentatively, as additional markers are needed for confirmation, the inner and outer divisions of the claustrum in the tree pangolin may potentially be considered homologous to the dorsal and ventral divisions of the claustrum in the laboratory rat, respectively (Smith et al., 2018). As this is only a very tentative proposal of homology, we have cautiously used different terminology to describe the divisions of the claustrum in the tree pangolin to that used in the laboratory rat until these possible homologies are clarified. In addition, it should be noted that immunostaining for the calcium-binding proteins in both cat (Rahman & Baizer, 2007) and monkey (Reynhout & Baizer, 1999) did not reveal an specific parcellation of the claustrum in these species.

The endopiriform nuclear complex of the tree pangolin could be parcellated into three nuclei—dorsal, intermediate, and ventral. This nuclear organization appears to conform to that reported in the brains of laboratory rodents (e.g., Paxinos & Watson, 2007; Watson & Puelles, 2017) and primates (e.g., Paxinos et al., 2000; Paxinos et al., 2012), and may be indicative of the nuclear organization of the endopiriform nuclear complex across mammals generally (Smith et al., 2018). In this sense, the functional aspects of the endopiriform nuclear complex in the tree pangolin likely correlate with that observed in other mammals, especially given the organization of the olfactory system in the tree pangolin (Imam et al., 2018a). Furthermore, these observations across species indicate that variations in the organization the endopiriform nuclear complex are likely to be few across mammals.

4.2 | Laminar organization of the white matter

Parvalbumin-immunostaining revealed a trilaminate organization of the subcortical white matter in the tree pangolin, an organization confirmed with both Nissl and myelin staining. To our knowledge, this laminate organization of the subcortical white matter has not been specifically described in other mammal species, but is likely to be present (e.g., Schmahmann & Pandya, 2006), although perhaps not as readily observed as in the tree pangolin. This laminar organization does not apply to either commissural projections, or to projections to sites distant to the cerebral cortex, as neither the corpus callosum nor the internal capsule contained these parvalbumin-immunopositive axons. It seems reasonable then to conclude that the laminate organization of the white matter observed applies specifically to ipsilateral corticocortical connections. While there is clearly a significant proportion of these axons immunolabeled with parvalbumin, indicating that they are likely to be inhibitory projections (although this cannot be stated definitively, see Gritti et al., 2003), the axons within the lamina are likely to primarily arise from excitatory neurons. It is unclear what functional significance this organization of the white matter might have, but speculatively, it may be an advantageous organization of the ipsilateral corticocortical pathways that allows a reduction in the overall volume of axonal tissue required for efficient connectivity and neural

information processing (e.g., Ringo et al., 1994), as well as reduced energetic requirements (e.g., Isler & van Schaik, 2006; Mink et al., 1981).

4.3 | White matter interstitial cells

Within the subcortical white matter of the tree pangolin, approximately 3.2 million WMICs, or white matter neurons, were revealed with immunostaining for NeuN marker. Approximately 14.7% of these white matter neurons were calretinin-immunopositive, while a small number were parvalbumin-immunopositive. The majority of these neurons were located close to the inner border of the cerebral cortex, although they were observed throughout the white matter, albeit it at much lower densities with distance from the gray matter. These observations align with earlier observations on the WMICs made in other mammal species, including, but not limited to, the laboratory rat (Clancy et al., 2001), megachiropteran bats (Bhagwandin et al., 2020), and primates (e.g., Beasley et al., 2002; Eastwood & Harrison, 2005; Emery et al., 1997; Mortazavi et al., 2017; Sedmak & Judaš, 2019; Swiegers et al., 2019, 2021a, b). While neurochemical phenotypes of other potential types of WMICs (such as those that may contain neuronal nitric oxide synthase, somatostatin, or neuropeptide Y) were not explored in the current study, the percentage of these neurons that are calretinin-immunopositive, with the few parvalbumin-immunopositive neurons, indicates that the proportions of a range of neurochemical phenotypes within this neuronal population in the tree pangolin is likely to be very similar to that observed in other mammals. In addition, the total number of white matter neurons appears to be close to what one would expect for the brain mass of the tree pangolin when compared to other species in which these have been quantified (Bhagwandin et al., 2020; Swiegers et al., 2019, 2021a, b). Given these broad similarities, it would be reasonable to assume that the functional role of these white matter neurons, whatever that may be (Colombo, 2018; Kilduff et al., 2011), is likely to be similar in the tree pangolin to other mammals.

4.4 | The cerebral cortex

Our comprehensive architectonic analysis of the tree pangolin cerebral cortex revealed a number of interesting findings. These include: the pyramidalization of layers 2 and 4 with a low number of neurons within layer 4; the general parcellation of the cerebral cortex into 38 cortical areas; the lack of gigantopyramidal neurons (or Betz cells) in the motor cortical region; and a subtle, but noteworthy, expansion of the auditory cortical region.

4.4.1 | Laminar organization and pyramidalization of the tree pangolin cerebral cortex

Determining the precise laminar organization of the cerebral cortex in the tree pangolin is not a straightforward task, as three variations to the "standard" model of cortical organization in mammals were observed. The first involves layer 2, where rather than being composed of distinct granular cells, the neurons forming layer 2 in the tree pangolin exhibit a pyramidal shape. Despite this alteration in the shape of the soma of the layer 2 neurons, this layer is present in all neocortical areas and generally exhibits the highest neuronal density of all layers. Thus, layer 2 of the tree pangolin neocortex can be considered to have undergone pyramidalization. The second variation of note is the often-indistinct boundaries between the cortical layers seen with cyto- and myeloarchitectural stains. The range of stains used in the current study assisted in the determination of the layer boundaries in the tree pangolin, but even with the broad range of stains used, a high degree of precision in the determination of these boundaries was not possible. This also occurred in the primary sensory areas, where often, the layer boundaries are most readily observed. The third variation of note is the altered appearance of layer 4 in the cortical regions where it could be identified. While certain areas, such as the prefrontal and motor cortex, were clearly agranular (i.e., lacking a layer 4), a modified layer 4 could be identified in the putative sensory regions of the neocortex. This modified layer 4 consisted of a visibly lower density of neurons, and rather than the soma of these neurons being granular in shape, they were pyramidal in shape. Thus, like layer 2, layer 4 in the tree pangolin has undergone pyramidalization, and in addition, the neuronal density is lower.

These three variations in the laminar organization of the cerebral cortex have been noted in other mammalian species, initially by Brodmann (1909), and are quite distinct in the cerebral cortex of the cetaceans (Manger, 2006), African elephant (Manger et al., 2009) and pygmy hippopotamus (Butti et al., 2014). In the Florida manatee, pyramidalization or absence of layers 2 and 4 has been noted in certain, but not all, regions of the cortex, as well as some cortical areas having indistinct layer boundaries, although some cortical areas exhibit quite distinct layer boundaries (Marshall & Reep, 1995; Reep et al., 1989). Layer 4 is also consistently reported to be absent from the motor cortex and portions of the prefrontal cortex across mammalian species (e.g., Brodmann, 1909; Shipp et al., 2013), but recent studies have indicated that it is possible that these neurons have undergone changes in their developmental processes (for example, changes to *Protocadherin20*) leading to an ectopic location of the true layer 4 neurons, along with pyramidalization of these neurons (Oishi et al., 2016; Yamawaki et al., 2014). Interestingly, protocadherins are often expressed in both the brain and the skin (Biswas, 2018), and the species with the noted differences in lamination of the cerebral cortex, all have quite unusual skin compared to other mammals. It is possible, although highly speculative, that there is a link between the genetic variations required to evolve skin types that allow mammals to inhabit vacant ecological niches and possibly neutral pleiotropic effects that alter the development and adult expression of the cortical layers. Such a speculative scenario may also apply to understanding the unusually organized, but functionally patent, locus coeruleus complex of the tree pangolin (Imam et al., 2018b). Alterations to specific gene complexes in humans can lead to neurocutaneous syndromes, such as tuberous sclerosis, where both skin and brain (amongst other organs) are affected (e.g.,

Islam & Roach, 2015; Randle, 2017). Changes in these gene complexes, the TSC genes, may be candidates for revealing the mechanisms leading to the potentially linked cutaneous and neural variations observed in the tree pangolin and other mammals with neurocutaneous features that distinguish them from more commonly studied species.

4.4.2 | Areal organization of the tree pangolin cerebral cortex

While speculations regarding the causal factors producing the unusual cortical lamination observed in the tree pangolin are of interest theoretically at present, it is clear that the laminar organization of the cerebral cortex in the tree pangolin is quite different to "typical" mammals, and this presents a challenge in delineating specific homologous cortical regions and areas in this species, as certain features that are characteristic of particular cortical areas (such as a prominent layer 4 in the primary sensory areas) could not be employed as strongly supported criteria. The range of stains employed in the current study was necessary to allow us to determine the cortical areas reported, and the delineation of these cortical areas was based on the presence of three or more consistent differences in the expression patterns of structures stained between adjacent cortical regions and areas. In addition, it must be noted that the architectonic map provided, and the cortical areas named, are all done in a putative manner, as no electrophysiological mapping, or other techniques, used to determine precisely where specific sensory, motor, or other neural systems are located has been undertaken in the tree pangolin—the implied homologies of cortical areas in the tree pangolin in comparison to other species are hypothetical at present. Despite these caveats, the similarity of the sulcal and gyral pattern of the tree pangolin cerebral cortex to that observed in carnivores (Imam et al., 2017), and the localization of what appear to be primary sensory areas that correlate topographically in relation to the homologous sulci and gyri in carnivores, allows us to be reasonably confident that the assignation of names for the specific cortical areas identified are likely to be homologous to those reported in other species where often multiple approaches have allowed the accurate delineation of these areas.

Broadly, the location of the different cortical regions (such as frontal, motor, somatosensory, auditory, cingulate, and so forth) reported here for the tree pangolin correspond to that reported in other mammals (Kaas, 2017) and bear a strong resemblance in terms of the areal organization to that observed in carnivores (e.g., Scannell & Young, 1993). This similarity in the cortical organization of the tree pangolin and carnivores extends, to a reasonable extent, to the specific cortical areas identified in cortical regions. For example, within the visual cortical region of the tree pangolin, we identified several cortical areas that can be proposed to be directly homologous to those observed in carnivores (such as the SVA, areas 17, 18, 19, and 21) (Manger et al., 2002a; Tusa et al., 1978; Tusa et al., 1979; Tusa & Palmer, 1980). In the regions demarcated as the posterior parietal, suprasylvian, and temporal visual regions, there appears to be correspondence to similar regions in the carnivore visual cortex, but we could not subdivide these regions into the numerous cortical areas reported in carnivores. The suprasylvian cortex of the carnivores is comprised of six distinct cortical areas (AMLS, PMLS, ALLS, PLLS, DLS, and VLS) (Homman-Ludiye et al., 2010; Palmer et al., 1978), while in the tree pangolin, we noted the MSS that we believe corresponds to the AMLS and PMLS, the LSS that we believe corresponds to the ALLS and PLLS, and the VSS which we propose corresponds to the DLS and VLS. In the posterior parietal region of the carnivores, two cortical areas are noted (5 and 7 in the cat, Pigarev & Rodionova, 1998; PPr and PPc in the ferret, Manger et al., 2002b), whereas in the tree pangolin, we could not subdivide this region. Similarly, in the carnivore temporal visual cortex, three areas are identified (20a, 20b, and PS) (Manger et al., 2004; Scannell & Young, 1993; Tusa & Palmer, 1980), and in the tree pangolin, we could only identify the region and not the cortical areas contained within this region.

If we consider the somatosensory cortex, composed of five areas in most mammals (Kaas, 2017), the areas identified as somatosensory in the tree pangolin follow this organization. Similar equivalencies of cortical areas within regions when comparing the tree pangolin to other mammals can be made for the motor cortical areas, auditory cortical areas (see below for more detail), insular and pararhinal cortical areas, cingulate cortex, and prefrontal cortex. In this sense, the parcellation and arealization of the areas and regions of the cerebral cortex in the tree pangolin align with many observations made in other mammals (Kaas, 2017). Additionally, nothing specifically distinct about the organization of the tree pangolin cerebral cortex was noted, in that no additional regions or areas that do not appear to have equivalents in other mammal species were noted.

4.4.3 | Motor cortex and the lack of gigantopyramidal (Betz) neurons

The primary motor and premotor cortical areas of mammals are often readily identified, and their extent defined, by the presence of gigantopyramidal neurons (or Betz cells) (e.g., Badlangana et al., 2007; Betz, 1874; Brodal, 1968, 1978; Jacobs et al., 2018). In contrast to the regularly reported occurrence of gigantopyramidal neurons in layer 5 of the motor cortex across mammals, in the tree pangolin, no distinct larger pyramidal neurons located in layer 5 of the presumptive primary motor cortex or the presumptive premotor cortex were identified. The absolute size of the gigantopyramidal neurons does not appear to be dependent upon the size/length of the axon that is required for the action potentials to move from primary motor cortex to the ventral horn of the spinal (e.g., Badlangana et al., 2007). Rather, it appears that the largest gigantopyramidal neurons are found in species that require concerted and rapid activation of several major muscle groups simultaneously, such as during the act of pouncing during predation in the big cats (Jacobs et al., 2018).

The corticospinal tract of the tree pangolin is unusual, in that it decussates rostrally within the medulla and appears to send many of its axons to the hypoglossal nucleus (Imam et al., 2019c). In addition, the spinal cord of the tree pangolin is very short (Imam et al., 2017),

although the internal organization of this spinal cord is similar to that observed in other mammals (Imam et al., 2022c). In this sense, it may be argued that the length of the axons that need to be supported by the layer 5 pyramidal neurons in the motor cortex are not exceptionally, and indeed are likely to be quite short, which may lead to a general reduction in the size of the layer 5 soma; however, this reasoning can be questioned by the observations made in giraffe (Badlangana et al., 2007).

The largest gigantopyramidal neurons reported in the mammalian primary motor cortex were found in species classified within the genus *Panthera* (lions, leopards, and tigers) (Jacobs et al., 2018). The common attribute of these *Panthera* species is the locomotory demands placed on these animals during the "kill" phase of hunting, where rapid, simultaneous, precise, contractions, and relaxations of major muscles groups are required. Tree pangolins exhibit quadrupedal walking, bipedal walking, and arboreal climbing often employing the prehensile tail (Kingdon, 1971). The locomotor repertoire employed by the tree pangolin is relatively slow, often employing "deliberate" movements that do not involve the need for precisely coordinated whole-body movements. It is possible that this difference in the locomotory styles and associated neural demands contributes to our inability to observe gigantopyramidal neurons in layer 5 of the motor cortex of the tree pangolin, as the potential function attributed to these gigantopyramidal neurons is not required for locomotion in the tree pangolin.

4.4.4 | Is there a specialization of the auditory cortex of the tree pangolin?

In our previous studies of the diencephalon and brainstem of the tree pangolin, we noted a modular arrangement within the ventral division of the medial geniculate nucleus of the dorsal thalamus revealed with parvalbumin immunostaining (Imam et al., 2019b), and the architectonic refinement of the lateral superior olivary nucleus and nucleus of the trapezoid body (Imam et al., 2019c). These features, while not specifically indicating an auditory specialization in the tree pangolin, do indicate that the sense of hearing in the tree pangolin is likely to be enhanced in subtle ways, through refinement and modularization of existing neural pathways, rather than the addition of novel nuclei as seen, for example, in the African elephant medial geniculate body and superior olivary nuclear complex (Maseko et al., 2013). In the current study, our analysis revealed the existence of five distinct putative auditory cortical areas, the organization of which broadly resembles that seen in carnivores such as the cat (e.g., Reale & Imig, 1980) and ferret (e.g., Bizley et al., 2005). The proportion of the cortical sheet occupied by these auditory cortical areas in the tree pangolin also seems to be slightly larger, based on a qualitative assessment, than might be observed in the cat and ferret. Thus, there are several indications that, despite the primacy of the olfactory sense for the tree pangolin (Imam et al., 2018a), the auditory sense appears to be the next most important sensory system.

Previously, we indicated that these subtle refinements of the auditory system in the tree pangolin may relate to the localization of prey (Imam et al., 2019b, c). In terms of the life history of the tree pangolin, we propose that the olfactory sense may be used to locate termite mounds or ant nests at a distance, and once these are found and the tree pangolin is digging into these mounds/nests, the auditory detection of the communicative stridulation sounds produced by ants and termites may guide the excavating pangolin in the direction of the majority of ants/termites within the nest/mound. The current, albeit qualitative, indication of a slightly proportionally larger portion of the cortex putatively devoted to the processing of sounds, supports the previous findings regarding the auditory system and supports the concept of the use of audition in localization of abundant prey sources. Further studies of the anatomical and behavioral basis of audition in the tree pangolin may allow an in-depth understanding of the potentially combinatorial use of the olfactory and auditory senses in the location of nutrition.

ACKNOWLEDGMENTS

We thank Dr. Elizabeth Ebewele of the Department of Forestry, Federal Ministry of Environment, Nigeria, for her assistance in helping to facilitate the issuance of the CITES permit.

CONFLICT OF INTEREST

The authors declare no conflicts of interest.

AUTHOR CONTRIBUTION

PRM conceptualized the study. AI, AB, MSA, and PRM obtained the brains. AI, AB, and PRM performed the staining and analysis. AI and PRM wrote the manuscript, and the remaining authors contributed to the editing and improvement of the early drafts of the manuscript. All authors had full access to all data in the study and take responsibility for the integrity of the data and the accuracy of the data analysis.

DATA AVAILABILITY STATEMENT

Data have not been shared due to this study being based on histological sections.

PEER REVIEW

The peer review history for this article is available at https://publons.com/publon/10.1002/cne.25349

REFERENCES

Arnason, U., Adegoke, J. A., Gullberg, A., Harley, E. H., Janke, A., & Kullberg, M. (2008). Mitogenomic relationships of placental mammals and molecular estimates of their divergences. *Gene*, *421*, 37–51. https://doi.org/10.1016/j.gene.2008.05.024

Badlangana, N. L., Bhagwandin, A., Fuxe, K., & Manger, P. R. (2007). Observations on the giraffe central nervous system related to the corticospinal tract, motor cortex and spinal cord: what difference does a long neck make? *Neuroscience*, *148*, 522–534. https://doi.org/10.1016/j.neuroscience.2007.06.005

Baizer, J. S., Sherwood, C. C., Noonan, M., & Hof, P. R. (2014). Comparative organization of the claustrum: What does structure tell us about function? *Frontiers in Systems Neuroscience*, *8*, 117. https://doi.org/10.3389/fnsys.2014.00117

Barbaresi, P., Fabri, M., & Mensa, E. (2014). Characterization of NO-producing neurons in the rat corpus callosum. *Brain and Behavior*, *4*, 317–336. https://doi.org/10.1002/brb3.218

Beasley, C. L., Cotter, D. R., & Everall, P. (2002). Density and distribution of white matter neurons in schizophrenia, bipolar disorder and major depressive disorder: No evidence for abnormalities of neuronal migration. *Molecular Psychiatry*, *7*, 564–570. https://doi.org/10.1038/sj.mp.4001038

Betz, W. (1874). Anatomischer Nachweis zweier Gehirncentra. [Anatomical evidence of two brain centers]. *Zentralblatt für die Medizinischen Wissenshaften*, *12*, 578–580.

Bhagwandin, A., Debipersadh, U., Kaswera-Kyamakya, C., Gilissen, E., Rockland, K. S., Molnar, Z., & Manger, P. R. (2020). Distribution, number, and certain neurochemical identities of infracortical white matter neurons in the brains of three megachiropteran bat species. *Journal of Comparative Neurology*, *528*, 3023–3038. https://doi.org/10.1002/cne.24894

Biswas, S. (2018). Role of PCDH 1 gene in the development of childhood asthma and other related phenotypes: A literature review. *Cureus*, *10*, e3360. https://doi.org/10.7759/cureus.3360

Bizley, J. K., Nodal, F. R., Nelken, I., & King, A. J. (2005). Functional organization of ferret auditory cortex. *Cerebral Cortex*, *15*, 1637–1653. https://doi.org/10.1093/cercor/bhi042

Brodal, P. (1968). The corticopontine projection in the cat. I. Demonstration of a somatotopically organized projection from the primary sensorimotor cortex. *Experimental Brain Research*, *5*, 210–234.

Brodal, P. (1978). The cortico-pontine projection in rhesus monkey. Origins and principles of organization. *Brain*, *10*, 251–283. https://doi.org/10.1093/brain/101.2.251

Brodmann, K. (1909). *Localisation in the cerebral cortex*. Translated with editoriall notes and an introduction by L.J. Garey (1999). Imperial College Press.

Butti, C., Fordyce, R. W., Raghanti, M. A., Gu, X., Bonar, C. J., Wicinski, B. A., Wong, E. W., Roman, J., Brake, A., Eaves, E., Spocter, M. A., Tang, C. Y., Jacobs, B., Sherwood, C. C., & Hof, P. R. (2014). The cerebral cortex of the pygmy hippopotamus, *Hexaprotodon liberiensis* (Cetartiodactyla, Hippopotimidae): MRI, cytoarchitecture, and neuronal morphology. *The Anatomical Record*, *297*, 670–700. https://doi.org/10.1002/ar.22875

Clancy, B., Silva, M., & Friedlander, M. J. (2001). Structure and projections of white matter neurons in the postnatal rat visual cortex. *Journal of Comparative Neurology*, *434*, 233–252. https://doi.org/10.1002/cne.1174

Colombo, J. A. (2018). Cellular complexity in subcortical white matter: A distributed control circuit? *Brain Structure and Function*, *223*, 981–985. https://doi.org/10.1007/s00429-018-1609-1

Dell, L. A., Patzke, N., Spocter, M. A., Siegel, J. M., & Manger, P. R. (2016). Organization of the sleep-related neural systems in the brain of the harbour porpoise (Phocoena phocoena). *Journal of Comparative Neurology*, *524*, 1999–2017. https://doi.org/10.1002/cne.23929

Doran, G. A., & Allbrook, D. B. (1973). The tongue and associated structures in two species of African pangolin, *Manis gigantea* and *Manis tricuspis*. *Journal of Mammalogy*, *54*, 887–899. https://doi.org/10.2307/1379083

Eastwood, S. L., & Harrison, P. J. (2005). Interstitial white matter neuron density in the dorsolateral prefrontal cortex and parahippocampal gyrus in schizophrenia. *Schizophrenia Research*, *79*, 181–188. https://doi.org/10.1016/j.schres.2005.07.001

Emery, J. A., Roper, S. N., & Rojiani, A. M. (1997). White matter neuronal heterotopia in temporal lobe epilepsy: A morphometric and immunohistochemical study. *Journal of Neuropathology & Experimental Neurology*, *56*, 1276–1282. https://doi.org/10.1097/00005072-199712000-00002

Foley, N. M., Springer, M. S., & Teeling, E. C. (2016). Mammal madness: Is the mammal tree of life not yet resolved? *Philosophical Transactions of the Royal Society B, Biological Sciences*, *371*, 20150140. https://doi.org/10.1098/rstb.2015.0140

Gritti, I., Manns, I. D., Mainville, L., & Jones, B. E. (2003). Parvalbumin, calbindin, or calretinin in cortically projecting and GABAergic, cholinergic, or glutaminergic basal forebrain neurons of the rat. *Journal of Comparative Neurology*, *458*, 11–31. https://doi.org/10.1002/cne.10505

Gundersen, H. J. (1988). The nucleator. *Journal of Microscopy (Oxford)*, *151*, 3–21. https://doi.org/10.1111/j.1365-2818.1988.tb04609.x

Homman-Ludiye, J., Manger, P. R., & Bourne, J. A. (2010). Immunohistochemical parcellation of the ferret (*Mustela putorius*) visual cortex reveals substantial homology with the cat (*Felis catus*). *Journal of Comparative Neurology*, *518*, 4439–4462. https://doi.org/10.1002/cne.22465

Imam, A., Ajao, M. S., Bhagwandin, A., Ihunwo, A. O., & Manger, P. R. (2017). The brain of the tree pangolin (*Manis tricuspis*). I. General appearance of the central nervous system. *Journal of Comparative Neurology*, *525*, 2571–2582. https://doi.org/10.1002/cne.24222

Imam, A., Bhagwandin, A., Ajao, M. S., Ihunwo, A. O., Fuxe, K., & Manger, P. R. (2018b). Brain of the tree pangolin (*Manis tricuspis*). III. The unusual locus coeruleus complex. *Journal of Comparative Neurology*, *526*, 2570–2584. https://doi.org/10.1002/cne.24519

Imam, A., Bhagwandin, A., Ajao, M. S., Ihunwo, A. O., & Manger, P. R. (2019a). The brain of the tree pangolin (*Manis tricuspis*). IV. The hippocampal formation. *Journal of Comparative Neurology*, *527*, 2393–2412. https://doi.org/10.1002/cne.24519

Imam, A., Bhagwandin, A., Ajao, M. S., & Manger, P. R. (2019b). The brain of the tree pangolin (*Manis tricuspis*). V. The diencephalon and hypothalamus. *Journal of Comparative Neurology*, *527*, 2413–2439. https://doi.org/10.1002/cne.24619

Imam, A., Bhagwandin, A., Ajao, M. S., & Manger, P. R. (2022a). The brain of the tree pangolin (*Manis tricuspis*). VII. The amygdaloid body. *Journal of Comparative Neurology*, pubished online. https://doi.org/10.1002/cne.25345

Imam, A., Bhagwandin, A., Ajao, M. S., & Manger, P. R. (2022b). The brain of the tree pangolin (*Manis tricuspis*). VIII. The subpallial telencephalon. *Journal of Comparative Neurology*, in press.

Imam, A., Bhagwandin, A., Ajao, M. S., & Manger, P. R. (2022c). The brain of the tree pangolin (*Manis tricuspis*). X. The spinal cord. *Journal of Comparative Neurology*, in press.

Imam, A., Bhagwandin, A., Ajao, M. S., Spocter, M. A., Ihunwo, A. O., & Manger, P. R. (2018a). The brain of the tree pangolin (*Manis tricuspis*). II. The olfactory system. *Journal of Comparative Neurology*, *526*, 2548–2569. https://doi.org/10.1002/cne.24510

Imam, A., Bhagwandin, A., Ajao, M. S., Spocter, M. A., & Manger, P. R. (2019c). The brain of the tree pangolin (*Manis tricuspis*). V. The brainstem and cerebellum. *Journal of Comparative Neurology*, *527*, 2440–2473. https://doi.org/10.1002/cne.24721

Islam, M. P., & Roach, E. S. (2015). Tuberous sclerosis complex. *Handbook of Clinical Neurology*, *132*, 97–109. https://doi.org/10.1016/B978-0-444-62792-5.00006-8

Isler, K., & van Schaik, C. P. (2006). Metabolic costs of brain size evolution. *Biology Letters*, *2*, 557–560. https://doi.org/10.1098/rsbl.2006.0538

Jacobs, B., Garcia, M. E., Shea-Shumsky, N. B., Tennison, M. E., Schall, M., Saviano, M. S., Tummino, T. A., Bull, A. J., Driscoll, L. L., Raghanti, M. A., Lewandowski, A. H., Wicinski, B., Chui, H. K., Bertelsen, M. F., Walsh, T., Bhagwandin, A., Spocter, M. A., Hof, P. R., Sherwood, C. C., & Manger, P. R. (2018). Comparative morphology of gigantopyramidal neurons in primary motor cortex across mammals. *Journal of Comparative Neurology*, *526*, 496–536. https://doi.org/10.1002/cne.24349

Johnson, J. I., Kirsch, J. A. W., Reep, R. L., & Switzer, R. C. (1994). Phylogeny through brain traits: more characters for the analysis of mammalian evolution. *Brain, Behavior & Evolution*, *43*, 319–347. https://doi.org/10.1159/000113643

Kaas, J. H. (2017). The organization of neocortex in early mammals. In S. Herculano-Houzel (Ed.), *Evolution of nervous systems* (2nd ed., Vol. 2, pp. 87–101). Academic Press, Elsevier. http://doi.org/10.1016/B978-0-12-804042-3.00032-4

Kilduff, T. S., Cauli, B., & Gerashchenko, D. (2011). Activation of cortical interneurons during sleep: An anatomical link to homeostatic sleep regulation? *Trends in Neuroscience*, *34*, 10–19. https://doi.org/10.1016/j.tins.2010.09.005

Kingdon, J. (1971). *East African mammals: An atlas of evolution in Africa. I*. Academic Press.

Kowianski, P., Dziewiatkowski, J., Kowianska, J., & Morys, J. (1999). Comparative anatomy of the claustrum in selected species: A morphometric analysis. *Brain, Behavior & Evolution*, *53*, 44–54. https://doi.org/10.1159/000006581

Manger, P. R. (2006). An examination of cetacean brain structure with a novel hypothesis correlating thermogenesis to the evolution of a big brain. *Biological Reviews*, *81*, 293–338. https://doi.org/10.1017/S1464793106007019

Manger, P. R., Kiper, D., Masiello, I., Murillo, L., Tettoni, L., Hunyadi, Z., & Innocenti, G. M. (2002a). The representation of the visual field in three extrastriate areas of the ferret (*Mustela putorius*) and the relationship of retinotopy and field boundaries to callosal connectivity. *Cerebral Cortex*, *12*, 423–437. https://doi.org/10.1093/cercor/12.4.423

Manger, P. R., Masiello, I., & Innocenti, G. M. (2002b). Areal organization of the posterior parietal cortex of the ferret (*Mustela putorius*). *Cerebral Cortex*, *12*, 1280–1297. https://doi.org/10.1093/cercor/12/12/1280

Manger, P. R., Nakamura, H., Valentiniene, S., & Innocenti, G. M. (2004). Visual areas in the lateral temporal cortex of the ferret (*Mustela putorius*). *Cerebral Cortex*, *14*, 676–689. https://doi.org/10.1093/cercor/bhh028

Manger, P. R., Pillay, P., Maseko, B. C., Bhagwandin, A., Gravett, N., Moon, D. J., Jillani, N., & Hemingway, J. (2009). Acquisition of brains from the African elephant (*Loxodonta africana*): Perfusion-fixation and dissection. *Journal of Neuroscience Methods*, *179*, 16–21. https://doi.org/10.1016/j.jneumeth.2009.01.001

Marshall, C. D., & Reep, R. L. (1995). Manatee cerebral cortex: Cytoarchitecture of the caudal region in *Trichechus manatus latirostris*. *Brain, Behavior and Evolution*, *45*, 1–18. https://doi.org/10.1159/000113381

Maseko, B. C., Patzke, N., Fuxe, K., & Manger, P. R. (2013). Architectural organization of the African elephant diencephalon and brainstem. *Brain, Behavior and Evolution*, *82*, 83–128. https://doi.org/10.1159/000352004

Mink, J. W., Blumenschine, R. J., & Adams, D. B. (1981). Ratio of central nervous system to body metabolism in vertebrates – Its constancy and functional basis. *American Journal of Physiology*, *241*, R203–R212. https://doi.org/10.1152/ajpregu.1981.241.3.R203

Mortazavi, F., Romano, S. E., Rosene, D. L., & Rockland, K. S. (2017). A survey of white matter neurons at the gyral crowns and sulcal depths in the Rhesus monkey. *Frontiers in Neuroanatomy*, *11*, 69. https://doi.org/10.3389/fnana.2017.00069

Mortazavi, F., Wang, X. Y., Rosene, D. L., & Rockland, K. S. (2016). White matter neurons in young adult and aged rhesus monkey. *Frontiers in Neuroanatomy*, *10*, 15. https://doi.org/10.3389/fnana.2016.00015

Oishi, K., Nakagawa, N., Tachikawa, K., Sasaki, S., Aramaki, M., Hirano, S., Yamamoto, N., Yoshimura, Y., & Nakajima, K. (2016). Identity of neocortical layer 4 neurons is specified through correct positioning into the cortex. *eLife*, *5*, e10907. https://doi.org/10.7554/eLife.10907

Palmer, L. A., Rosenquist, A. C., & Tusa, R. J. (1978). The retinotopic organization of lateral suprasylvian visual areas in the cat. *Journal of Comparative Neurology*, *177*, 237–256. https://doi.org/10.1002/cne.901770205

Patzke, N., Innocenti, G. M., & Manger, P. R. (2014). The claustrum of the ferret: Afferent and efferent connections to lower and higher order visual cortical areas. *Frontiers in Systems Neuroscience*, *8*, 31. https://doi.org.10.3389/fnsys.2014.00031

Paxinos, G., Huang, X. F., & Toga, A. W. (2000). *The rhesus monkey brain in stereotaxic coordinates*. Academic Press.

Paxinos, G., & Watson, C. (2007). *The rat brain in stereotaxis coordinates*. Academic Press.

Paxinos, G., Watson, C., Carrive, P., Kirkcaldie, M. T. K., & Ashwell, K. (2009). *Chemoarchitectonic atlas of the rat brain*. Elsevier.

Paxinos, G., Watson, C., Petrides, M., Rosa, M., & Tokuno, H. (2012). *The marmoset brain in stereotaxic coordinates*. Academic Press, Elsevier.

Pigarev, I. N., & Rodionova, E. I. (1998). Two visual areas located in the middle suprasylvian gyrus (cytoarchitectonic field 7) of the cat's cortex. *Neuroscience*, *85*, 717–732. https://doi.org/10.1016/s0306-4522(97)00642-8

Puelles, L. (2017). Comments on the updated tetrapartite pallium model in the mouse and chick, featuring a homologous claustro-insular complex. *Brain, Behavior and Evolution*, *90*, 171–189. https://doi.org/10.1159/000479782

Radtke-Schuller, S. (2018). *Cyto- and Myeloarchitectural brain atlas of the ferret (Mustela putorius) in MRI aided stereotaxic coordinates*. Springer International Publishing AG.

Rahman, F. E, & Baizer, J. S. (2007). Neurochemically defined cell types in the claustrum of the cat. *Brain Research*, *1159*, 94–111. https://doi.org/10.1016/j.brainres.2007.05.011

Randle, S. C. (2017). Tuberous sclerosis complex: A review. *Pediatric Annals*, *46*, e166–e171. https://doi.org/10.3928/19382359-20170320-01

Real, M. A, Davila, J. C., & Guirado, S. (2003). Expression of calcium-binding proteins in the mouse claustrum. *Journal of Chemical Neuroanatomy*, *25*, 151–160. https://doi.org/10.1016/S0891-0618(02)00104-7

Reale, R. A., & Imig, T. A. (1980). Tonotopic organization in auditory cortex of the cat. *Journal of Comparative Neurology*, *192*, 265–291. https://doi.org/10.1002/cne.901920207

Reep, R. L., Johnson, J. I., Switzer, R. C., & Welker, W. I. (1989). Manatee cerebral cortex: Cytoarchitecture of the frontal region in *Trichechus manatus latirostris*. *Brain, Behavior and Evolution*, *34*, 365–386. https://doi.org/10.1159/000116523

Reynhout, K., & Baizer, J. S. (1999). Immunoreactivity for calcium-binding proteins in the claustrum of the monkey. *Anatomy and Embryology*, *199*, 75–83. https://doi.org/10.1007/s004290050211

Ringo, J. L., Doty, R. W., Demeter, S., & Simard, P. Y. (1994). Time is of the essence: A conjecture that hemispheric specialization arises from interhemispheric conduction delay. *Cerebral Cortex*, *4*, 331–343. https://doi.org/10.1093/cercor/4.4.331

Scannell, J. W., & Young, M. P. (1993). The connectional organization of neural systems in the cat cerebral cortex. *Current Biology*, *3*, 191–200. https://doi.org/10.1016/0960-9822(93)90331-H

Schmahmann, J. D., & Pandya, D. P. (2006). *Fiber pathways of the brain*. Oxford University Press.

Sedmak, G., & Judaš, M. (2019). The total number of white matter interstitial neurons in the human brain. *Journal of Anatomy*, *235*, 626–636. https://doi.org/10.1111/joa.13018

Shipp, S., Adams, R. A., & Friston, K. J. (2013). Reflections on agranular architecture: Predictive coding in the motor cortex. *Trends in Neurosciences*, *36*, 706–716. https://doi.org/10.1016/j.tins.2013.09.004

Smith, J. B., Alloway, K. D., Hof, P. R., Orman, R., Reser, D. H., Watakabe, A., & Watson, G. D. R. (2018). The relationship between the claustrum and endopiriform nucleus: A perspective towards consensus on cross-species homology. *Journal of Comparative Neurology*, *527*, 476–499. https://doi.org/10.1002/cne.24537

Swiegers, J., Bhagwandin, A., Maseko, B. C., Sherwood, C. C., Hard, T., Bertelsen, M. F., Spocter, M. A., Molnar, Z., & Manger, P. R. (2021b). The distribution, number, and certain neurochemical identities of infracortical white matter neurons in the brains of a southern lesser galago, a black-capped squirrel monkey, and a crested macaque. *Journal of Comparative Neurology*, *529*, 3676–3708. https://doi.org/10.1002/cne.25216

Swiegers, J., Bhagwandin, A., Sherwood, C. C., Bertelsen, M. F., Maseko, B. C., Hemingway, J., Rockland, K. S., Molnar, Z., & Manger, P. R. (2018). The distribution, number, and certain neurochemical identities of infracortical white matter neurons in a lar gibbon (*Hylobates lar*) brain. *Journal of Comparative Neurology*, *527*, 1633–1653. https://doi.org/10.1002/cne.24545

Swiegers, J., Bhagwandin, A., Sherwood, C. C., Bertelsen, M. F., Maseko, B. C., Hemingway, J., Rockland, K. S., Molnár, Z., & Manger, P. R. (2019). The distribution, number, and certain neurochemical identities of infracortical white matter neurons in a Lar gibbon (Hylobates lar) brain. *Journal of Comparative Neurology*, *527*, 1633–1653. https://doi.org/10.1002/cne.24545

Swiegers, J., Bhagwandin, A., Williams, V. M., Maseko, B. C., Sherwood, C. C., Hard, T., Bertelsen, M. F., Rockland, K. S., Molnar, Z., & Manger, P. R. (2021a). The distribution, number, and certain neurochemical identities of infracortical white matter neurons in a chimpanzee (*Pan troglodytes*) brain. *Journal of Comparative Neurology*, *529*, 3429–3452. https://doi.org/10.1002/cne.25202

Tomioka, R., & Rockland, K. S. (2007). Long-distance corticocortical GABAergic neurons in the adult monkey white and gray matter. *Journal of Comparative Neurology*, *505*, 526–538. https://doi.org/10.1002/cne.21504

Tusa, R. J., & Palmer, L. A. (1980). Retinotopic organization of areas 20 and 21 in the cat. *Journal of Comparative Neurology*, *193*, 147–164. https://doi.org/10.1002/cne.901930110

Tusa, R. J., Palmer, L. A., & Rosenquist, A. C. (1978). The retinotopic organization of area 17 (striate cortex) in the cat. *Journal of Comparative Neurology*, *177*, 213–235. https://doi.org/10.1002/cne.901770204

Tusa, R. J., Rosenquist, A. C., & Palmer, L. A. (1979). Retinotopic organization of areas 18 and 19 in the cat. *Journal of Comparative Neurology*, *185*, 657–678. https://doi.org/10.1002/cne.901850405

van der Gucht, E., Hof, P. R., van Brussel, L., Burnat, K., & Arckens, L. (2007). Neurofilament protein and neuronal activity markers define regional architectonic parcellation in the mouse visual cortex. *Cerebral Cortex*, *17*, 2805–2819. https://doi.org/10.1093/cercor/bhm012

van Essen, D. C., & Dierker, D. L. (2007). Surface-based and probabilistic atlases of primate cerebral cortex. *Neuron*, *56*, 209–223. https://doi.org/10.1016/j.neuron.2007.10.015

Watson, C., Mitchelle, A., & Puelles, L. (2017). A new mammalian brain ontology based on developmental gene expression. In J. H. Kaas (Ed.), *Evolution of nervous systems* (2nd ed., pp. 53–75). Elsevier.

Watson, C., & Puelles, L. (2017). Developmental gene expression in the mouse clarifies the organization of the claustrum and related endopiriform nuclei. *Journal of Comparative Neurology*, *525*, 1499–1508. https://doi.org/10.1002/cne.24034

West, M. J., Slomianka, L., & Gundersen, H. J. (1991). Unbiased stereological estimation of the total number of neurons in the subdivisions of the rat hippocampus using the optical fractionator. *Anatomical Record*, *231*, 482–497. https://doi.org/10.1002/ar.1092310411

Yamawaki, N., Borges, K., Suter, B. A., Harris, K. D., & Shepherd, G. M. G. (2014). A genuine layer 4 in motor cortex with prototypical synaptic circuit connectivity. *eLife*, *3*, e05422. https://doi.org/10.7554/eLife.05422

How to cite this article: Imam, A., Bhagwandin, A., Ajao, M. S., & Manger, P. R. (2022). The brain of the tree pangolin (*Manis tricuspis*). IX. The pallial telencephalon. *Journal of Comparative Neurology*, *530*, 2645–2691. https://doi.org/10.1002/cne.25349